A NONLINEAR CIRCUIT MODEL FOR LITHIUM-ION BATTERIES

by

Shengru Ren

B.A.Sc, The University of British Columbia, 2011

A THESIS SUBMITTED IN PARTIAL FULFILLMENT OF

THE REQUIREMENTS FOR THE DEGREE OF

MASTER OF APPLIED SCIENCE

in

THE FACULTY OF GRADUATE AND POSTDOCTORAL STUDIES

(Electrical and Computer Engineering)

THE UNIVERSITY OF BRITISH COLUMBIA

(Vancouver)

December 2013

Abstract

A lithium ion battery model is required for proper design of battery powered systems such as marine applications. The various existing models lack of the nonlinear aspect of the batteries being studied, suffer from high complexity and are not quite suitable for system level simulation. Therefore the scope of this thesis is to produce a battery model capable of capturing the nonlinearity of the battery for system level design. The Randle circuit model is selected as the base model to build upon and the electrochemical impedance spectroscopy is chosen as the fundamental test method for extracting the model parameters. The nonlinearity is accounted for by defining the equivalent circuit model elements' parameters functions of the state of charge. Since lithium-ion batteries are prone to be affected by the changes in temperature, all the experiments are done under controlled temperature. The proposed model is a modified Randle circuit model in time domain implemented in MatLAB/SIMULINK. The model's validity is verified using test data. It is concluded that this final version of model proposed in this thesis can be used directly in system level simulation while offering reasonable accuracy. However the proposed model does suffer from its dependency on the cell chemistry, which will limit its applications.

Preface

The text of the thesis is original and unpublished work of the author, S. Ren.

The circuit design in Chapter 3 was done by Dr. William Dunford. The circuit was constructed and tested by myself.

The models introduced in section 4.1 and 4.2 were developed by myself. The model introduced in section 4.3 was completely by me, with assistance from E. Fok. The validation experiments mentioned in section 4.4 were designed by E.Fok and carried out by myself.

Table of Contents

List of Tables

List of Figures

List of Abbreviations

EIS	Electrochemical impedance spectroscopy
NI	National Instrument
DAQ	Data acquisition card
SoC	State of charge
CCS	Current controlled source
CVS	Voltage controlled source
VM	Voltage measurement
CM	Current measurement
NMC	Lithium-nickel-manganese-cobalt
ESR	Equivalent series resistance

Acknowledgements

Foremost, I would like to express my sincere gratitude to my supervisors Dr. William Dunford and Dr. John Madden for their continuous support throughout my research and study. Their patience, immerse knowledge and guidance helped me both during my research project but also during the process of writing the thesis.

I would also like to thank my thesis committee: Dr. William Dunford, Dr. John Madden and Dr. Martin Ordonez.

I thank Corvus Energy Inc. for its technical support.

I thank Natural Sciences and Engineering Research Council of Canada for its financial support.

I owe special thanks to Mr. Eddie Fok for his great help and mentorship. I'd like to offer particular thanks to Mr. John Chow for his insights and suggestions.

I would also like to thank all of my colleagues from UBC and friends who have supported me throughout my study.

I offer my sincere thanks to my family for their understanding, support and never ending love.

Dedicated to my parents

Chapter 1: Introduction

Before we start our discussion about battery modelling, one might be curious of what importance it has and why researchers are so keen on producing accurate models. The answer is apparent once we learn more about the current applications of batteries. Battery technology has improved dramatically over the years as batteries are becoming more and more widely used in industries ranging from large scale, such as substation back up power source, to small scale, such as laptops, cell phones, and other portable devices. As the systems which use batteries as a primary or secondary power supply become increasingly complex, it is more and more important for system designers to be able to predict the behaviour of batteries used in the system under various conditions. Through the knowledge of the general performance of batteries, designers can estimate how long the battery can sustain under normal or extreme conditions. With even more advanced technology such as usage scheduling [1], it is possible to extend the battery life beyond its manufacture rating. Other battery research topics and applications include protection from hazardous operations such as overcharge or short circuit, early indication of battery failure, and battery synchronization and balancing [2]. However, usage scheduling or other technique is based on the thorough knowledge of the batteries, thus proving that battery modelling is crucial to practical battery applications.

This thesis will focus on creating a model such that the model can be applied in the two cases described below. In case one, a model is needed to assist in the design of a hybrid system in which the designer can use a black-box battery model to predict how the batteries perform under different loads. In case two, the aim is to create a battery model that will enable predictions to be

made of the effect of the batteries on the marine system during potentially hazardous situations, of whose predictions will be used by insurance companies and marine safety agencies.

1.1 Background and motivation

Batteries can be divided into two categories: primary and secondary. Primary batteries are easy to use, often have a long shelf life, require little maintenance but can be used only once [3]. This is due to the fact that they generally cannot be recharged, although, in special cases, some primary batteries can be recharged with a fairly limited lifetime [4]. Secondary batteries, which can be recharged, offer much longer lifetime and are among the most economical power solutions to many industrial or commercial problems. Therefore it is of particular interest in the industrial field to model the operation of secondary batteries. In the interest of this thesis, a study is done on a lithium-ion secondary battery cell provided by an industrial partner.

A lithium ion battery consists of three major components which are the anode, cathode and electrolyte. When the current flows, the electrolyte carries the ions between the anode and cathode. During discharge, the metallic anode supplies lithium ions Li^+ to the electrolyte. The electrolyte carries the ions to the cathode, where they are being inserted into the cathode. During charging, the external power source applies an over-voltage which is higher than that of the battery itself to force the current flow in the reserve direction. The Li^+ ions are then released from the cathode and carried back to the anode by the electrolyte. For a secondary lithium ion battery, the process of the insertion of Li^+ ions and the exchange of electrons between anode and cathode must be reversible [5].

Similar to many other devices or systems, a battery or a battery cell[1] has many physical characteristics which can be modelled or interpreted as different parameters. These characteristics can be grouped into two main types: thermodynamic and kinetic properties [4]. Thermodynamic parameters describe the system in equilibrium when there is no current and all the reactions are balanced. Thermodynamic parameters describe the maximum limit of the performance data which will be reduced by the influence of kinetic parameters once there is current. Kinetic parameters, which are influenced by parameters such as cell thickness and electrode spacing, account for the rates of internal chemical reactions that convert chemical energy into electrical energy, and the movement of reacting species. They include mass transport caused by migration or diffusion, where migration is caused by the current and diffusion is caused by the difference in the concentration of the reacting species [4].

A battery has the following general parameters which are commonly used to determine the state and health of the battery: voltage, capacity, temperature, and internal resistance [4]. For lithium-ion secondary batteries in particular, the battery voltage, or often referred to as the state of charge (SoC), and temperature effect is often of research interest. It is also known that some cell parameters such as equivalent capacitance are SoC dependent [6], which means SoC is the essential parameter when developing a battery model. Research has also shown that lithium-ion batteries[2] are very sensitive to temperature changes [7]. It is found that many cell parameters are not only SoC dependent, but also temperature dependent. For the scope of this thesis, the effect of temperature is not investigated and all the experiment is carried out at one controlled

[1] A battery cell is a single component which can be connected either in series or in parallel to construct a battery. In practice, some single cell can also be referred to as battery, such as a commercial alkaline primary battery [4].In this thesis, the words 'battery' and 'cell' are interchangeable.

[2] In this thesis, lithium-ion batteries refer to the secondary batteries. Primary lithium-ion batteries are not covered.

temperature. Due to the limited time available for this research project, the aging effect is also not covered in this thesis. The primary interest of this thesis is to investigate the behaviour of battery SoC under a constant temperature, over a range of charging/discharging cycles and currents where the performance is not affected, and to develop a model which can run in Matlab to predict the battery performance. At the request of the industrial partner, Matlab is chosen as the platform software to develop the model.

Much work has been done on battery modelling [8][9][10][11]. Some models provide run-time I-V predictions, and others focus on the non-linearity aspect. Many models also have coefficients which are battery dependent [12][13]. Even though there are models which are meant to be "chemistry independent" [14], it is in the interest of this thesis to develop a model specifically fit for the battery provided by the industrial partner, which is made of lithium-nickel-manganese-cobalt (NMC). Such a tailor-designed model not only can describe the battery accurately but also can be used to better understand the battery cell in order to improve the battery performance in future cell design and production. Among the many approaches employed by other researchers, the Randle circuit model is chosen to be the base of the battery model developed in this thesis because the Randle circuit is simple to use and is able to describe the physical reactions inside the cell. A Randle's circuit includes the following circuit elements: equivalent series resistance, charge transfer resistance, double layer capacitance and the Warburg impedance. The equivalent series resistance accounts for the internal resistance as well as the contact resistance. A current is induced in the electrode surface region when the Li^+ ions diffuse into the surrounding electrolyte and the electrons enter the lithium metal. The speed of electrode reaction (or the current) is governed by the rate of the mass transfer, the rate of the electron transfer at the electrode surface, the chemical reactions at the surface and other surface reactions. The magnitude of the current is

limited by a sum of the over-potentials of different reaction steps. The electrode reaction can be presented by a resistance which includes the mass-transfer resistance R_{mt}, the charge-transfer resistance R_{ct}, etc as shown in Figure 1 [15].

Figure 1: Processes in an electrode reaction represented as resistances

An electrical double layer is formed between the electrolyte and the surface of the electrode. The double layer capacitance accounts for the capacitance generated by the ions from the electrolyte being absorbed onto the electrode [16]. The Warburg impedance is caused by diffusion and its magnitude depends on the frequency. The Warburg impedance is small at high frequencies and it increases with decreasing frequencies [16].

Due to the linear nature of the Randle circuit, in order to capture the nonlinearity aspect of the cell, the proposed model in this thesis is a nonlinear model built upon the linear Randle circuit. It is the goal of this research project to develop a model which offers great simplicity while providing accurate results for practical purposes, allowing it to be directly connected to the rest of a system model. This thesis will present a nonlinear model that is designed for the lithium ion cells provided by the industrial partner. The model will predict the performance of the battery in the range of 3V to 4.2V, under a constant temperature at 22˚C. The aging effect is not accounted for by the model.

1.2 Thesis outline

The thesis consists of five chapters, with the first being the Introduction, followed by Chapter 2, a literature review, in which modelling work done previously by other researchers are explored and presented. In Chapter 3 the experimental design, setup as well as the experimental results are presented and discussed. Chapter 3 presents three tests which are the EIS test, the charge/discharge cycle test and the pulse charge/discharge test. Chapter 4 presents the model itself and the validation data. In Chapter 4, two linear frequency domain models and one nonlinear time domain models are presented. The nonlinear model is built based on the linear frequency model. Chapter 5 concludes the thesis and provides discussions on possible future work.

Chapter 2: Literature review

As the batteries are becoming more and more crucial in many applications such as hybrid vehicles, marines and other heavy industrial projects, it is becoming increasingly important to capture and predict battery performance and behaviour using battery models. The aim of this thesis is not to describe the change in battery performance with time, but rather describe its response on normal operating conditions and over a time and usage period in which capacity and other characteristics are stable. The other aspects such as temperature and aging effects will be added in future research. Amongst the vast amount of literature work on battery modelling, the following models are selected and reviewed as they are often reviewed and cited by other researchers, and many advanced models are built upon these fundamental models. Following the approach taken in [17], the various battery models are categorized as the following types: analytical models and abstract models.

2.1 Analytical models

Analytical models are good for modelling the run-time behaviour of the batteries as well as the nonlinear effective capacity during discharge. These models do not require a large set of equations and therefore are easy to manage and computationally-efficiency [18]. However, because of this simplicity, they are not very suitable for capturing the electrochemical processes inside the cell or the dynamic I-V characteristic [19]. Among the three types of models, analytical models are generally the least accurate [17].

There are several different analytical models proposed [12][17]. One of the proposed analytical models is Peukert's law which is used to estimate the remaining capacity of the cell [12]. When using the Peukert's law, it is important to note that under varying load conditions, the resulted

remaining capacity estimation may be underestimated [12]. In addition, the Peukert's law does not account for the temperature changes during battery operation [13], whereas the temperature effect is a crucial part in modelling lithium ion batteries.

2.2 Abstract models

Abstract models provide an equivalent representation of a battery in continuous-time or discrete-time environment. Abstract models offer better accuracy than analytical models and are less computational costly than electrochemical models [17]. There are three major abstract model categories, electrical equivalent circuit model, discrete time model and stochastic model. The discrete time model is not chemically based which allows it be employed on different battery chemistries [14][20][21]. The stochastic model can be very useful in the scheduling battery discharge to improve the battery lifetime by allowing the battery to relax properly after a burst discharge [8][22]. The emphasis will be placed on the electrical equivalent circuit model.

Electrical circuit models use an equivalent circuit to capture the general behaviour of the cell and predict the run-time performance. In general, the electrical circuit models can be divided into two categories which are Thevenin's equivalent model and impedance based model [23].

2.2.1 Thevenin's equivalent model

The Thevenin equivalent model can be used to predict the dynamic characteristics of the battery [24]; however its main disadvantage is that all the elements in the equivalent circuit are assumed to be constant [25]. The equivalent circuit elements are in fact functions of the state of charge of the battery as well as cell temperature.

2.2.2 Impedance based model

Batteries are electrochemical systems and it is very useful to use impedance based models, which can be extracted from electrochemical impedance spectroscopy (EIS) measurements. These models are employed to analyse the dynamic behaviour of the batteries at different SoC and operation temperatures [26]. EIS can be carried out by passing a small ac current through the battery and measuring its ac voltage response. As a result of the nonlinearity of most electrochemical systems, several impedance measurements at different working points are required for analysis [27]. From the measurements, the battery's characteristic parameters and other information of the chemical reactions can be extracted and evaluated [17]. Several impedance based models have been proposed [26][27][28][29] and study has shown that the extracted equivalent capacitance can be very useful in predicting the SoC of lithium-ion batteries [17]. One drawback of EIS measurements is that they usually require a long experimental time due to the very long time constants involved in many cells.

One common model used to explain the impedance spectra is a Randle circuit. A Randle circuit consists of a series resistance $R_{s,}$ with the parallel combination of the double-layer capacitance C_{dl}, and charge transfer resistance R_{ct} in series with a constant phase element Zw [30]. Figure 2 shows the basic Randle model.

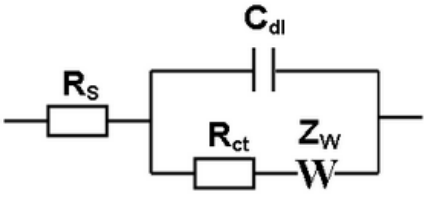

Figure 2: Randle circuit

The Randle circuit is commonly used in EIS studies. It is chosen as the foundation model to build upon in this thesis because the equipment needed for extracting the circuit parameters is readily available. As discussed later in Chapter 4, a Randle circuit is not enough to capture the nonlinearity of the battery cell and thus a modified nonlinear Randle circuit model is developed. Although Randle's circuit is commonly used, the nonlinear version of it has not been proposed before.

Chapter 3: Experimental setup and results

This chapter explains the experiment design and the rationale behind it. After reviewing the design principle, the detailed experiment setup will be presented for each experiment. Following the experimental setup, the test results are presented and explained. It will be explained further in the detail how the test data is used to extract models in Chapter 4.

3.1 Experiment design

During this research project, three different experiments are performed which are electrochemical impedance spectroscopy (EIS) test, constant current charge and discharge, and pulse discharge. EIS tests are one of the common experiments employed for developing impedance based models. They can provide useful information about the equivalent circuit parameters, which will be applied in the time domain model. Many EISs are performed at different state of charge (SoCs) to produce sufficient data points for the parameters needed in the nonlinear time domain model.

EIS tests are carried out to extract the equivalent series resistance, double layer capacitance and charge transfer resistance. Constant current charge and discharge can be used to extract equivalent capacitance [31]. It is later found that the equivalent capacitance plays a crucial role in the modeling results and more data points of the equivalent capacitance for various cell potentials will yield a more accurate fitting result. Although EIS tests can also be used to find the equivalent capacitance, constant current operation offers more data points within a shorter period of time. Constant current operation is carried out not only to provide equivalent capacitance data but also to validate the model extracted from EIS tests. In particular, constant current partial charge/discharge tests are performed to simulate the real load conditions for model validation

purposes. Another experiment, pulse operation, is designed and executed to validate the battery model. During the pulse operation, the cell is charged and discharged using short constant current pulses. Temperature control is employed because there is an effect of temperature on the cell performance and it is then desired to keep the surrounding ambient temperature of the cell constant at 22˚C in order to minimize the effect of the heat generated during cell operation.

3.2 Experimental setup

Two Dow Kokam cells are tested to obtain data. The two cells are named as Cell A and Cell B for identification purpose. They are made of lithium-nickel-manganese-cobalt (NMC). These Dow Kokam cells have the following specifications: nominal voltage of 3.7V, lower limit voltage of 2.7V, upper limit voltage of 4.2V and a rated capacity of 76.5Ah. In this section, the experimental setups of the EIS tests, charge/discharge cycles, the pulse operations, as well as the temperature control, are explained below.

3.2.1 EIS test setup

A cell is an electrochemical system, making the EIS test suitable for measuring and characterizing the frequency response of the cell. A Solartron 1260A is used to perform EIS tests; the Solartron applies an AC current with a 1A amplitude to the cell and the frequency of the injected current sweeps from $10^5 Hz$ down to 0.1 mHz. 1A is chosen to be the amplitude of the AC current after comparing results taken from lower current amplitudes. 1A is the

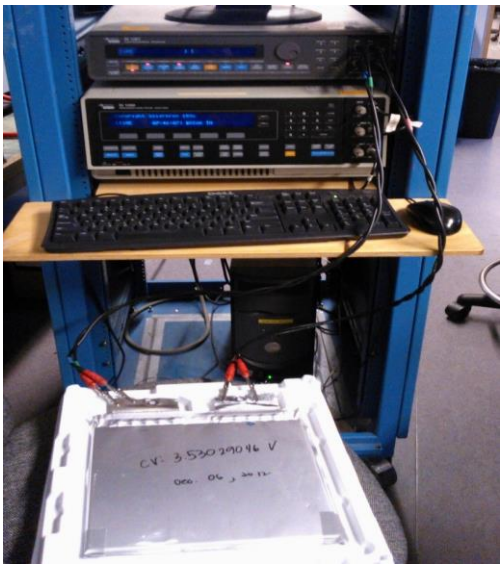

Figure 3: EIS test connection

maximum that the Solartron is able to supply and it yields the same results with lower currents, but with much less noises.

The connection of the cell to the Solartron is shown Figure 3, as performed before insertion into a controlled temperature bath. The left electrode shown in Figure 3 is the negative electrode and the right one is the positive electrode. The four probes connected to the cell are two reference electrodes, one working electrode and one counter electrode. A reference electrode is an electrode whose potential is well defined and stable. The potential of a half cell can be measured against a reference electrode in an electrochemical cell. The working electrode is where the reaction of interest occurs and the counter electrode is where the current flows [15]. One reference electrode and the working electrode are twisted together to minimize the noise caused by the line inductance. Similarly, the other reference electrode and the counter electrode are twisted together. The working electrode and one reference electrode are connected to the positive electrode of the cell, which is on the right side. The counter electrode and one reference electrode are connected to the negative electrode of the cell, which is on the left side. The 1A current is being applied via the counter electrode and the working electrode where the voltage across the cell terminals is measured between the two reference electrodes.

3.2.2 Charge/discharge cycle setup

The cell voltage and current are to be monitored and recorded. Labview 2013 and a National Instrument Data Acquisition card (NI DAQ)[3] are used to monitor and control the battery testing process, which automatically cycles the cell through charge and discharge. Typically the cells are charged and discharged from nearly full (4.1V) to nearly empty (3V) or vice versa. A special

[3] Device number: NI DAQ card USB-6211

case is made in the constant current partial charge and discharge operation, where the cells are charged or discharged only by a fraction of the batteries' total capacity. For instance, the cells will be discharged from 100% to 75% and charged up again to 100%. This is to provide validation data for model verification, since the model should be able to predict the battery performance under all kinds of load conditions as well as at different cell capacities.

3.2.2.1 Battery test circuit

Figure 4 illustrates the testing circuit. R_s is a 1 mΩ shunt resistor used to monitor the current and R_l is a 0.07Ω resistor bank used to discharge the cell.

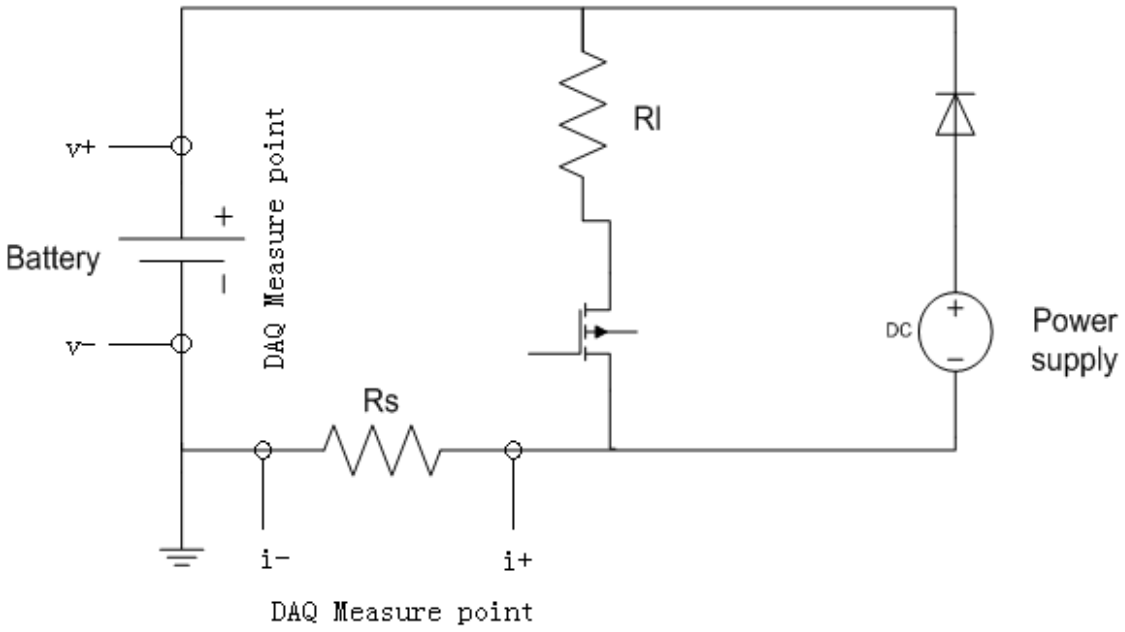

Figure 4: Battery test circuit

The rated resistance of the shunt resistor is 1 mΩ. Using four-point-probe method, the actual voltage drop is measured to be 0.00921V when the applied current is 10A. The measurement is taken using a HP 34401A digital meter. The actual resistance of the shunt resistor has an uncertainty of 10%. The resistor bank is constructed using twelve 0.82Ω (+/- 1%), 25W power

resistors connected in parallel. The actual resistance measured with the HP 30441A digital meter using four-point-probe method is 0.07 Ω where the calculated resistance is 0.068 Ω. The resistor bank resistance has an uncertainty of 3%.

The battery cell is charged by a DC power supply[4] using a constant current. It is then allowed to rest for an hour before being discharged using constant current. The one hour resting period is recommended by the industrial partner. During the charging process, the constant current is controlled by the DC power supply while the discharge branch is turned off by turning off the MOSFET[5]. During the discharging process, the cell is discharged through the resistor bank while the power supply output is turned off. The discharge current is maintained constant by controlling the MOSFET. As the cell voltage drops, a program is used to adjust the DAQ card voltage and in turn adjusts the gate voltage of the MOSFET to maintain the current, as described in the next section.

3.2.2.2 Test control program in Labview

The charging and discharging processes are monitored and logged by using a NI DAQ card, which is controlled using Labview. Labview operates under the three modes: charge, discharge and rest. Depending on the measured cell voltage, Labview will choose which operation mode to enable. Figure 5 shows the algorithm of the Labview program. The cycle operation code can be found in appendix A.1.

[4] The power supply's series number is XFR 1200 20V-60A Watt Programmable DC Power Supply
[5] The MOSFET's series number is IRF 3205

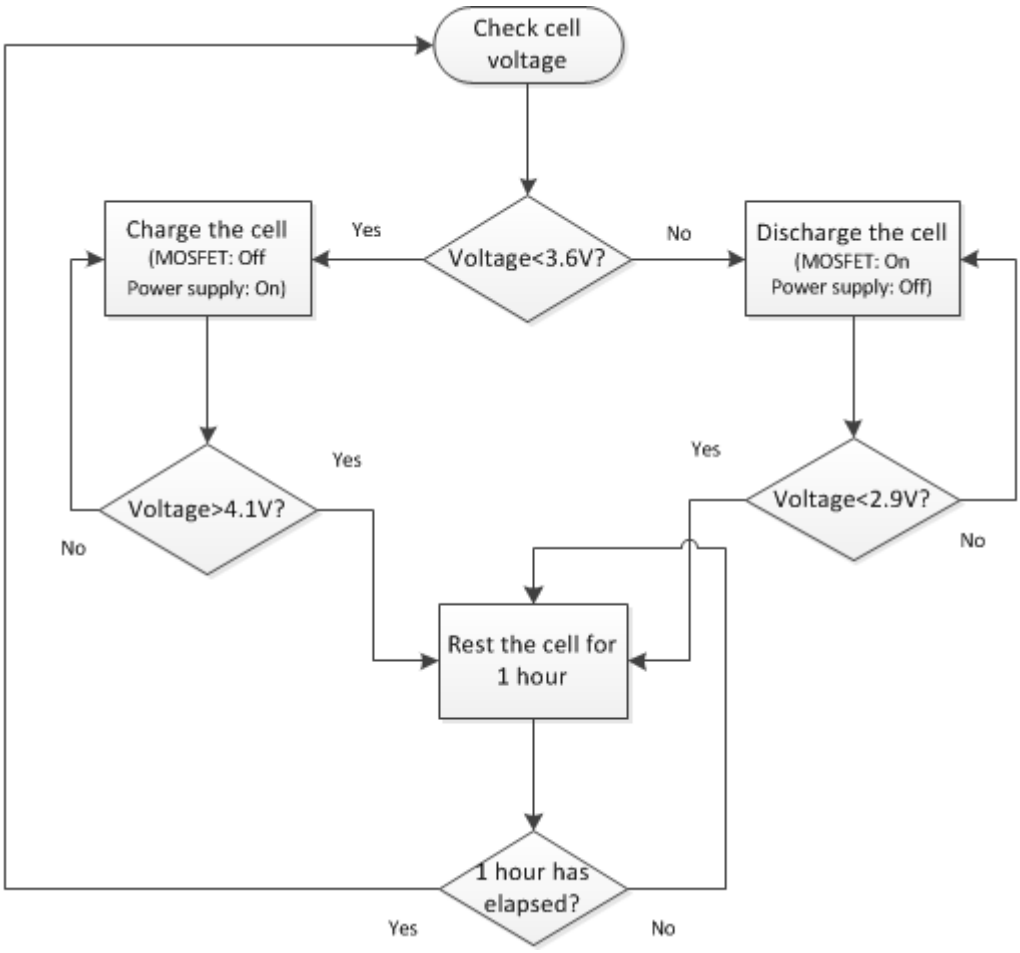

Figure 5: Labview control program

3.2.3 Pulse charge/discharge setup

The pulse operation is designed to resemble the real battery operating conditions in order to provide useful validation data. This approach has been employed previously by other researchers [11][19] [23]. In practice, the cells are to be charged or discharged at various SoCs for different durations rather than going through full charge or discharge cycles. Hence pulse tests can be used to mimic the frequent on and off operation of the batteries. The data collected from this test can be used to see how fast and accurately the model follows the changes in load conditions and the model's transient response. The cells are charged and discharged using a pulsed constant current. For instance, the pulse discharge operation procedure is described as the following: starting from

fully charged state 4.1V, one cell is discharged at 15A for a fixed amount of time, for example, five minutes after which the cell will be let rest for an hour. This pulsed discharge repeats 12 times and the discharge time is changed to 12.5 minutes, which is again followed by a rest period of an hour after each discharge. 15A is chosen as the operating current for easy calculation. The operation is illustrated in Table 1: Pulse discharge operation. The pulse charge test uses the same design approach as the discharge, with the exception of the current direction. The testing circuitry is explained in section 3.2.3.1. Similar to the cycle operation, the pulse test is also automated by a Labview program which is explained in section 3.2.3.2.

Discharge time	Rest time	Number of repeats
5 minutes	1 hour	14
12.5 minutes	1 hour	12
5 minutes	1 hour	2
2.5 minutes	1 hour	8

Table 1: Pulse discharge operation at 15A, starting from 4.1V

3.2.3.1 Testing circuitry

The circuit used to do the pulse discharge is illustrated in Figure 6. It consists of the battery cell, a power supply, a load resistor R_l, a relay and a shunt resistor R_s. The power supply, together with the cell, provides the constant 15A current. As the cell voltage drops during the discharge, the power supply provides the extra voltage needed to keep the potential across the cell and the power supply at constant, which results in a constant current flow in the circuit. Similar to the charge and discharge cycle circuit, the resistor load R_l is used to dissipate the heat during the discharge. The shunt resistor R_s is for monitoring the current. The relay is controlled by Labview

which automates the operation. Labview automatically runs the series of discharges by switching on and off the relay while taking the measurements. Similarly, the pulse charge circuitry uses the same setup as the pulse discharge, only without the load resistor R_l and the power supply being connected in the reverse direction. The pulse charge test is also controlled by the Labview program. The labview control program is discussed in section 3.2.3.2.

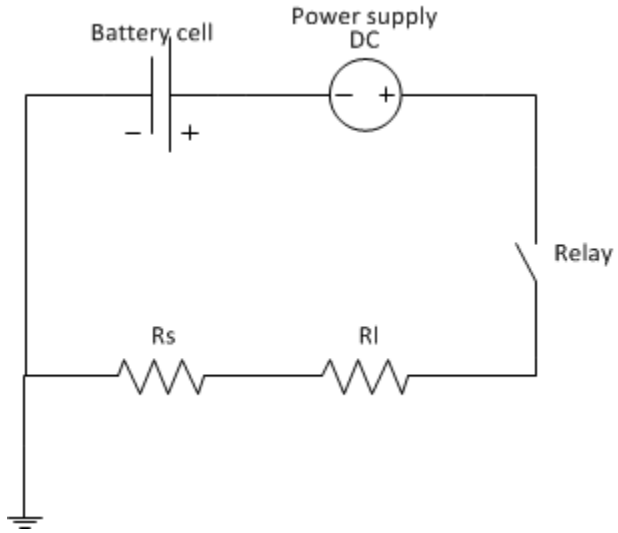

Figure 6: Pulse discharge testing circuitry

3.2.3.2 Labview control program

A program written in Labview is used to control the operation. Figure 7 is the algorithm of the Labview control program. The pulse discharge code can be found in appendix A.2. The pulse charge code has the same algorithm, only with a different threshold. The threshold '*voltage<2.9V'* is replaced by '*voltage>4.1V'* in the pulse charge code.

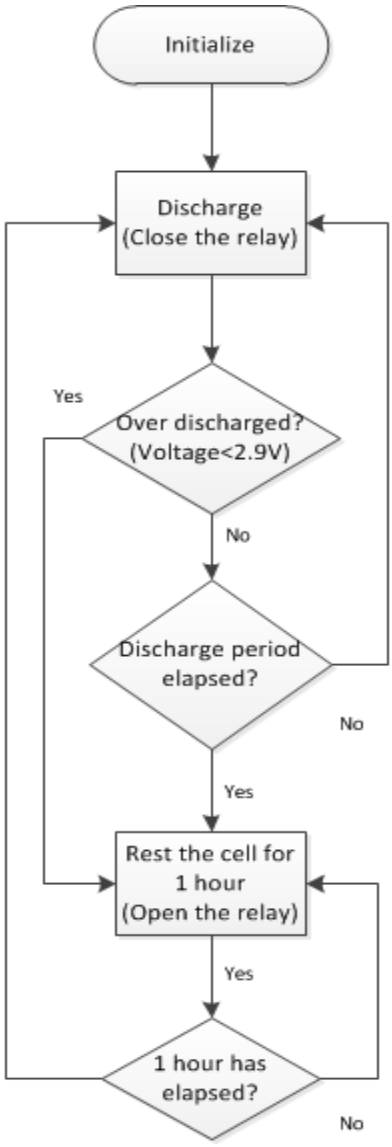

Figure 7: Labview control program for pulse discharge operation

3.2.4 Temperature control

Although the cell being investigated does not heat up dramatically during testing, the temperature is controlled to minimize the temperature effects on the test results. Temperature control is achieved by using a water bath and a circulator. The cell is wrapped by three layers of small kitchen garbage bags to insulate it from water. The insulated cell is then placed inside a water tank, where the water is circulated through the circulator[6]. The circulator regulates the water temperature to be within +/- 1 degree of the set temperature. The +/- 1 degree uncertainty is measured using a thermometer throughout the day while the circulator is running. During the experiment, the temperature is maintained to be 22 Celsius degrees.

3.3 Test results

The results obtained from the EIS tests, cycle tests and the pulse discharge are presented here. The test results are further analysed to extract parameters used in battery modelling, and to provide data for model verification, which will be discussed in details in Chapter 4.

3.3.1 EIS data

The cell goes through several EIS tests at different states of charge (SoC). The obtained data are expressed in a Nyquist plot and Bode plot. Figure 8 and Figure 9 are the Bode plot and Nyquist plot for the 4 different SOC, respectively. At each SOC, it is observed that the cell has a different equivalent capacitance associated with the SOC.

[6] The circulator's model number: Fisher Scientific Isotemp Refrigerated circulator Model 900

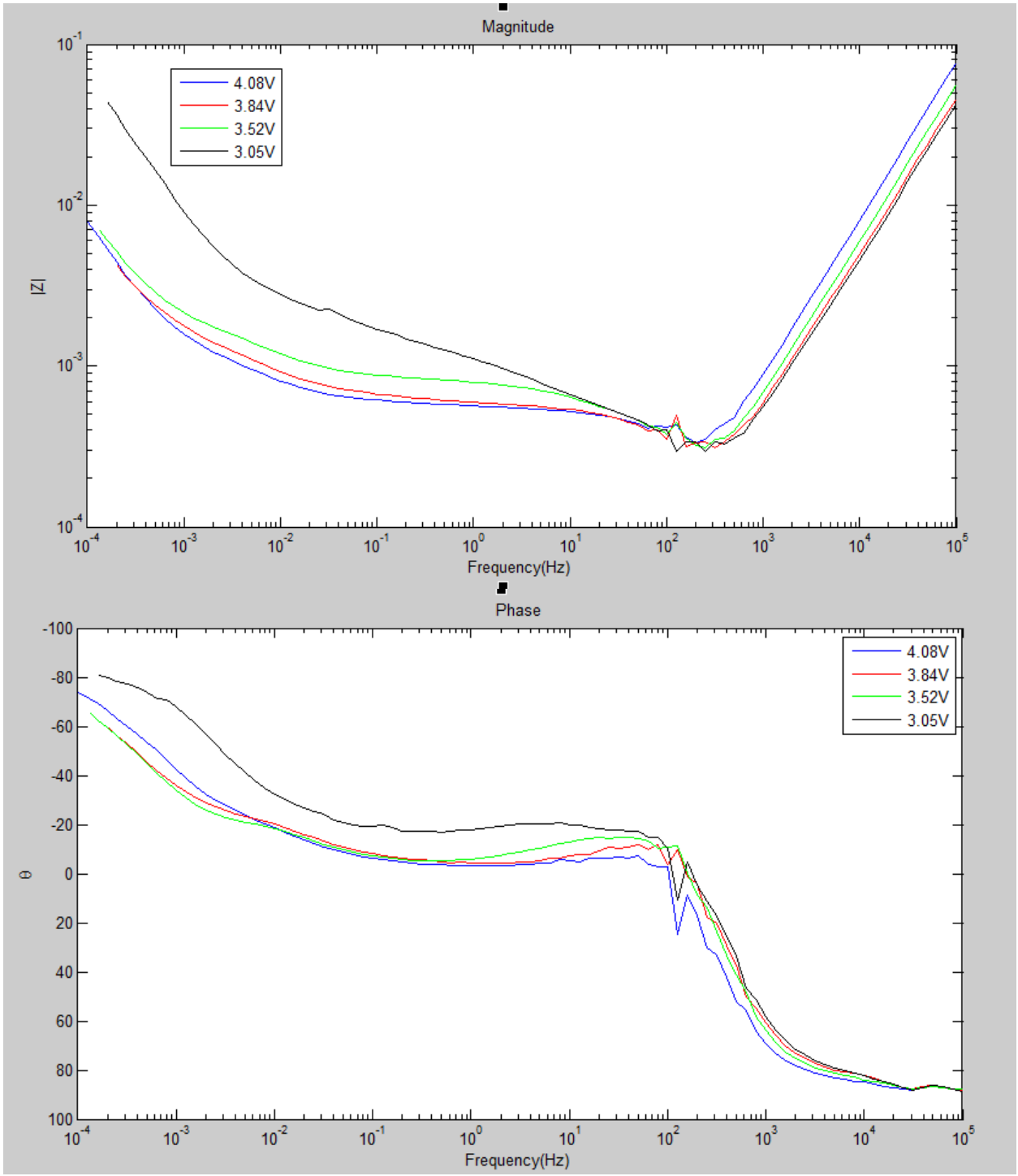

Figure 8: Bode plot of cell A at 4 different SoCs

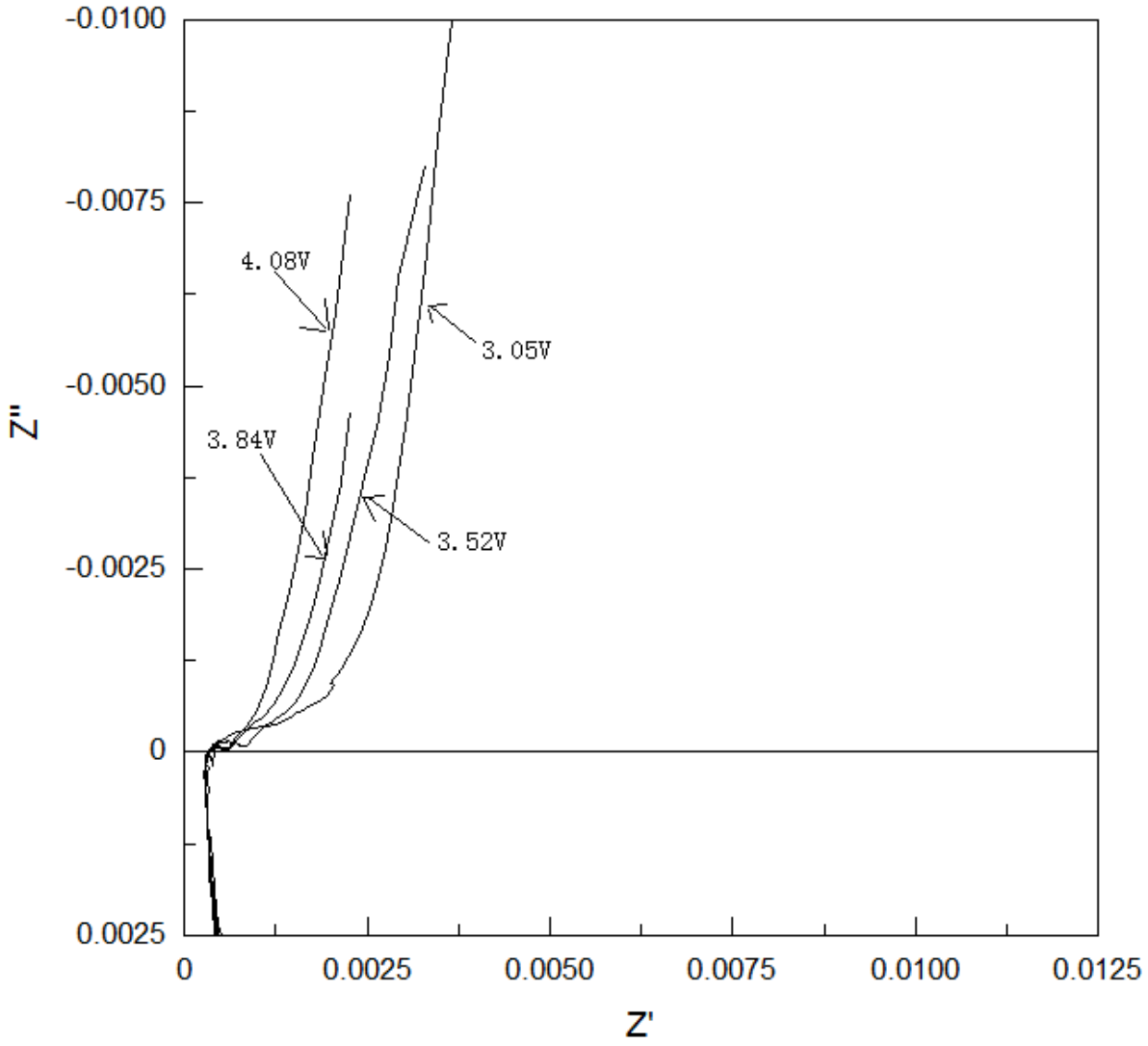

Figure 9: Nyquist plot of cell A at 4 different SoCs

In Figure 8, the upper plot is the magnitude and the lower plot is the phase. It can be seen that as the cell is moved from one SoC to the next SoC, the frequency response changes gradually with the change in SoC. The spikes seen around 120Hz are speculated to have been caused by the line frequency. From the phase plot it can be seen that at high frequencies, the cell behaves like an inductor with nearly 90 degree phase. At low frequencies, the cell behaves like a capacitor with

nearly -90 degree phase. In between, the resistive behaviour can be seen in the Nyquist plot where there's a semicircle.

3.3.2 Cycle data

The battery cell undergoes deep charge and discharge cycles at a constant current. A sample discharge cycle plot is shown in Figure 10. Figure 11 shows the constant current charge cycle.

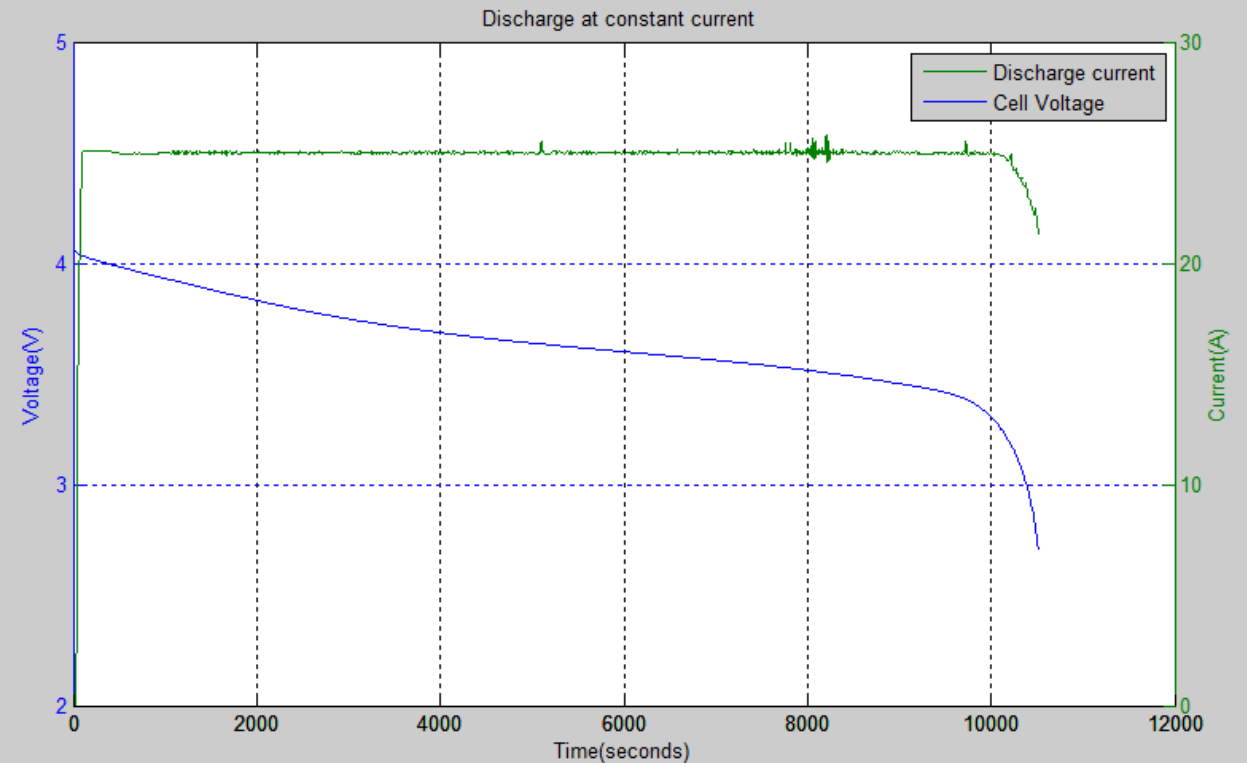

Figure 10: Discharge curve of cell B at 25A

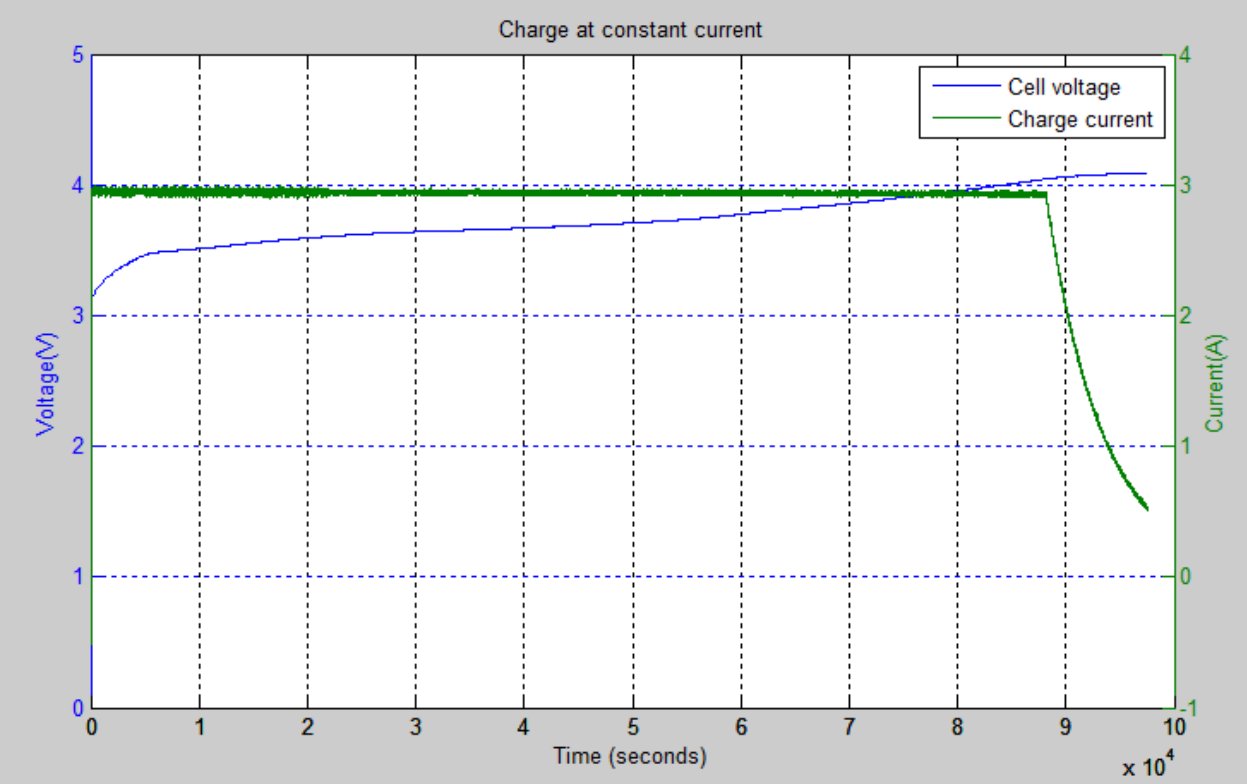

Figure 11: Charge curve of cell B at 3A

The cell was charged slowly (slow scan test) from 3V to 4.1V at 3A and 1.5A. Using the data from the charging cycles, the equivalent capacitance of the cell can be extracted by applying equation (1) $\boldsymbol{C = \frac{I}{dv/dt}}$, where *I* is the constant charging current and dv/dt can be found by taking the slope of the voltage curve.

$$\boldsymbol{C = \frac{I}{dv/dt}} \quad (1)$$

The capacitance calculated from the charging curves' constant current region is shown in Figure 12.

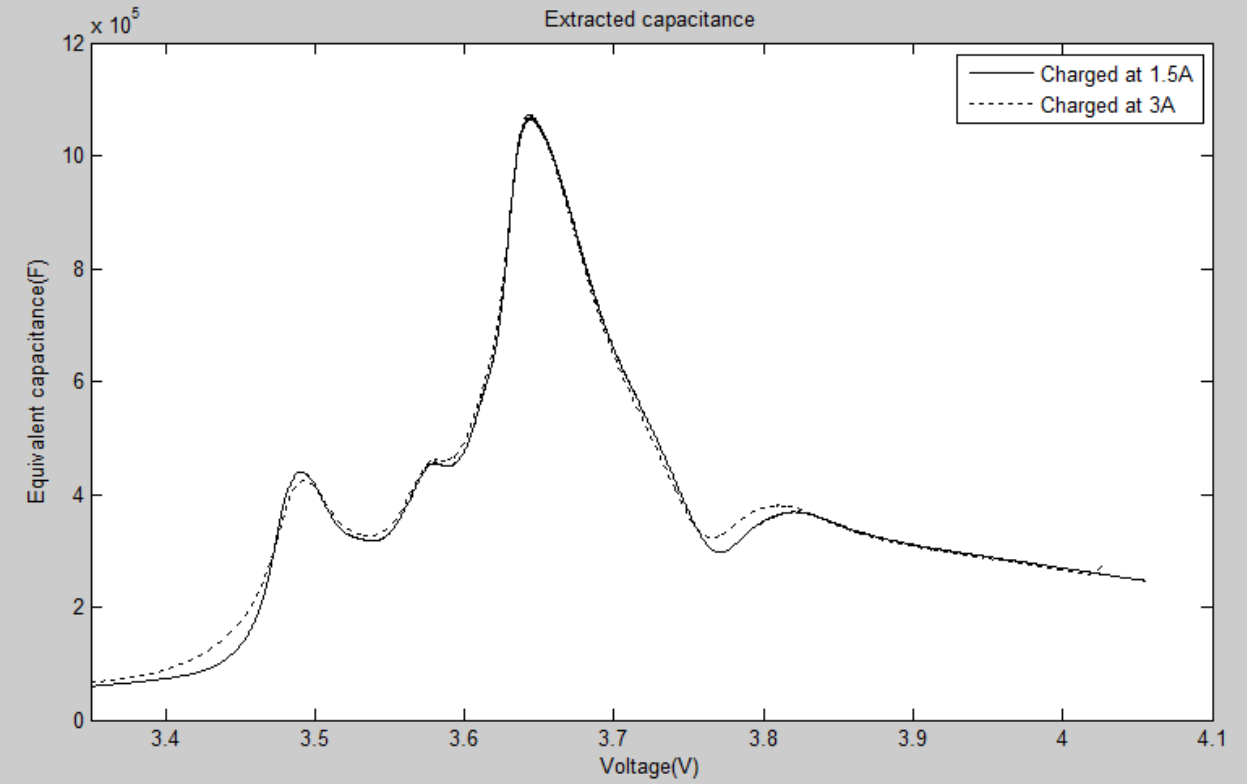

Figure 12: Equivalent capacitance extracted from charging data from cell A and B using 3A and 1.5A constant current, respectively

The capacitance extracted from 2 sets of charging data matches with each other, which confirms that the two cells are consistent and implies that the parameters from the two cells should be reasonably close enough. A wider ranged 'capacitance v.s. voltage' curve can be found in appendix B. The matching curves also indicate that the cell capacitance is, indeed, a function of voltage. The charging profile rather than the discharging profile is used for extracting the equivalent capacitance is because the DC power supply is more reliable at outputting a constant current than the MOSFET controlled circuit. This voltage-dependency will be used in the nonlinear model, as explained in Chapter 4.

The consistency of the calculated capacitance as a function of current suggests the possibility of developing a simple model purely based on the equivalent capacitance, similar to what had been proposed in [31], where the Zimmermann model is employed to describe change in capacity of cells as they age. This approach is likely feasible, but would require modification as the Zimmermann model assumes a Gaussian-shaped voltage dependence of cell capacitance with cell voltage. The focus in this thesis is placed on the physical model extracted from the EIS tests as this is the first outcome desired by the industry partner. However, using the equivalent capacitance to implement a Zimmermann model is of future interest.

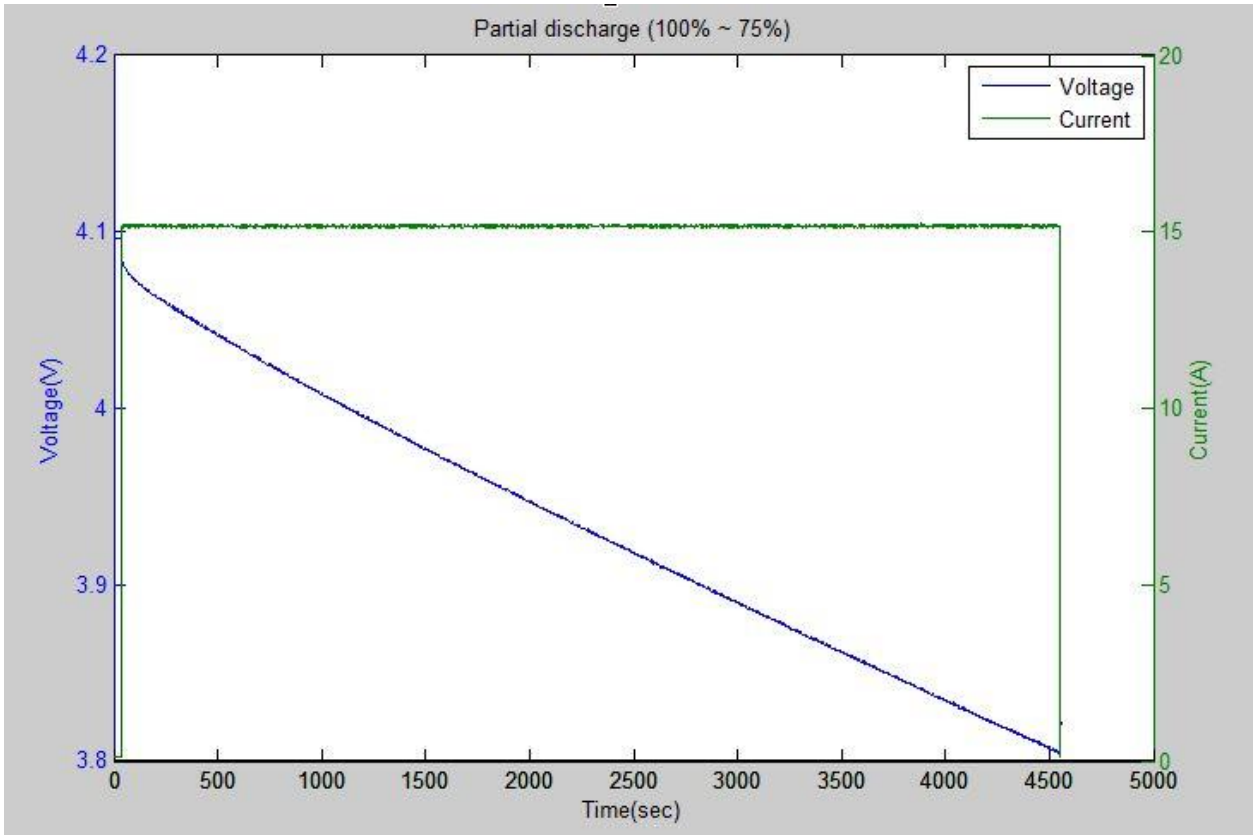

Figure 13: Partial discharge

Figure 13 depicts partial discharge data for the current pulse applied from the fully charged state. As mentioned earlier, the partial discharge is done under constant current and the data collected is for validation purposes.

3.3.3 Pulse test data

The test data from one pulse charge experiment is plotted in Figure 14.

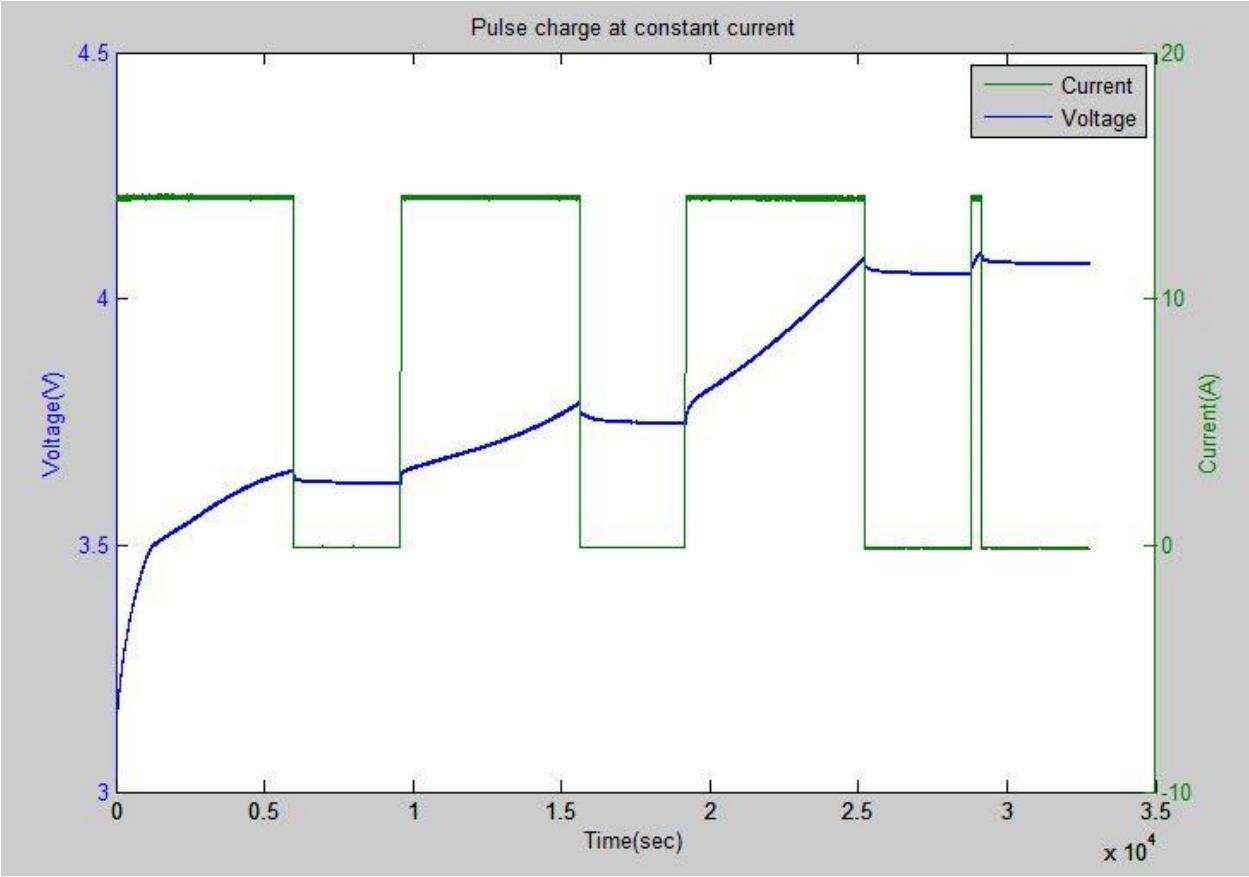

Figure 14: Pulse discharge sample data

The cell is charged and discharged using pulsed current for various durations. The data are used in validating the nonlinear Simulink model, which is covered in Chapter 4.

Note that as expected from the capacitance vs. voltage plot in Figure 12, the slope of the voltage at constant current drops sharply when 3.5 V is reached, as expected given the sudden rise in

capacitance at this cell potential. The lowest slopes are between 3.6 and 3.7 V, again as expected given the less stiff changes in capacitance. The drop in voltage seen during open circuit is expected given the equivalent circuit resistance and distributed nature of the charge storage. This drop is relatively small, suggesting that the rate of charging seen here is not leading to large charging gradients in the electrodes.

In this chapter, the experiment design, experimental setup and the test results are presented. EIS test are performed to extract parameters for the various circuit elements such as the equivalent series resistance, double layer capacitance and charge transfer resistance. Cycle operation and pulse operation are carried out to not only provide the equivalent capacitance but also provide validation data. The following chapter will explain how the extracted data is used to implement and verify the model.

Chapter 4: Modelling and validation

Using the data obtained from the experiments discussed in chapter 3, two frequency domain models and a time domain model are developed. This chapter presents the three models and their simulation results, as well as the validation data.

4.1 Simple frequency domain model

This section discusses the rationale behind the design of the modified Randle circuit model and the model fitting results in frequency domain. Following the fitting of frequency responses using these models, we will turn to simplified non-linear versions that can represent time response.

4.1.1 Data analysis

Following the discussion in section 3.3.1, the detailed explanation and analysis of the EIS testing data is provided here.

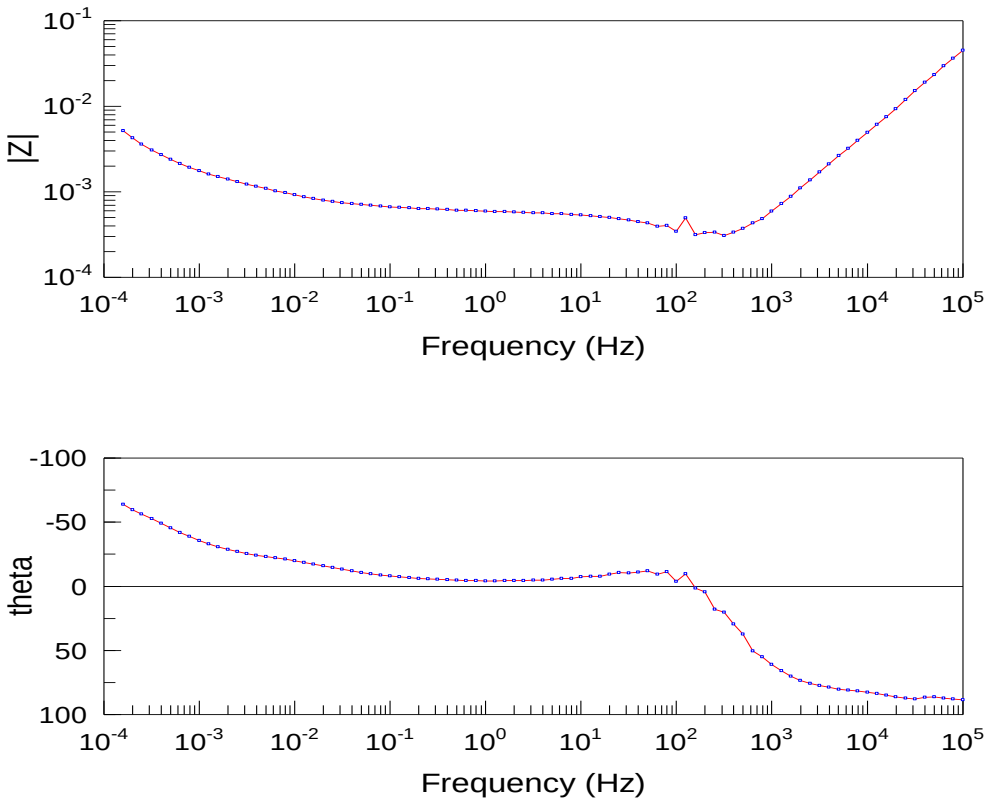

Figure 15: Bode plot for cell A at 3.84V with 1A ac sweep current

Figure 15 and Figure 16 are one set of sample EIS data at 3.84V. From the Nyquist plot, it is observed that the semicircle can be described using a parallel combination of a resistor and a capacitor. Following the approach taken in [32], the frequency dependent impedance seen at low frequencies is represented by a Warburg element. A series resistor is needed to account for the magnitude shown in the Bode plot. A series inductor is required to account for the slope at high frequencies. The analysis of the EIS tests suggests that a Randle circuit can be used to model the battery. A Randle's circuit has the elements mentioned above, except the series inductor – which is needed to describe the high frequency response.

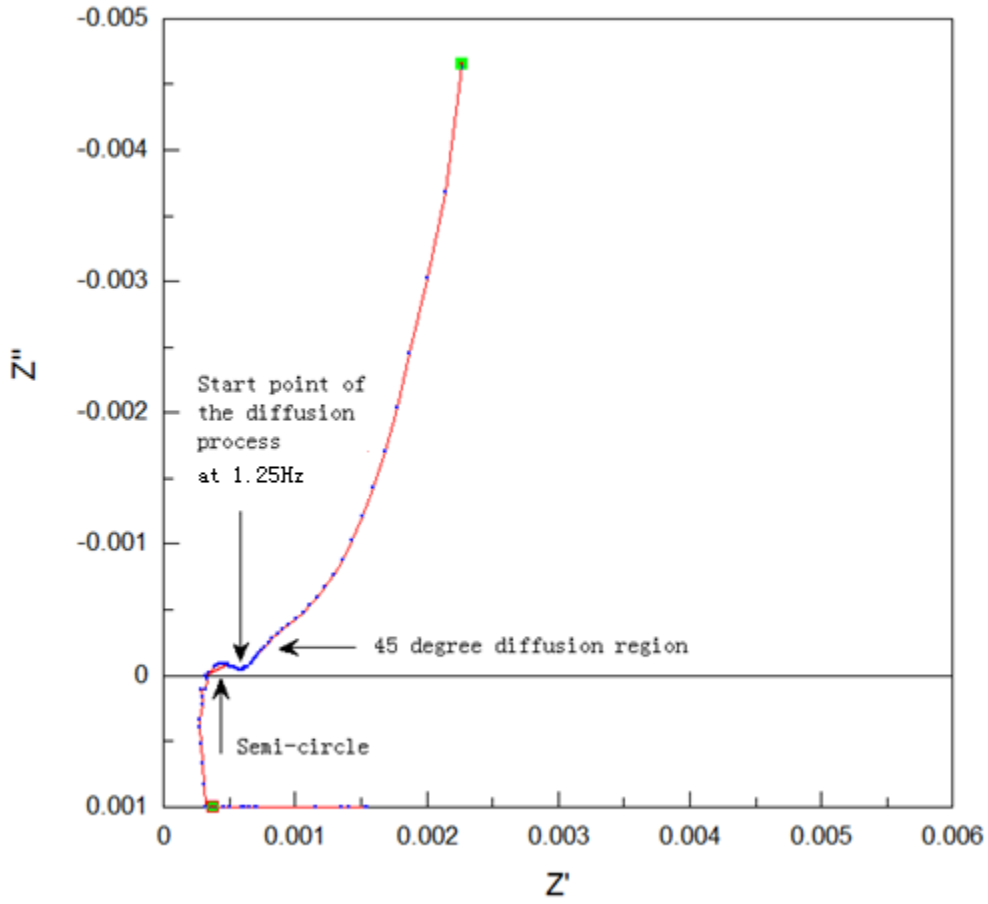

Figure 16: Nyquist plot for cell A at 3.84V from 10^5Hz to 1 mHz

A frequency domain model is designed based on the Randle equivalent circuit model with a few variations adjusted to fit to the testing data. The EIS data obtained from Solartron is plotted and analyzed in Zview2. The equivalent circuit is also developed and simulated in Zview2. Figure 17 shows a version of the frequency domain model. More complex models will be used to describe the very low frequency response.

As shown in Figure 17, an inductor is added in series with the series resistance to account for the inductance at high frequency, caused by the porous natural of the battery electrodes [33]. The constant phase element is replaced by a Warburg element. In this model, R_1 accounts for the

series resistance which includes the battery internal resistance and contact resistance. L_1 accounts for the inductive behaviour, caused by measurement cable inductance, at high frequencies. C_1 denotes the double layer capacitance and R_{ct} presents the charge transfer resistance. W_1 is the open circuit Warburg element which captures the diffusion effect. The Warburg element models finite-length diffusion, and can be described in lumped parameters using a finite length RC transmission line, as discussed in section 4.3.

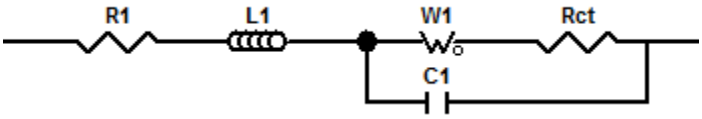

Figure 17: Simple frequency model

The data can be used to estimate the parameters for the modified Randle model. On the Nyquist plot, there is a semicircle followed by a 45° slope. After the 45° slope, the curve is dominated by the capacitive behaviour. The 45° slope indicates a diffusion process [16]. The semicircle is due to the parallel combination of the double layer capacitance and the charge transfer resistance. The left intersection of the semicircle and the x-axis is accounted for by the series resistance R_1, which includes the solution resistance and contact resistance.

The circuit elements parameters are found to be voltage dependent after analysing the data from various SoCs. It is found that the value of R_1depends on the SoC. The height of the semicircle is determined by the double layer capacitance C_1, whereas the width of the semicircle is determined by charge transfer resistance R_{ct}. It is observed from datasets obtained from several different SoCs that as the cell varies SoC, the value of the double layer capacitance C_1 and the charge transfer resistance R_{ct} also vary.

The dependence of double layer capacitance on SoC may enable an estimate the SoC of the battery cell to be made very quickly. This is an area of future research interest. Last but the not least, the parameters for the Warburg element are recognized to be voltage dependent as well. It is then established that the elements in the modified Randle circuit are all voltage dependent and individual fitting data is required for each element to account for the nonlinearity. The individual fitting data translates into the lookup-tables used in the time domain model discussed in section 4.3. First the model fitting is shown.

4.1.2 Fitting result

EIS tests are performed at different SoCs and some of the SoCs are nearly overlapping to assess test results' repeatability. The model shown in Figure 17 is applied to each of the data sets collected at various SoCs, and the parameters are adjusted for each data set to produce the best fitting result.

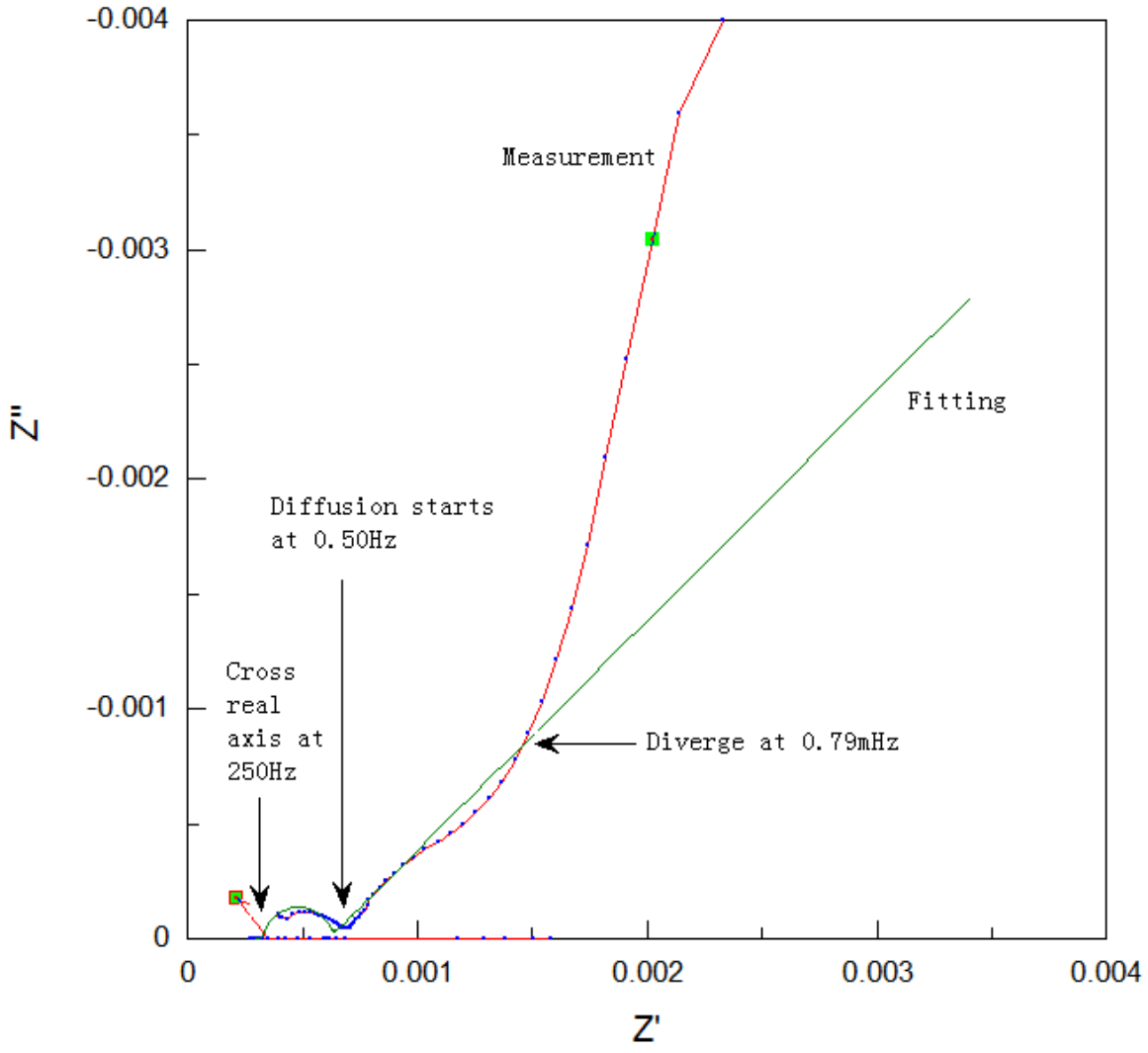

Figure 18: Nyquist - cell A at 3.62V

The simple version produces a fairly accurate fit at high frequencies and around the semi-circle in the Nyquist plot as shown in Figure 18. It also produces a good fit in Bode plot, as shown in Figure 19. With only one Warburg element, the model is not able to capture the extreme low frequency response (see Figure 18). This effect is investigated further in the section that follows.

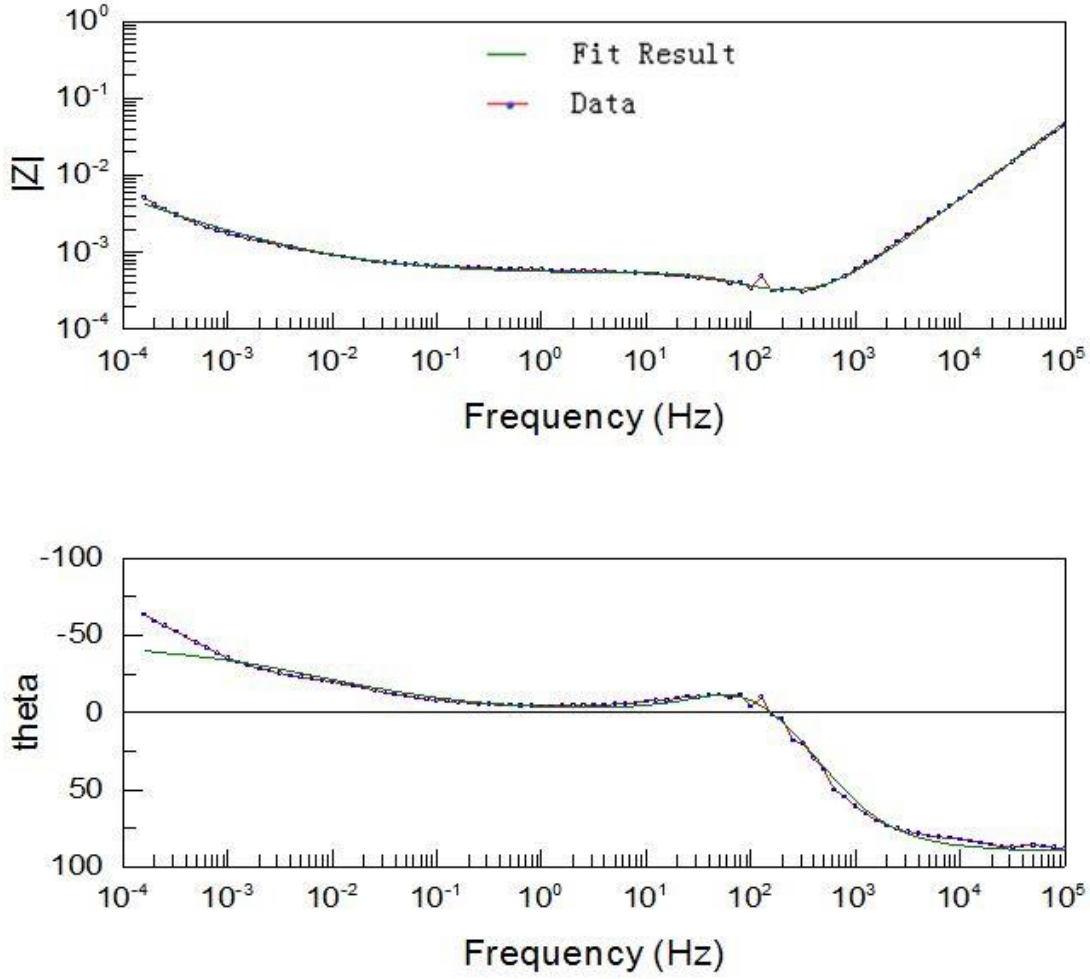

Figure 19: Bode plot – cell A at 3.62V

Table 2 shows the parameters found at four different SoCs. $W_1 - R$ represents the resistance of the transmission line and $W_1 - T$ is the time constant associated with the transmission line. $W_1 - P$ is always 0.5 for diffusion process.

SoC(V)	4.08V(error%)	3.84V(error%)	3.52V(error%)	3.05V(error%)
$R_1(m\Omega)$	0.33(5.70)	0.31(3.06)	0.32 (3.42)	0.30(6.87)
$L_1(H)$	1.24E-7(2.76)	7.86E-8(1.73)	9.24E-8(2.08)	6.64E-8(4.56)
$W_1 - R(m\Omega)$	21.1(311.26)	20.01(2.68)	82.40(2.7E7)	492.7(4.76E7)
$W_1 - T(s)$	27156(620.16)	27114(4.84)	279420(5.4E7)	280710(9.51E7)
$W_1 - P$	0.5	0.5	0.5	0.5
$R_{ct}(m\Omega)$	0.15(13.29)	0.22(5.10)	0.36(4.46)	0.35(12.38)
$C_1(F)$	15.72(34.48)	11.61(13.26)	13.52(11.31)	15.78(21.59)

Table 2: Simple model fitting parameters for cell A using circuit from Figure 17

It can be seen that the fitting parameters are voltage dependent. This dependency can later be used to develop a time domain nonlinear model presented in section 4.3. For more fitting results, please refer to appendix B.1.

4.2 Complex frequency domain model

Model shown in Figure 17 doesn't account for the low frequency response caused by multiple time constants. The signal to noise ratio becomes poor at extremely low frequency. To account for the slope of the Nyquist plot shown in Figure 18, a more complex frequency is developed. This model, which is illustrated in Figure 20, builds upon the simple model discussed in section 4.1.

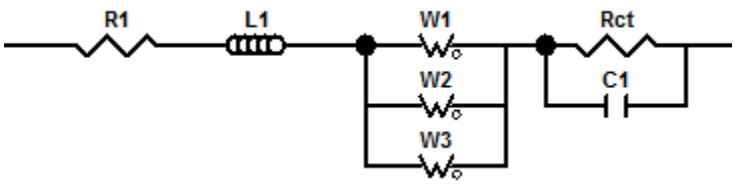

Figure 20: Complex frequency domain model

The fitting results at 3.88V are shown in Figure 21 and Figure 22.

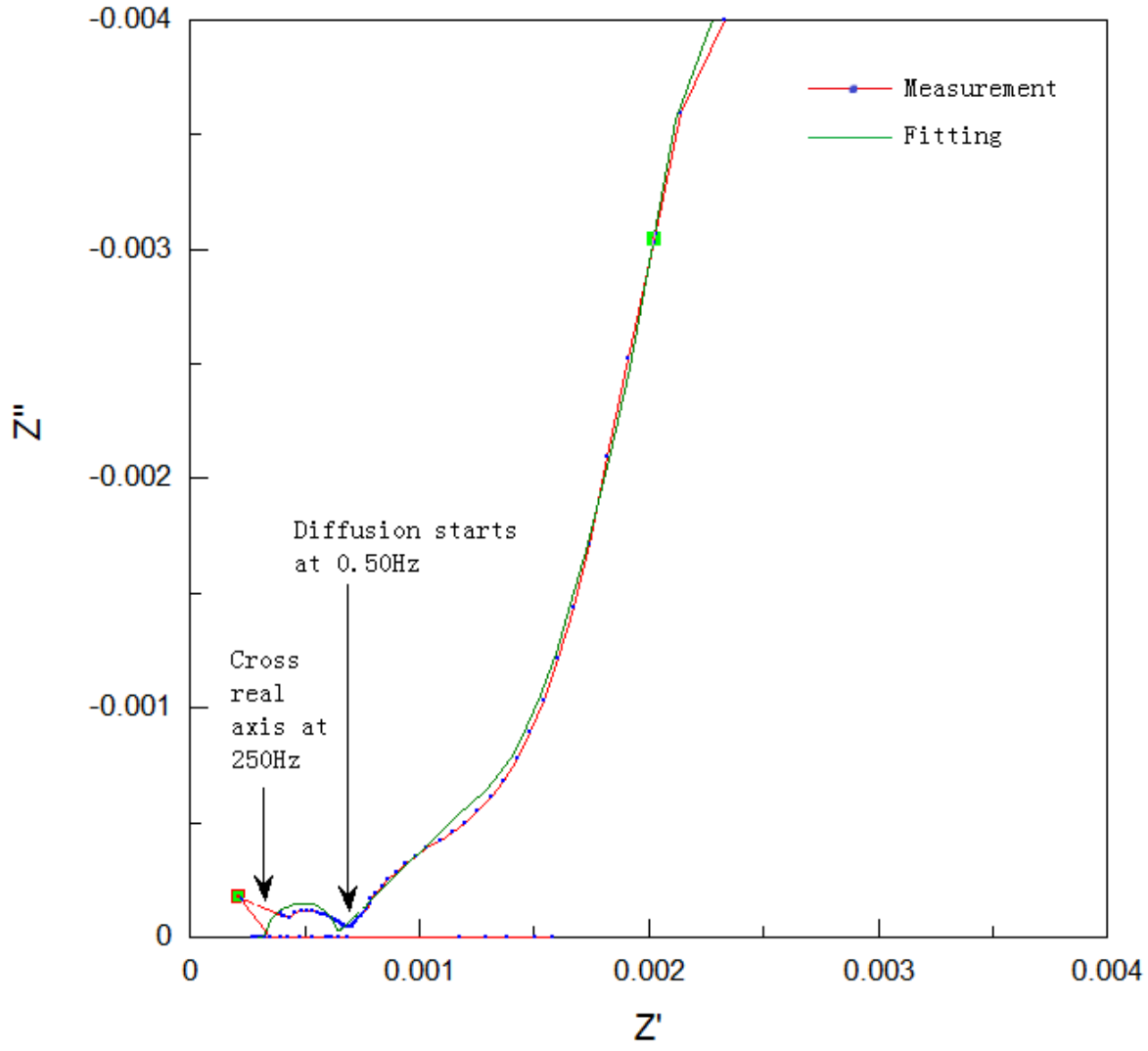

Figure 21: Nyquist – cell A at 3.62V with 1A ac sweep current

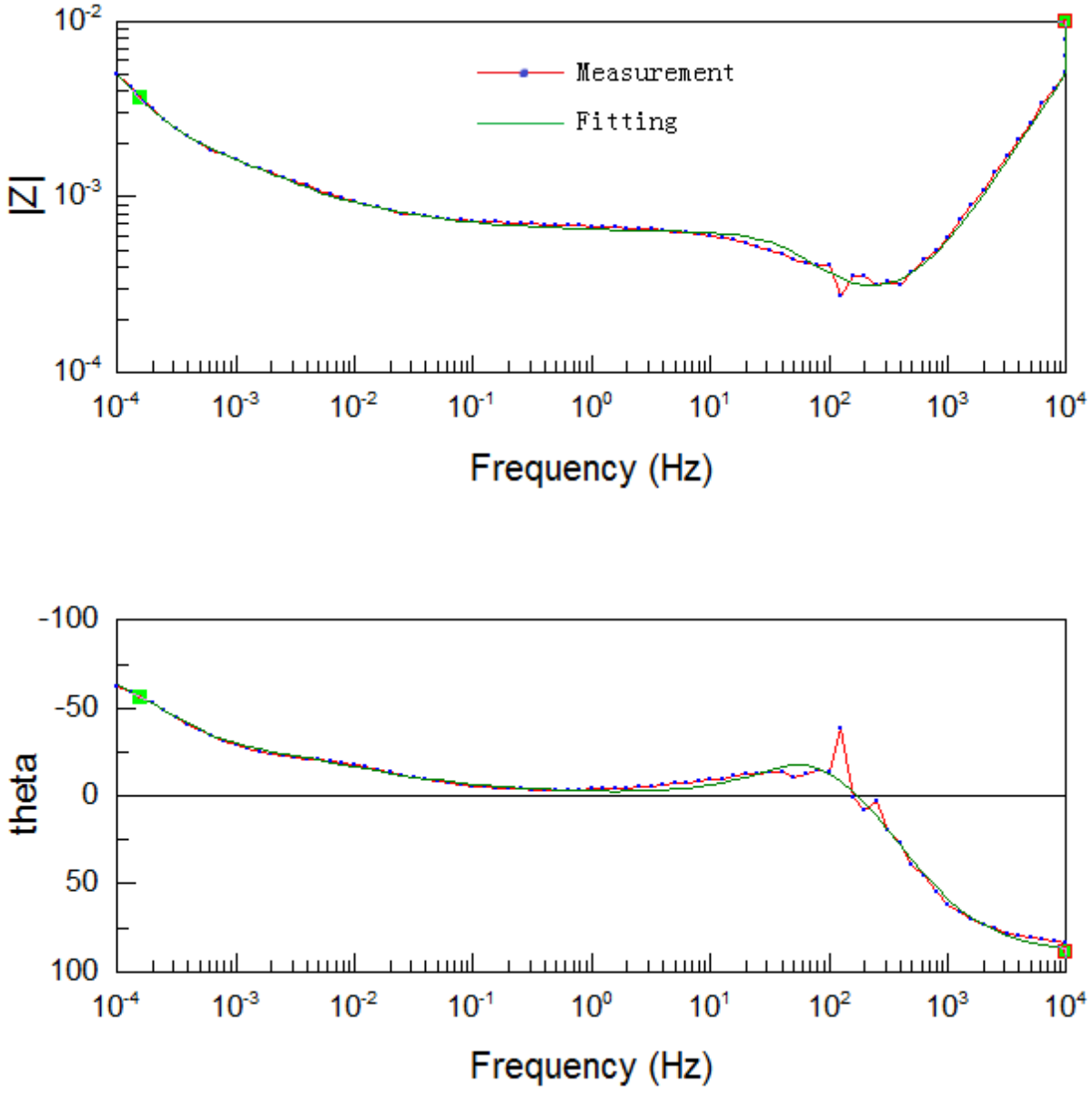

Figure 22: Bode plot – cell A at 3.62V with 1A ac sweep current

The parameters of this model are shown in Table 3 and Table 4.This complex model represents the battery cell as a parallel combination of transmission lines with different lengths, which is why the three parallel Warburg elements have different time constants *W-T*. For more fitting results, please refer to appendix B.2.

R_1(mΩ)(error%)	L_1(H)(error%)	R_{ct}(mΩ)(error%)	C_1(F)(error%)
0.31(1.81)	7.92E-8(1.05)	0.23(3.07)	12.78(7.96)

Table 3: Complex model parameters at 3.84V for cell A using circuit from Figure 20– 1

	W_1(error%)	W_2(error%)	W_3(error%)
W-R(mΩ)	59.3(489.87)	5.57(92.16)	7.89(120.91)
W-T(s)	16821(1071.9)	282.2(70.982)	814.1(85.09)
W-P	0.5	0.5	0.5

Table 4: Complex model parameters at 3.84V for cell A using circuit from Figure 20 - 2

The interest of this thesis is to produce a time domain model which not only captures the general characteristics of the cell, but also accounts for the non-linear behaviour. The models proposed in section 4.1and 4.2 are linear models. Therefore a Simulink nonlinear model is proposed in section 4.3.

4.3 Time domain Simulink model

As mentioned in the introduction, the goal of this thesis is to develop a model which can be integrated into other existing models to perform system level analysis. Section 4.1 introduced a simple Randle circuit model, which will be developed into a nonlinear time domain model in this section. The model introduced in section 4.1, rather than the one introduced in section 4.2, is used as the basis for the nonlinear model because it is easier to start with than the more complicated model shown in Figure 20. The proposed nonlinear equivalent circuit model is shown in Figure 23.

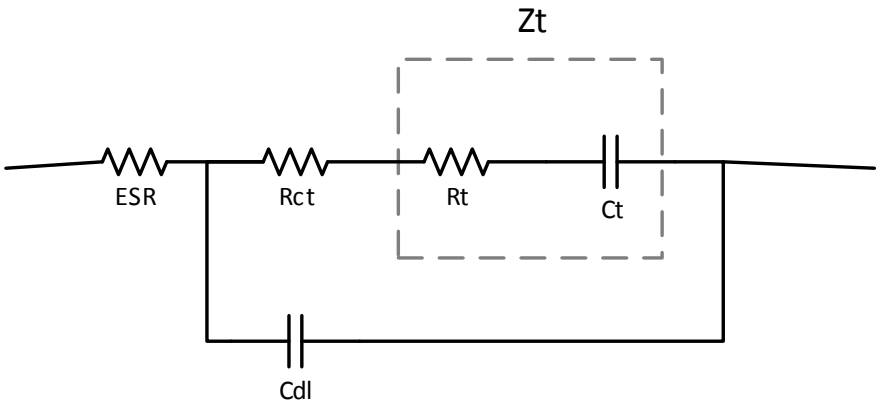

Figure 23: Nonlinear model equivalent circuit

ESR represents the equivalent series resistance, which also accounts for the contact resistance as well as internal resistance. R_{ct} is the charge transfer resistance. C_{dl} is the double layer capacitance. The Warburg element in the frequency model is represented by a transmission line block in Figure 24, which is the Z_t in Figure 23. To model the transmission line block, we start with the simplest model, in which the transmission line is simulated by a series RC combination. The detailed blocks inside *ESR*, $R_{ct,}$ $C_{dl,}$ R_t and C_t can be found in Appendix C . The MatLAB/Simulink model is shown in Figure 24.

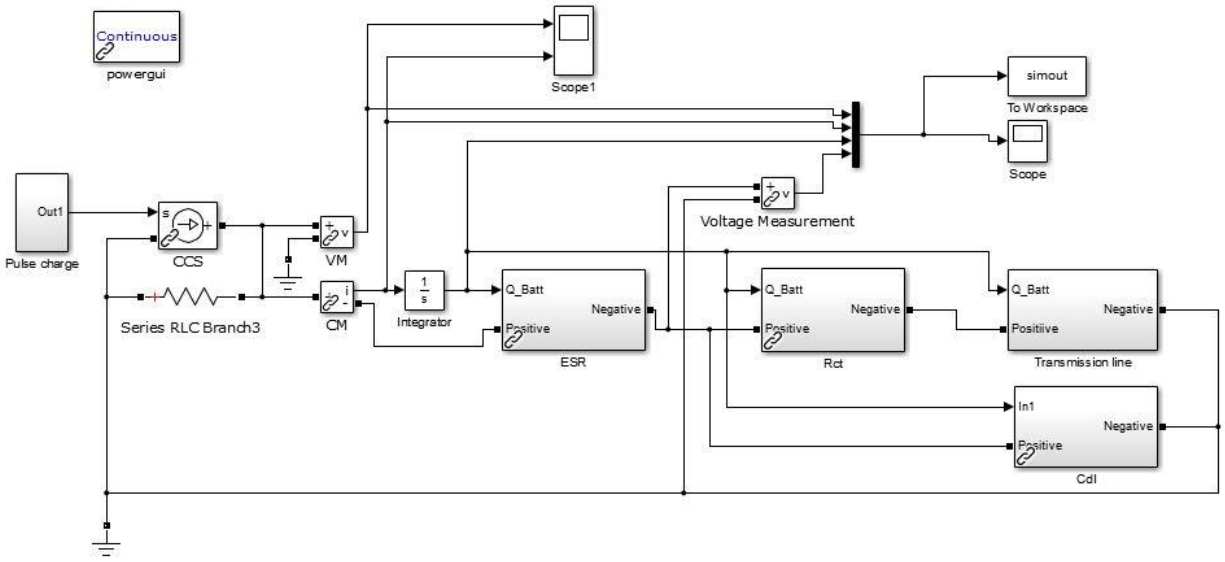

Figure 24: Nonlinear circuit simulink model

The Simulink model shown in Figure 24 is based on the equivalent circuit shown in Figure 23. Starting from the very left of Figure 24, the *Pulse Charge* block generates step changes to simulate the charge/discharge current. To its right, *CCS* stands for controlled-current-source. *CCS* outputs a controlled constant current whose magnitude is set by the *Pulse Charge* block. The current flows into two more blocks on the right which are *VM* and *CM*. *VM* stands for voltage measurement. It is measuring the voltage of the battery terminal with respect to ground. *CM* stands for current measurement, which is measuring the current flowing into the battery cell. Following the current measurement block, the integrator to its right counts how many coulombs have been fed into the cell and calculates the total charge stored in the battery. The total charge, Q, is being fed into the equivalent series resistance, *ESR*, and then divided between the branch containing R_{ct} and the, Transmission line block (contains R_t and C_t) and the branch with the double layer capacitance, C_{dl}. *ESR*, $R_{ct,}$ $C_{dl,}$ R_t and C_t are all voltage dependent. In each of the nonlinear blocks, Q is used in look-up tables to find the corresponding values at different states

of charge. For example, in *ESR* a look-up table for Q-R is used to find the series resistance at various SoCs. Similarly, a look-up table for Q-C is used in C_{dl} to find the equivalent capacitance at different potentials. *ESR*, R_{ct}, R_t and C_{dl} use the values from the R_1, R_{ct}, *W-R* and C_{dl} in the simple frequency domain model, respectively; whereas values for C_t are the data points of cell-voltage vs. charge accumulated in the cell, and these data points can be extracted from the slow can charge test. Linear interpolation is used for curve fitting between data points for the look-up tables. The values for each lookup table can be found in appendix D.

4.4 Model validation and modification

This section focuses on the validation of the nonlinear Simulink model. Using the validation data generated from various tests, the model's performance and accuracy is verified and analyzed. Followed by the validation, the model's sensitivity to its elements parameters are investigated and presented. Finally, based on the validation results and the sensitivity test, the model is modified to provide the most accurate result without increasing its numerical computational cost.

4.4.1 Model validation results

The model is validated using several test datasets, including the partial and pulse charge/discharge. Figure 25 and Figure 26 are model fitting results from pulse charge and partial discharge, respectively.

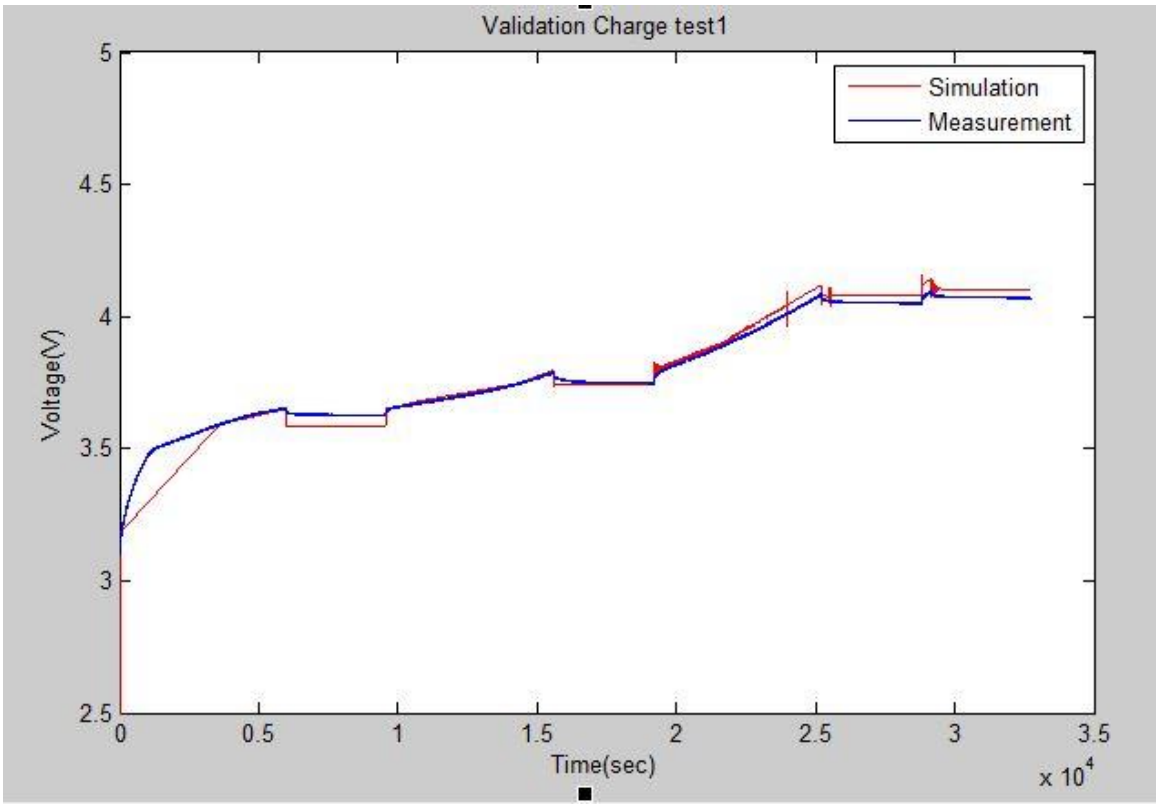

Figure 25: Pulse charge validation

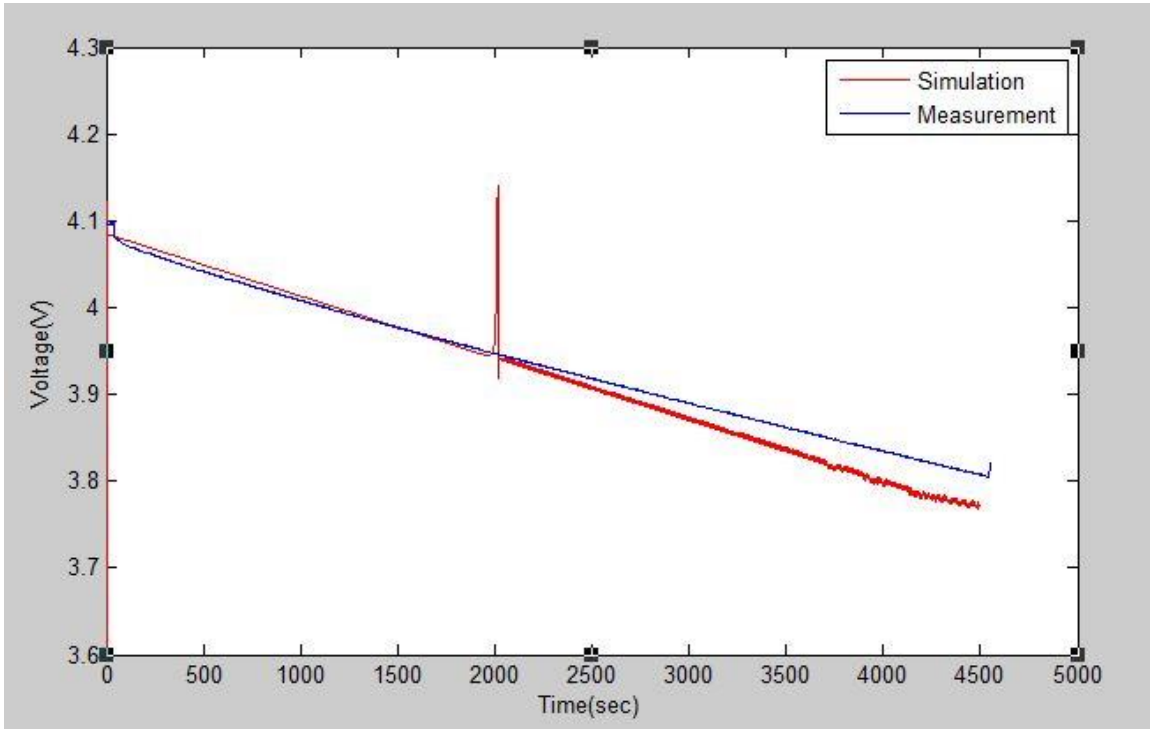

Figure 26: Partial discharge validation

4.4.2 Fitting result analysis

The fitting results are analyzed and the model is modified to provide better fitting results based on the analysis. The model undergoes the sensitivity test to see how the circuit elements parameters affect the accuracy. The limitations of the model are also explored after the sensitivity test.

4.4.2.1 Analysis

It is observed that in both Figure 25 and Figure 26, the simulation voltages start at a much lower value than the measured cell voltage. The model performs best in the range of 3.6V to 3.9V. At the lower end, the model tends to rise slower than the measurement data; and towards the higher end, the model produces higher voltage output than the experiment data. There are spikes in the simulation result, which usually occur after switching on or off the current. Figure 26 also shows the simulation result is noisy following the spike.

The spikes and noise are suspected to be caused by the double layer capacitance. After removing the double layer capacitance, the simulation result is smoother as shown in Figure 27 and Figure 28. However the accuracy of the model is not affected by removing C_{dl}, which leads to the prediction that the accuracy of the model purely depends on the accuracy of the element parameters.

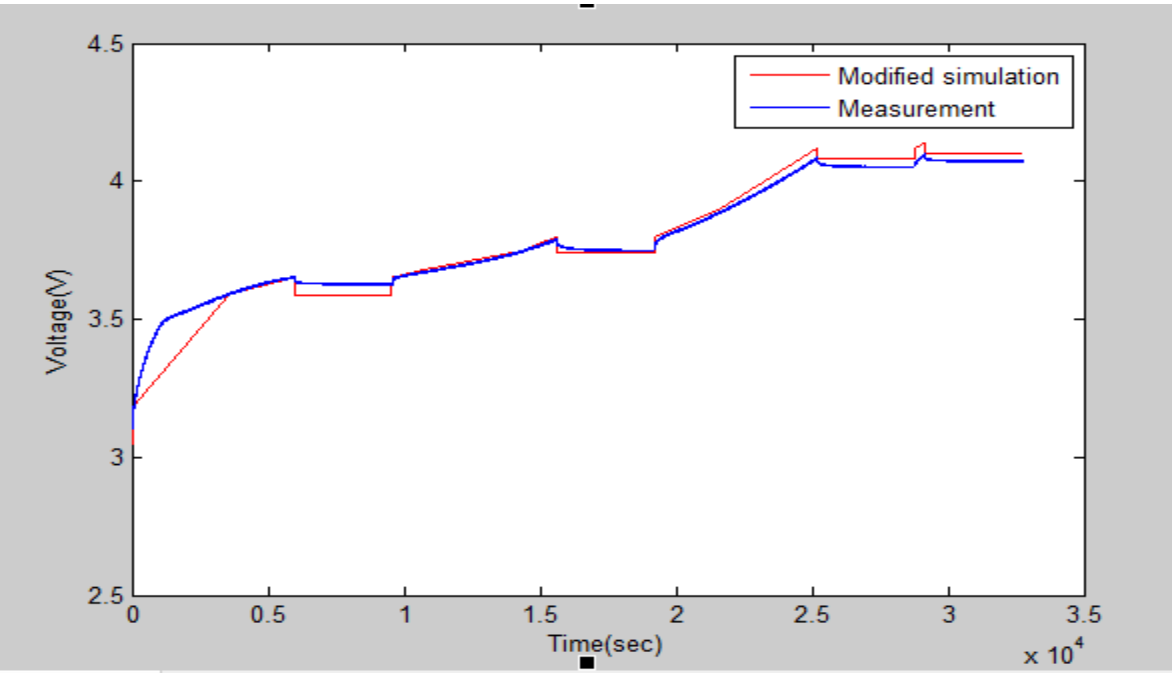

Figure 27: Modified model simulation result

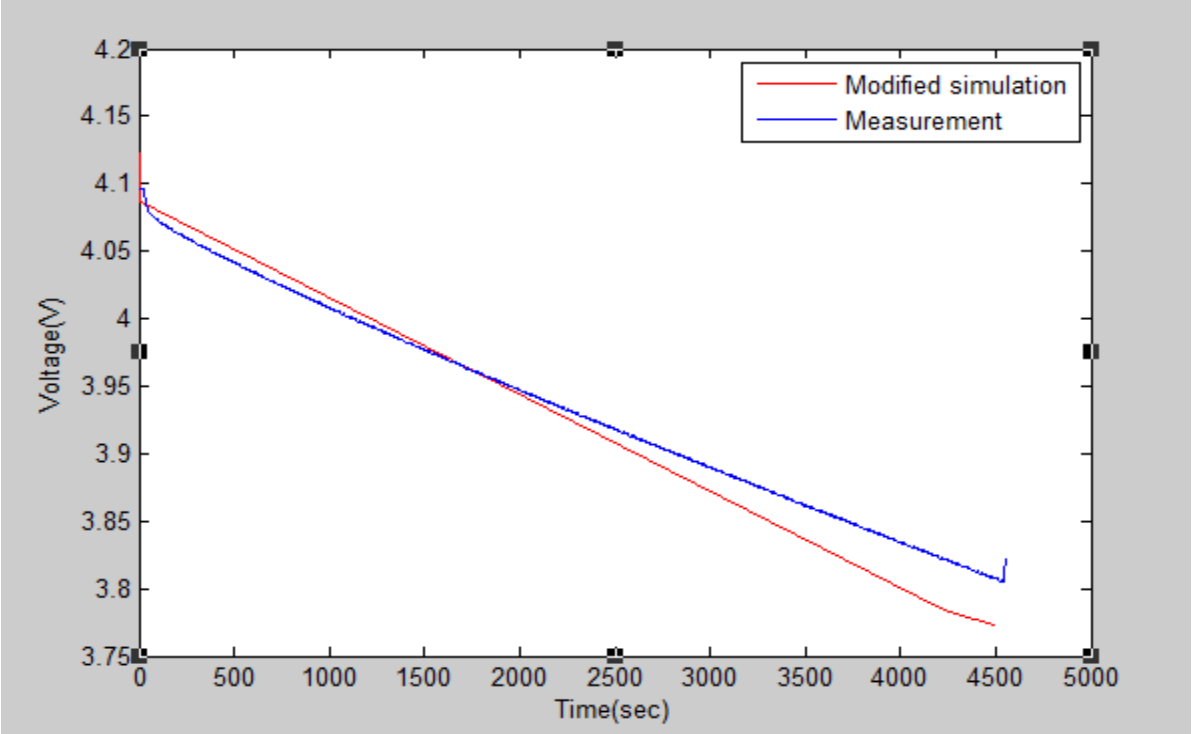

Figure 28: Modified model simulation result 2

4.4.2.2 Final version of the proposed model

C_{dl} is on the order of 10 and its associated time constant is less than 10ms since R_{ct} is less than 0.3 mΩ. On time scale that is much longer than 10ms, C_{dl} is not relevant. Following the discussion in section 4.4.2, C_{dl} is removed and more data points are added in C_t to the original proposed model to remove the spikes and noise.

Although it is believed that more segments of the transmission line elements can be added into the model to improve the accuracy, it is found that by implementing more segments, the compilation time rises significantly. It also increases the stiffness of the system which causes the reduction in stability of the model. The final version of the proposed model is shown in Figure 29.

Figure 29: Final version of proposed model

The proposed model in Simulink is shown in Figure 30.

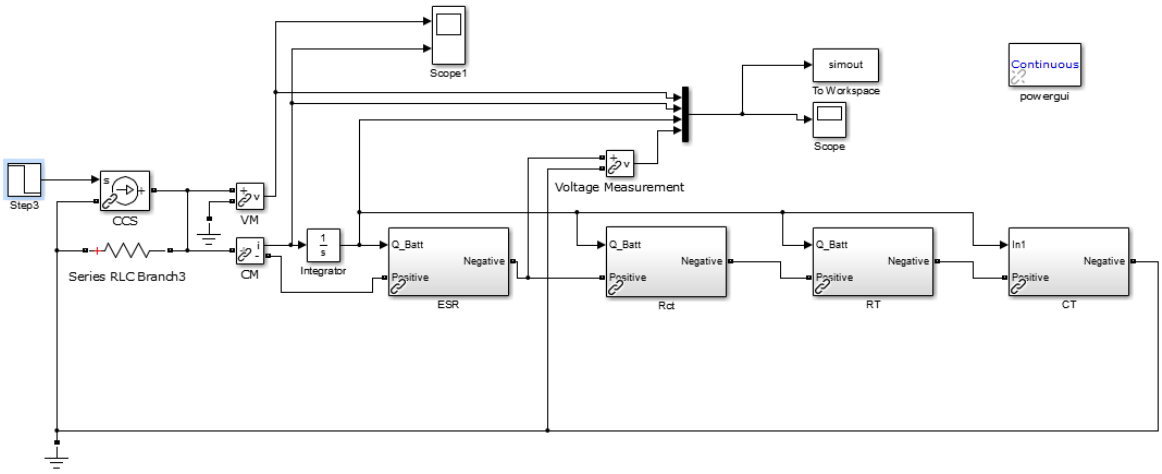

Figure 30: Final proposed Simulink model

The result is illustrated in Figure 31.

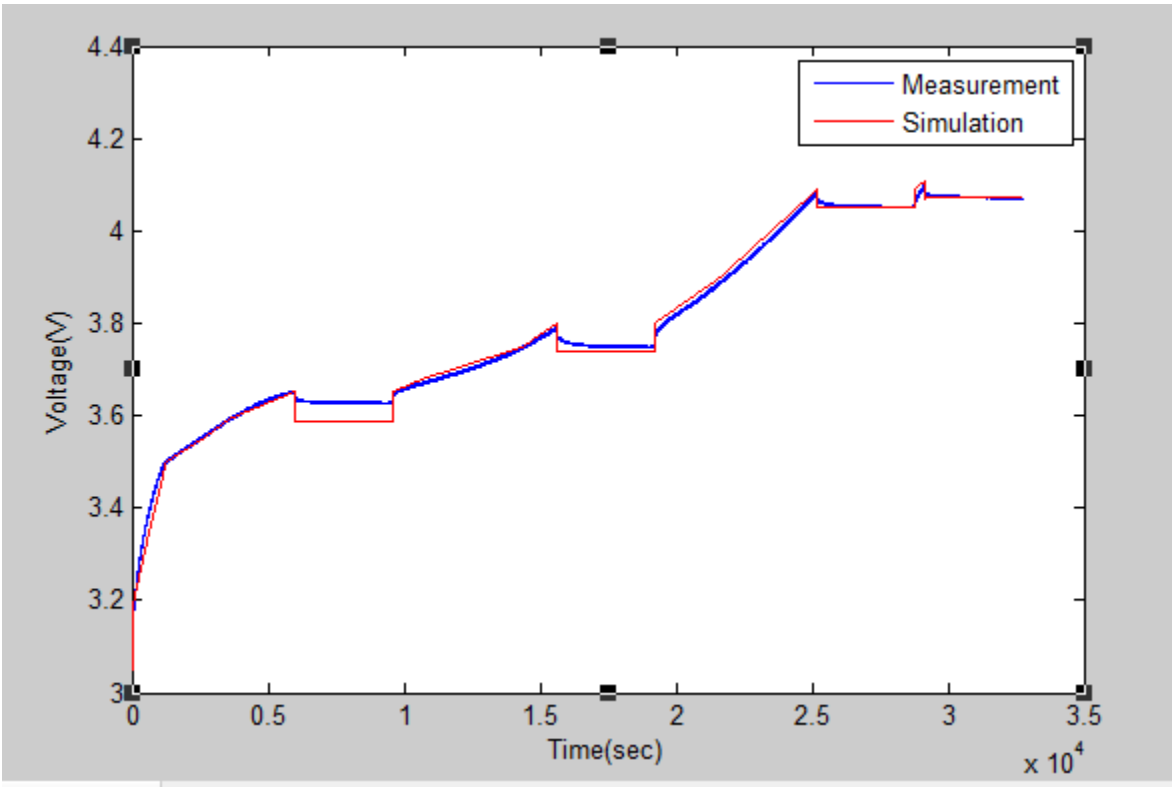

Figure 31: Final model simulation result

Inserting more data points in C_t has improved the fitting results. The rapid change seen in between 3.2V and 3.5V in Figure 31 can be related back to Figure 12. In Figure 12, it can be seen that the capacitance is at its lowest value. The slope becomes flatter in the region of 3.5V to 3.7V, which corresponds to an increase in the capacitance shown in Figure 12. After the first resting period, the slope between 3.7V to 3.75V is close to that of the region of 3.5V to 3.7V, since the capacitance is at its peak value in this region. As the cell voltage goes over 3.8V, the slope starts to become steeper as the capacitance starts to decrease. The rapid change in the region of 3.8V to 4.1V is again due to the low capacitance in this region. Caution must be taken when relating Figure 12 and Figure 31. The measurement shown in Figure 31 is taken under 15A constant current, whereas the data shown in Figure 12 is taken under 3A constant current. The difference in the supplied current will introduce different over-voltages caused by the resistance illustrated in Figure 29.

In the first relaxation period, there is a mismatch between the simulation and the measurement. Two possible explanations for the mismatch are: (1) this might have been caused by a long decay time constant which is not accounted for by the proposed model; (2) the resistance estimation in this region is not accurate. All four relaxation periods show signs of exponential decay after the current are switched off. The proposed model cannot predict the decay and it is believed that another RC time constant is needed in the model in order to account for the decay.

4.4.2.3 Sensitivity test

It is desired to see how sensitive the simulation is to the parameter variations. To investigate the sensitivity of the model, the values in the look-up tables for each circuit element are first increased by 1% and then decreased by 1%. It is found that varying the values of *ESR*, R_{ct} and R_t

have negligible effect on the simulation whereas the variation in C_t has a great impact on the modeling results. Using the extract parameters from Table 2, the sum of the resistances *ESR*, R_{ct} and R_t can be crudely estimated to be 30 mΩ. Referring back to the circuit shown in Figure 29, it can be observed that under a constant current of 15A, the total voltage drop on these resistances is 450mV. A 1% change in the resistances will introduce 4.5mV change in the voltage drop across the resistors. From Figure 12 it can be seen that the capacitance is on the order of mega farads. A 1% change in C_t will introduce a difference of 10kF in capacitance. 4.5mV of voltage change is irrelevant when the circuit response is dominated by the capacitor. The comparison between the original and the adjusted model with different C_t values are shown in Figure 32.

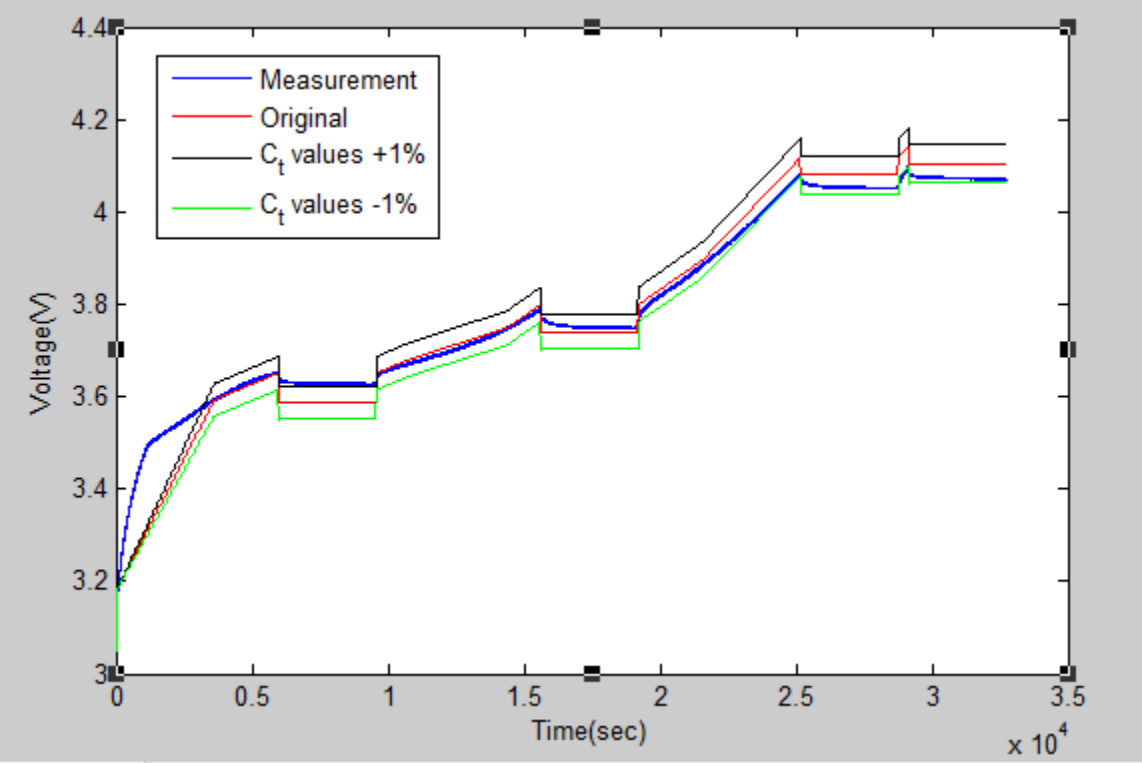

Figure 32: Comparison between different Ct parameters

C_t values are obtained from the constant current charge test and the values are directly associated with the capacity of the cell. C_t can be used to help to identify the SoC of the battery, which also

implies that the simulation accuracy lies heavily on the test data used to extract $C_{t.}$ The importance of the accuracy of $C_{t.}$ leads to the discussion of the model's limitations in the next section.

4.4.2.4 Limitations

Since the model is an experiment extracted physical model, its validity and accuracy are highly dependent on the tests data which contains uncertainties and errors. The modeling results' sensitivity to $C_{t.}$ indicates that the model is also chemistry dependent. For instance, given a different cell with a different charging profile, the values for $C_{t.}$ are expected to change considerably, resulting in the loss of accuracy in the simulation results. This dependency on $C_{t.}$ limits the usefulness of this model. In addition to the dependency on $C_{t.}$, the model lacks the ability to accurately predict the relaxation period as shown in Figure 27.

Chapter 5: Conclusion

This chapter concludes the findings, summarizes the entire thesis and discusses the future work for the continuation of this project.

5.1 Conclusion of the findings

The primary finding of this thesis is the significance of the nonlinear equivalent capacitance. It is found that the accuracy of the estimation of the capacitance greatly affects the simulation result during the charging/discharging process. During the relaxation, the accuracy of the resistance estimation plays an important role in determining the fitting result's accuracy. At the time scale considered for the model's application, the double layer capacitance is not significant since the RC time constant associated with it is much smaller than that of the equivalent capacitance. However, because the proposed model only has one RC time constant, it is not able to predict the decay after the current is switched off. This suggests that the model requires more than one transmission line segment to fully capture the behaviour of the cell.

The model proposed in this thesis can be linked back to the physical reactions in the cell. The disadvantage of the physical model is that its accuracy heavily depends on the circuit elements parameters, which will require precise measurement. This implies that for different cell chemistry, the parameters will need to be re-established in order to provide accurate fitting results. The chemistry dependence of the proposed model will limit its application in industry.

5.2 Summary

In this thesis, a lithium ion battery cell was studied. The testing procedure and setup were explained in detail and the extracted battery models were discussed.

In Chapter 2, work in the field of lithium-ion battery modelling done previously by other researchers was explored. The advantages and disadvantages of each type of model were reviewed and evaluated. It was concluded that, various battery models were built upon the fundamental models which were reviewed in Chapter 2. For this thesis, the impedance based model was chosen as the fundamental model to work with and build upon.

The experimental design, setup and results were presented in Chapter 3. Since the impedance based model was chosen as the fundamental model, the EIS test was carried out to obtain data required to extract the battery model. The cell also went through cycles of constant current charge and discharge, as well as pulse charge and discharge. The data obtained from these tests was used to validate the model. The experimental results were presented and briefly explained.

Following the discussion of the experimental results in Chapter 3, the data were further analysed in Chapter 4. Three battery models, as well as the fitting results for each model, were presented. It was shown that the simple linear frequency domain model extracted from the EIS data using ZView2 produced very good fitting results in Bode plots. However, it could not fit to the low frequency response in Nyquist plot. Although not accurate at the very low frequency, the simple model does offer simplicity and a reasonable degree of accuracy. To capture the very low frequency response in Nyquist plot, a more complex frequency domain model was developed. Though the physical explanation of the slope of the Nyquist plot at very low frequency was still unclear, the model introduced in section 4.2 demonstrated the potential of explaining the behaviour using multi-lengths transmission lines. This more complex model produced very good fitting results at all frequency ranges. Both the simple and the complex modified Randle circuit model were linear models in frequency domain which could not be used in system level

modeling, and therefore a nonlinear time domain model was proposed. The nonlinear model's parameters were extracted from the EIS tests and the slow charge test. Upon analyzing the validation results, C_{dl} was taken out from the nonlinear model and more data points were inserted into C_t to produce the best fit while maintaining its simplicity.

5.3 Future work

There are several areas which can be explored further to both improve the battery model and the understanding of the lithium ion battery. In particular, the following two areas can be investigated further: using the extracted equivalent capacitance to develop a modified Zimmermann model and to include temperature effect into the model. While the physical model offers insight into the chemistry of the cell and enhances the understanding of lithium-ion technology in general, the modified Zimmermann model presented in [31] has the advantage of chemistry independency and simplicity, in comparison to the complicated physical model which usually involves many different elements and various parameters. Another area which is worthy of further study is to be able to predict how the battery performs under different temperature.

References

[1] L. Benini et al., "Extending lifetime of portable systems by battery scheduling," in *Design, Automation and Test in Europe, 2001. Conference and Exhibition 2001*, Munich, 2001, pp. 197-201

[2] J. Cao et al., "Battery Balancing Methods: A Comprehensive Review," in *Vehicle Power and Propulsion Conference (VPPC), 2008 IEEE*, Harbin, 2008, pp. 1-6

[3] D. Linden and T.B. Reddy, "Primary Batteries—Introduction," in *Handbook of Batteries*, 3rd ed., McGraw-Hill, 2001, ch2, sec. 6, ch. 7, sec. 3

[4] H.A. Kiehne et al., "Electrochemical Energy Storage," in *Battery Technology Handbook*, 2nd ed., New York: Marcel Dekker, INC., 2003, pp. 2-40

[5] M. Wakihara and O. Yamamoto, "General Concepts," in *Lithium Ion Batteries: Fundamentals and performance*, Kodansha Ltd., and Wiley-VCH, 1998, pp. 2-3

[6] S. Rodrigues et al., "A review of state-of-charge indication of batteries by means of a.c. impedance measurements," *Journal of Power Sources*, vol. 87, issues 1-2, pp. 12-20, April 2000.

[7] T.M. Bandhauer et al., "A Critical Review of Thermal Issues in Lithium-Ion Batteries," *Journal of the Electrochemical Society*, January 2011.

[8] C.E. Chiasserinit and R.R. Rao, "A model for battery pulsed discharge with recovery effect," in *Wireless Communications and Networking, IEEE Conference - WCNC*, 1999, pp. 636-639

[9] X. Feng and Z. Sun, "A battery model including hysteresis for State-of-Charge estimation in Ni-MH battery," in *Vehicle Power and Propulsion Conference (VPPC), 2008 IEEE*, Harbin, 2008, pp. 1-5

[10] J. Zhang et al., “An enhanced circuit-based model for single-cell battery,” *Applied Power Electronics Conference and Exposition (APEC), 2010 Twenty-Fifth Annual IEEE,* Palm Springs, CA, 2010, pp. 672-675

[11] M. Chen and G.A. Rincón-mora, “Accurate Electrical Battery Model Capable of Predicting Runtime and I-V Performance,” *IEEE Trans. Energy Convers.*, 2006.

[12] D. Doerffel and S.A. Sharkh, “A critical review of using the Peukert equation for determining the remaining capacity of lead-acid and lithium-ion batteries,” *Journal of Power Sources*, vol. 155, issue 2, pp. 395-400, April 2006.

[13] A. Hausmann and C. Depcik, “Expanding the Peukert equation for battery capacity modeling through inclusion of a temperature dependency,” *Journal of Power Sources*, vol. 235, pp. 148-158, August 2013.

[14] L. Benini et al., “Discrete-time battery models for system-level low-power design,” *IEEE Trans. Very Large Scale Integr. (VLSI) Syst.*, vol. 9, issue 5, pp. 630-640, October 2001.

[15] A. J. Bard and L. R. Faulkner, “Introduction and overview of electrode processes,” in *Electrochemical methods – Fundamentals and Applications,* 2nd ed., John Wiley & Sons, INC., 2001, pp. 23-25

[16] *Basics of Electrochemical Impedance Spectroscopy* [Online]. Available: http://www.gamry.com/application-notes/basics-of-electrochemical-impedance-spectroscopy/

[17] R. Rao et al., “Battery Modeling for Energy-Aware System Design,” *IEEE J. Comput. Aid. Des.*, vol. 36, no. 12, pp. 77-87, 2003.

[18] M.R. Jongerden and B.R. Haverkort, “Which battery model to use?” *Software, IET,* vol. 3, issue 6, pp. 445-457, 2009.

[19] T. Kim, “A Hybrid Battery Model Capable of Capturing Dynamic Circuit Characteristics and Nonlinear Capacity Effects,” M.S. thesis, Dept. Elect. Eng., Univ. of Nebraska, Lincoln, NE, 2012.

[20] L. Benini et al., “A discrete-time battery model for high-level power estimation,” in *Design, Automation and Test in Europe Conference and Exhibition 2000,* Paris, 2000, pp. 35-39

[21] K.M. Tsang, “Lithium-ion Batteries models for computer simulation,” in 2010 *IEEE International Conference on Automation and Logistics (ICAL),* Hong Kong and Macau, 2010, pp. 98-102

[22] C. Chiasserini and R. Rao, “Energy efficient battery management,” *IEEE J. Sel. Areas Commun.*, vol. 19, issue 7, pp. 1235-1245, July 2001.

[23] L. Lam et al., “A practical circuit-based model for Li-ion battery cells in electric vehicle applications,” in *Telecommunications Energy Conference (INTELEC), 2011 IEEE 33rd International,* Amsterdam, 2011, pp. 1-9

[24] H. He et al., “Comparison study on the battery models used for the energy management of batteries in electric vehicles,” *Energy Conversion and Management,* vol. 64, pp. 113-121, 2012.

[25] H.L. Chan, “A new battery model for use with battery energy storage systems and electric vehicles power systems,” in *Power Engineering Society Winter Meeting, 2000. IEEE,* 2000, vol. 1, pp. 470-475

[26] S. Buller et al., “Impedance-based nonlinear dynamic battery modeling for automotive applications,” *Journal of Power Sources,* vol. 113, issue 2, pp. 422-430, January 2003.

[27] S. Buller et al., “Impedance-based simulation models of supercapacitors and Li-ion batteries for power electronic applications,” *IEEE Trans. Ind. Appl.*, pp. 742-747, 2005.

[28] D. Andre et al., “Characterization of high-power lithium-ion batteries by electrochemical impedance spectroscopy. I. Experimental investigation”, *Journal of Power Sources,* vol. 196, issue 12, pp. 5334-5341, June 2011.

[29] P. Zoltowski, “A new approach to measurement modeling in electrochemical impedance spectroscopy,” *Journal of Electroanalytical Chemistry*, vol. 375, issues 1-2, pp. 45-47, September 1994.

[30] J.E.B Randles, “Kinetics of rapid electrode reactions”, *Discussion of the Faraday Society*, pp.11-19, 1947

[31] M.P. Cassagne et al., “Comparison between ELAN Test Results and an Improved Zimmerman Model”, European Space Agency Space Power Conference, Tarragona, September 1998.

[32] A. J. Bard and L. R. Faulkner, “Techniques based on concepts of impedance,” in *Electrochemical methods – Fundamentals and Applications*, 2nd ed., John Wiley & Sons, INC., 2001, sec. 10.1.3, p. 376

[33] S. Rodrigues et al., “AC impedance and state-of-charge analysis of a sealed lithium-ion rechargeable battery,” *Journal of Solid State Electrochemistry*, pp. 397-405, 1999.

Appendices

The appendices have the following documents: additional Labview code, frequency domain model fitting results and plots, Simulink model and Simulink parameters.

Appendix A : Labview code

Appendix A includes the Labview code for cycle operation and pulse operation. Please note that the numbers 0123 shown in figures in Appendix A are part of the icon of the function blocks. They are not real inputs and they do not carry any meaning.

A.1 Cycle operation code

Please refer to Figure 5 for the algorithm used to develop this cycle operation control code. The cycle operation code is used to control the test circuit to charge or discharge the cell, and prevent it from being overcharged or over discharged.

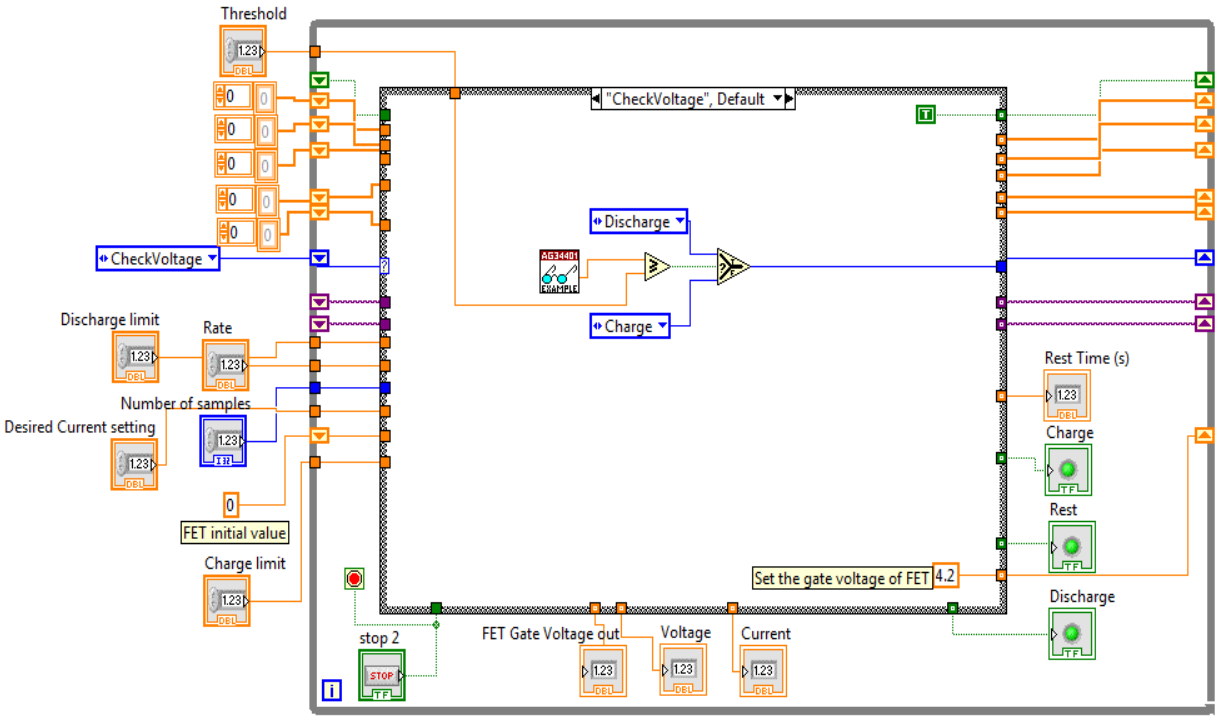

Figure 33: Cycle- Check cell voltage

Figure 33 is the initial state in the flow chart shown in Figure 5. This initial state checks the voltage of the cell by taking a single measurement and decides whether to charge or discharge the cell based on the measurement. In Figure 33, the outer grey loop is a 'while loop', which repeats the instructions inside the while loop at a rate specified by the user. Instructions outside the while loop will be performed only once when the program first runs. The inner grey loop is a 'case structure', which selects different outputs based on the input condition. The icon with 'AG34401' written on its label is a built-in driver for HP34401A meter. The driver sends a command to the HP meter and takes a single measurement, which will be sent back to Labview. 'Threshold', 'Discharge limit', 'Rate', 'Number of samples', 'Desired current setting' and 'Charge limit' are input blocks. The user can set values to initialize these blocks. 'Voltage', 'Current', 'FET Gate Voltage out' and 'Rest time' are output blocks. They provide the user with

new measurement result during each round of iteration. The green blocks ‘Charge’, ‘Rest’ and ‘Discharge’ are LED indicators, which light up when the corresponding operation is selected. The lines are data wires, which carries the data from the previous iteration to the next. For more detailed explanation of the ‘while loop’, ‘case structure’, ‘input blocks’, ‘output blocks’ and ‘data wires’, please refer to the LabVIEW User manual, 2003 edition.

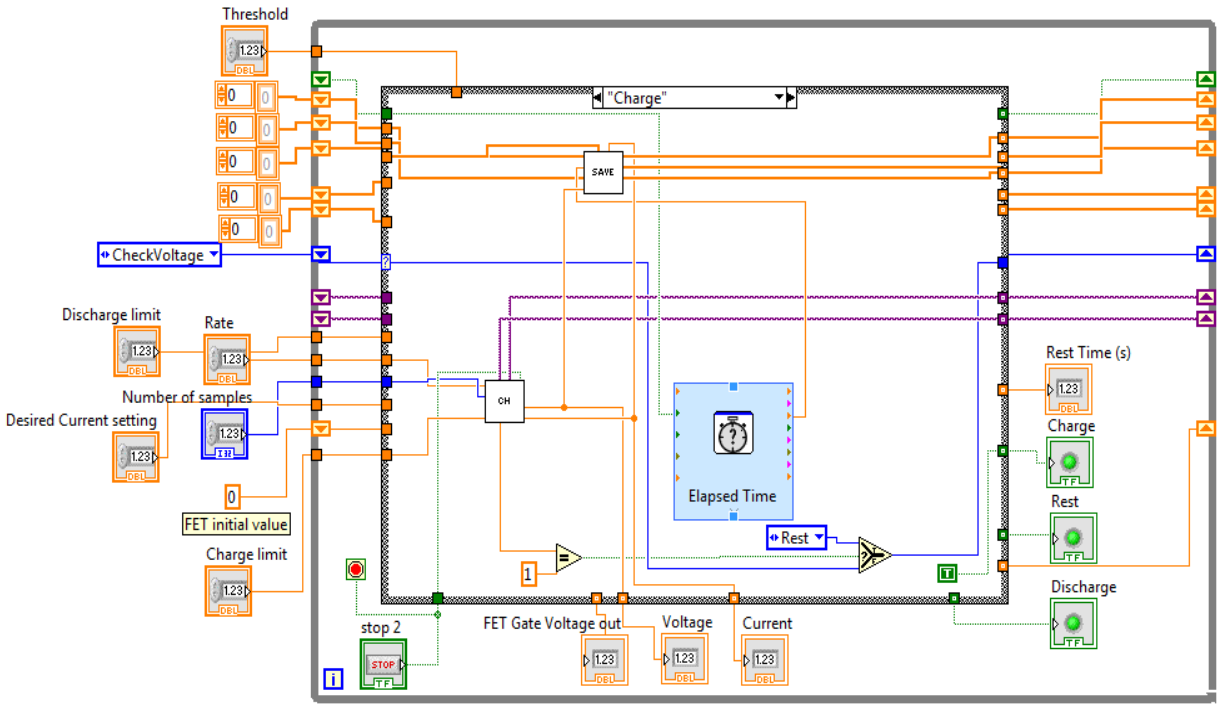

Figure 34: Cycle - Charge cell

Figure 34 is the case when the cell voltage is lower than the threshold and it needs to be charged. ‘CH’ and ‘SAVE’ are user defined function blocks. ‘CH’ is shown in Figure 37. It controls the DAQ card to enable the circuit to charge the cell as well as checking for the overcharge threshold. ‘CH’ also outputs voltage and current measurements taken using the DAQ card. ‘SAVE’ is shown in Figure 40. It stores the data collected during each round of iteration. ‘Elapsed time’ is a block which provides how much time has passed since last round of iteration.

For more information about the function block ‘Elapsed time’, please refer to the LabVIEW User manual, 2003 edition.

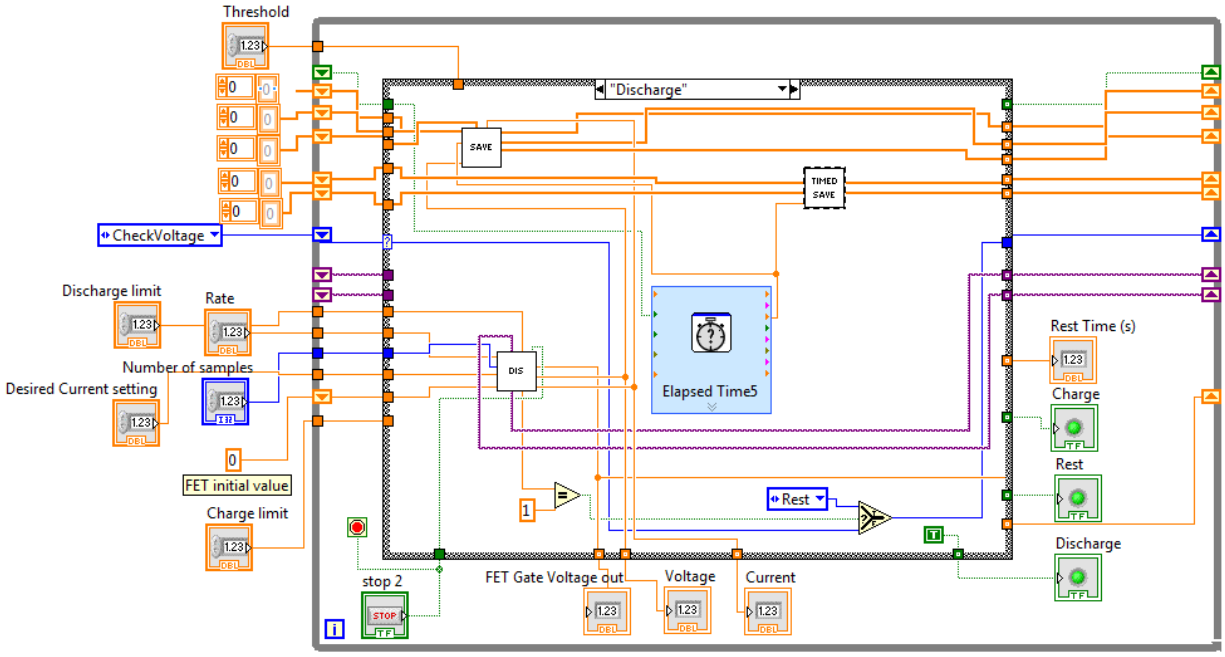

Figure 35: Cycle - Discharge cell

Figure 35 shows the case when the cell’s voltage is higher than the threshold and it needs to be discharged. ‘DIS’ and ‘TIMED SAVE’ are user defined function blocks. ‘DIS’ is shown in Figure 38. It is used to control the circuit to discharge the cell and prevent it from being over discharged by opening the circuit when the cell voltage drops below the discharge limit. ‘DIS’ also outputs voltage and current measurements taken using the DAQ card. ‘TIMED SAVE’ is shown in Figure 39. It saves the data every 10 seconds.

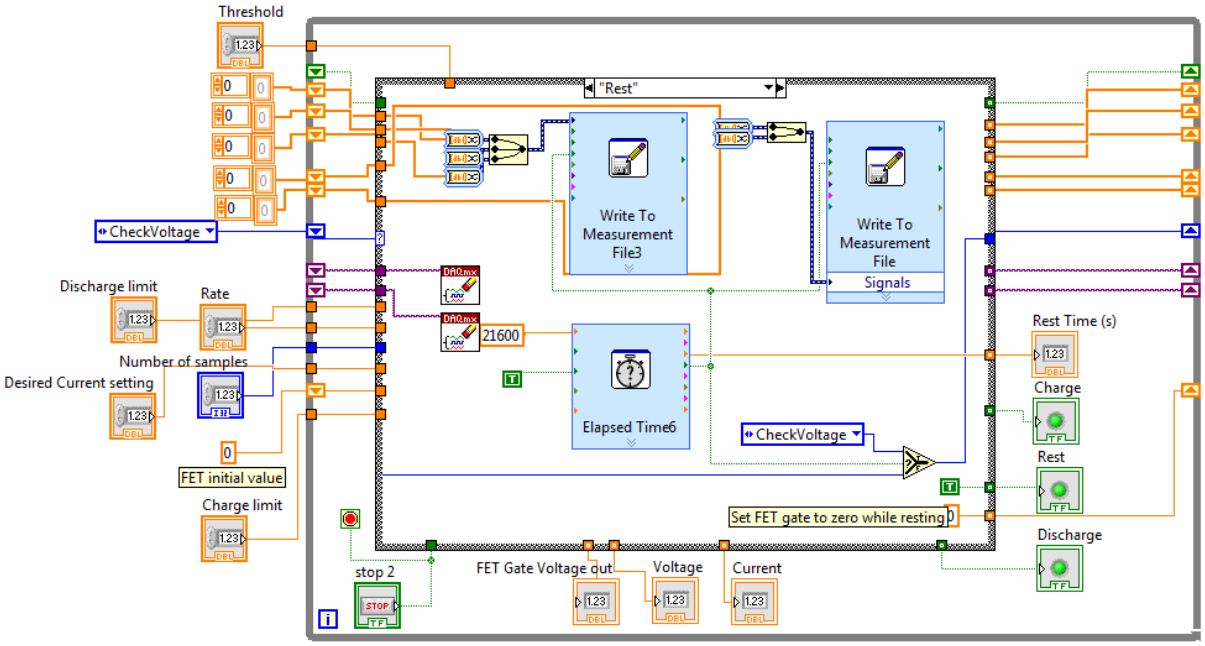

Figure 36: Cycle – Rest state

Figure 36 is the case when the cell has reached the charge or discharge limit. The cell is allowed to rest in open circuit for the amount of time specified by the 'Elapsed Time6' block. The number connect to the 'Elapsed Time6' block is the period for which the cell will be allowed to rest. This number is in seconds and it can be adjusted by the user. The two 'Write to Measurement File' blocks write the stored data into a file on the disk. The format and the name of the destination file can be edited using the 'Write to Measurement File' block. The two blocks with DAQmx written in their icon are DAQ task blocks, 'clear task'. They are used to free the DAQ after charge or discharge operation. For more information about 'Write to Measurement File' and 'DAQmx clear task' blocks, please refer to the LabVIEW user manual, 2003 edition.

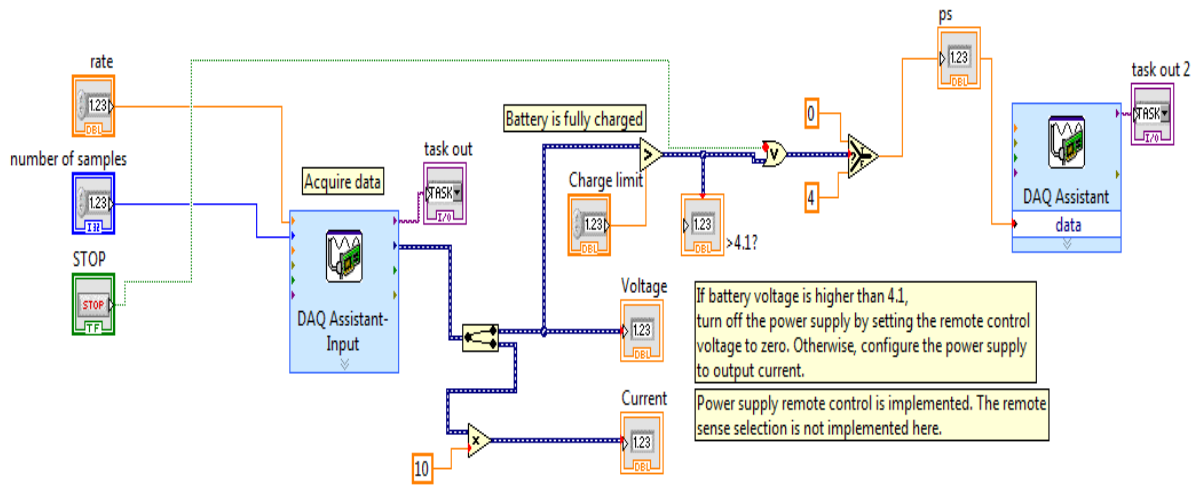

Figure 37: Cycle - SubVI CH

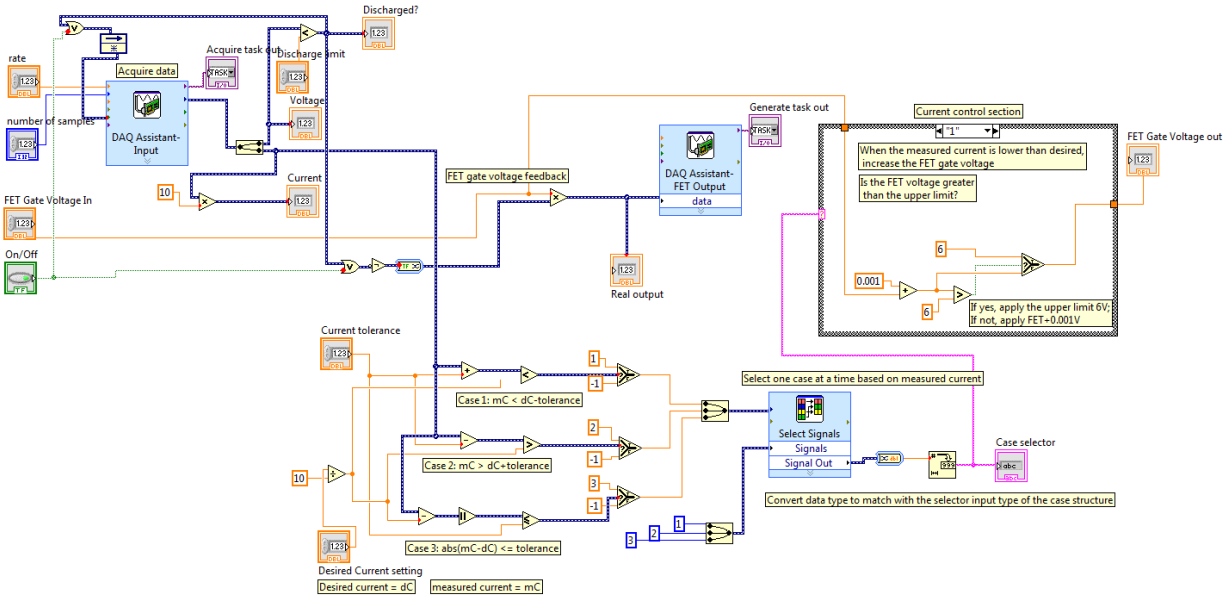

Figure 38: Cycle - SubVI DIS

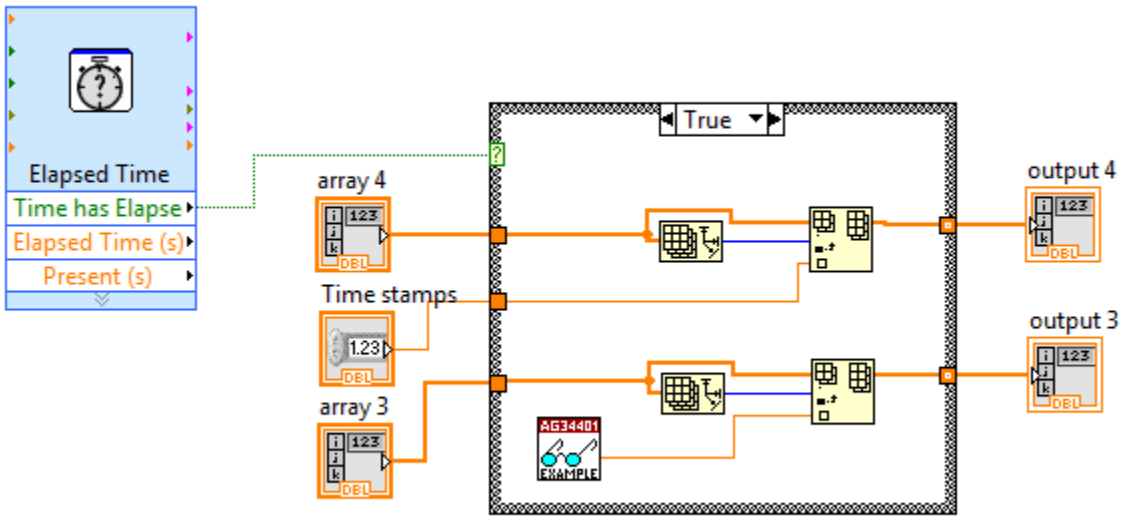

Figure 39: Cycle - SubVI TIMED SAVE

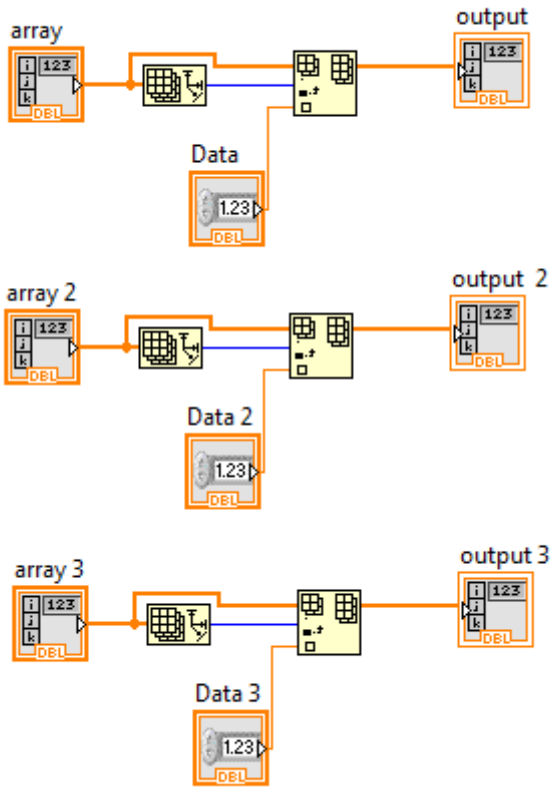

Figure 40: Cycle - SubVI SAVE

A.2 Pulse operation code

Appendix A.2 is the code for the algorithm shown in Figure 7.

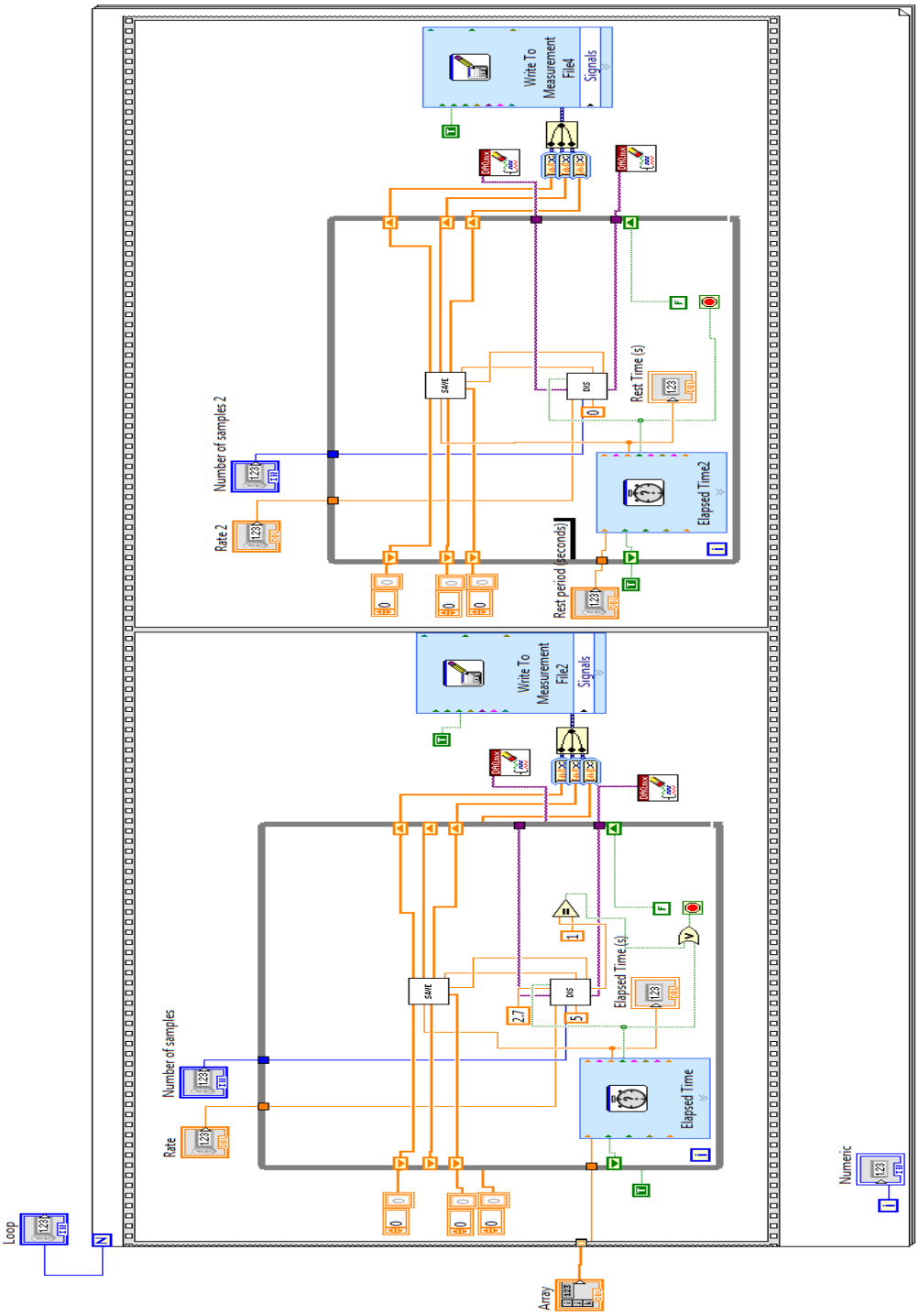

Figure 41: Pulse control

Figure 41 has an outer ‘while loop’ and an inner ‘flat sequence structure’. The ‘flat sequence structure’ performs the actions required in the first frame on the left. Once the actions in the first frame on the left are completed, the ‘flat sequence structure’ moves onto the next frame. The ‘while loop’ repeats the whole *left-to-right frame* sequence. In the left frame, the cell is being either charged or discharged, depending on the user specified limit setting. The program moves to the right frame once the time specified in the left frame has passed, or the cell has reached the voltage limit. In the right frame, the cell is allowed to rest for an hour. For more information on the ‘flat sequence structure’, please refer to the LavVIEW user manual, 2003 edition.

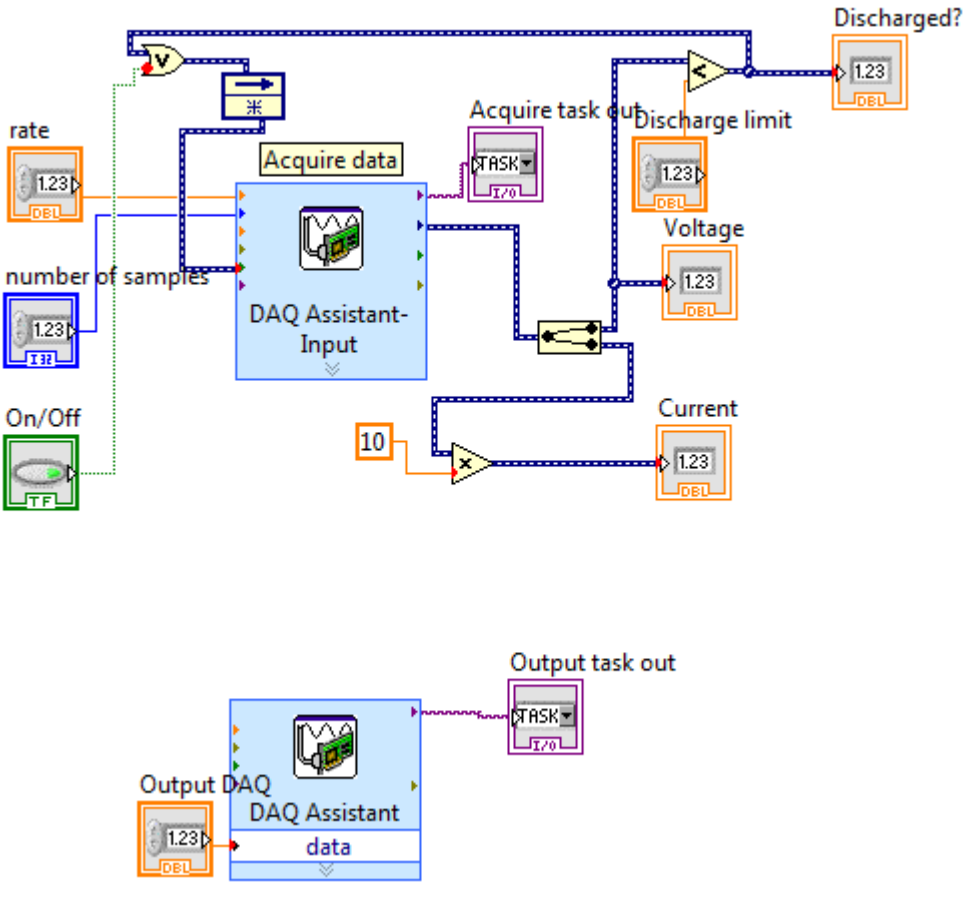

Figure 42: Pulse - SubVI DIS

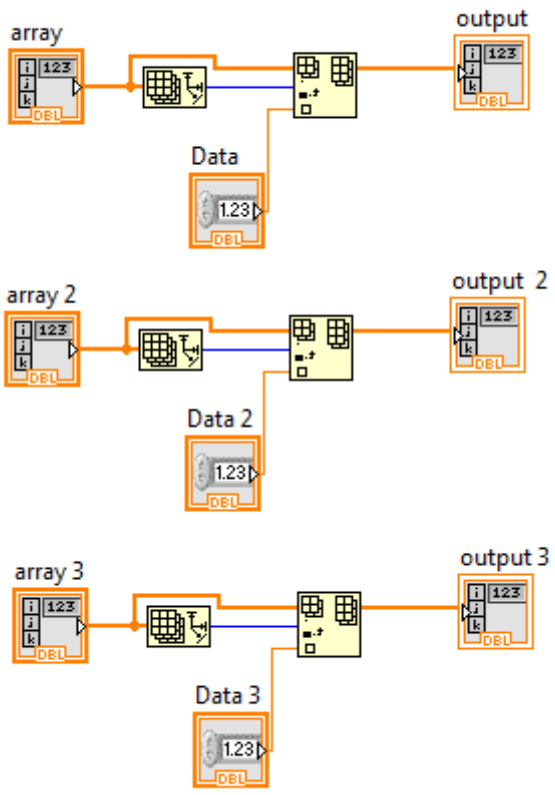

Figure 43: Pulse -SubVI SAVE

.

Appendix B : EIS data and fitting results

Note: the fitting parameters shown in Appendix B have the following units:

Resistor elements(R): Ohms Ω

Inductor elements (L): Henry H

Capacitor elements (C): Farad F

Time constants (T): Seconds s

B.1 Simple frequency domain model fitting results

B.1 includes the fitting result for the model introduced in section 4.1. The electrochemical impedance spectroscopy (EIS) experiment carried out has not reached a low enough frequency where the cell behaves similar to a pure capacitor, in which case the nyquist plots will have a negative 90 degrees slope at low frequency. This implies that the EIS test has not reached a point where the time constant of the cell can be extracted with high accuracy. The mismatch at low frequency shown in this section is likely due to the wrong estimation of the time constant(s) of the cell.

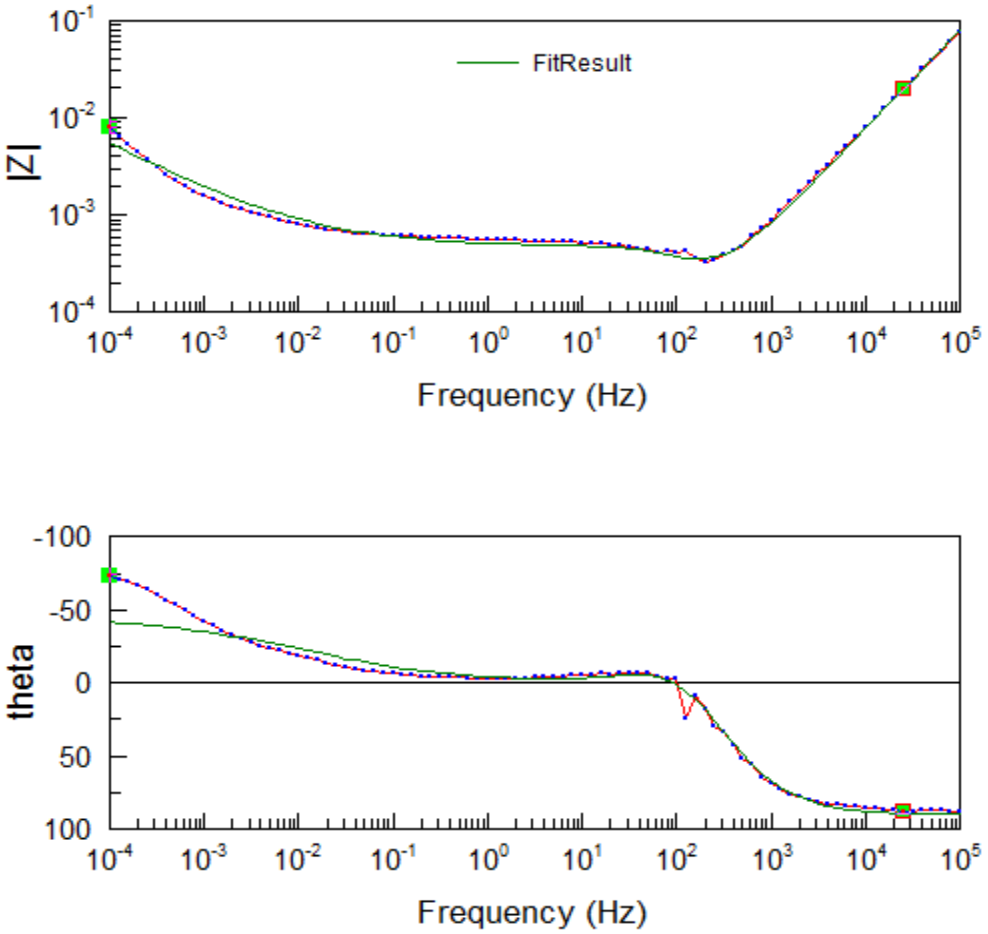

Figure 44: Bode plot of cell A at 4.08V

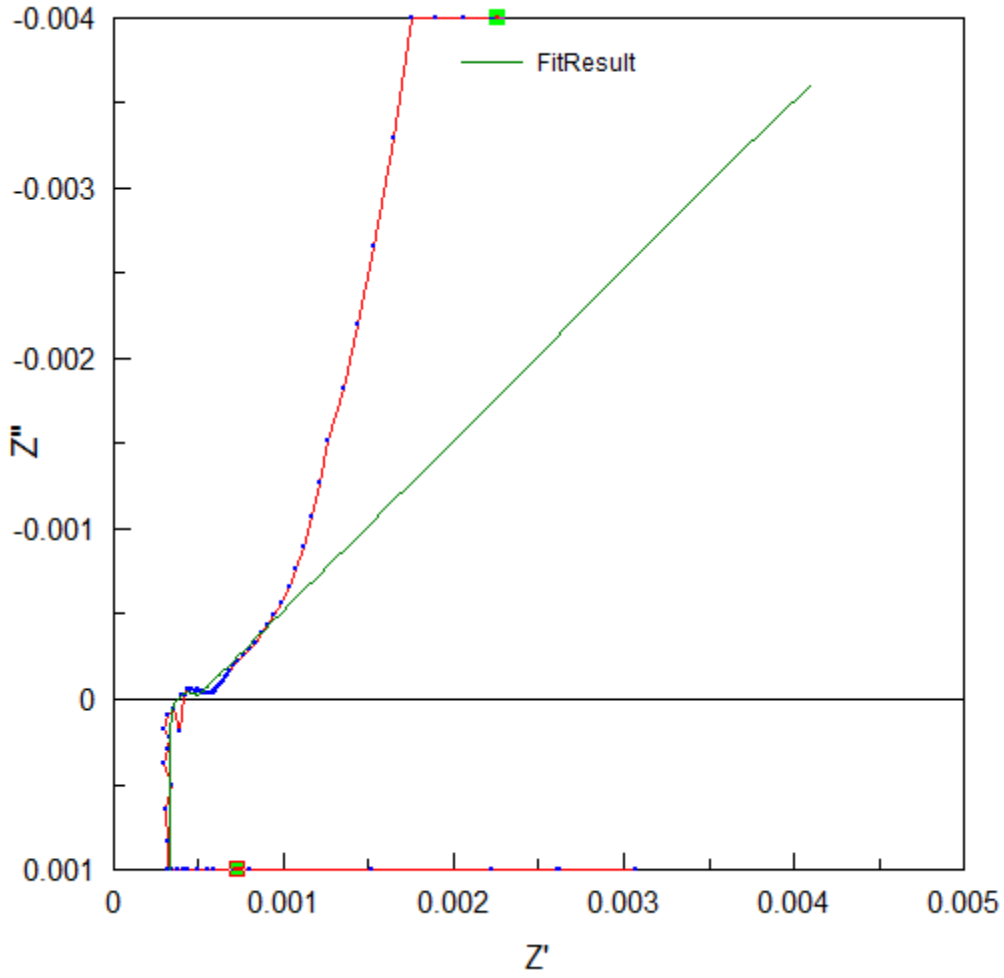

Figure 45: Nyquist plot of cell A at 4.08V

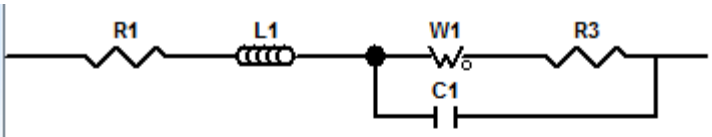

Element	Freedom	Value	Error	Error%
R1	± Free(±)	0.00032667	1.8627E-5	5.7021
L1	± Free(±)	1.2409E-7	3.4312E-9	2.7651
W1-R	± Free(±)	0.021043	0.065498	311.26
W1-T	± Free(±)	27156	1.6841E5	620.16
W1-P	X Fixed	0.5	N/A	N/A
R3	± Free(±)	0.00015235	2.0306E-5	13.329
C1	± Free(±)	15.72	5.4357	34.578

Figure 46: Model and fitting parameters for cell A at 4.08V

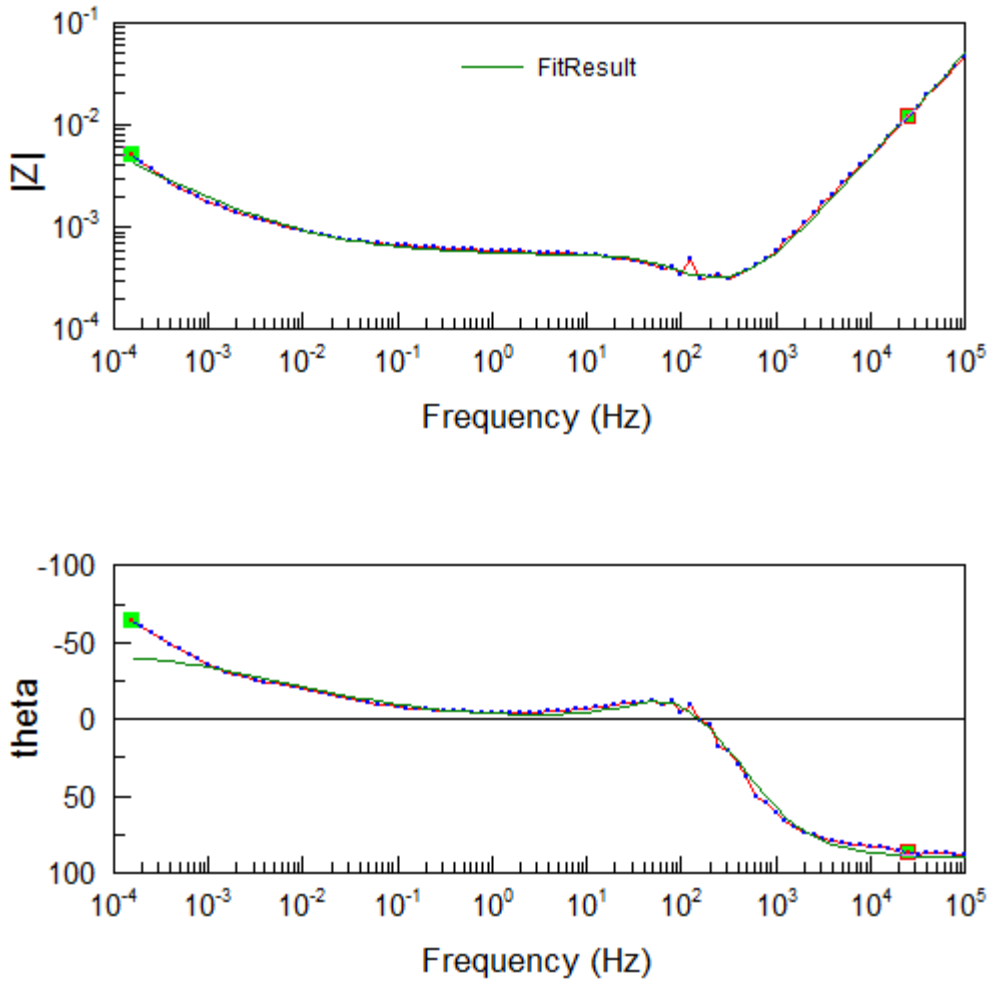

Figure 47: Bode plot of cell A at 3.84V

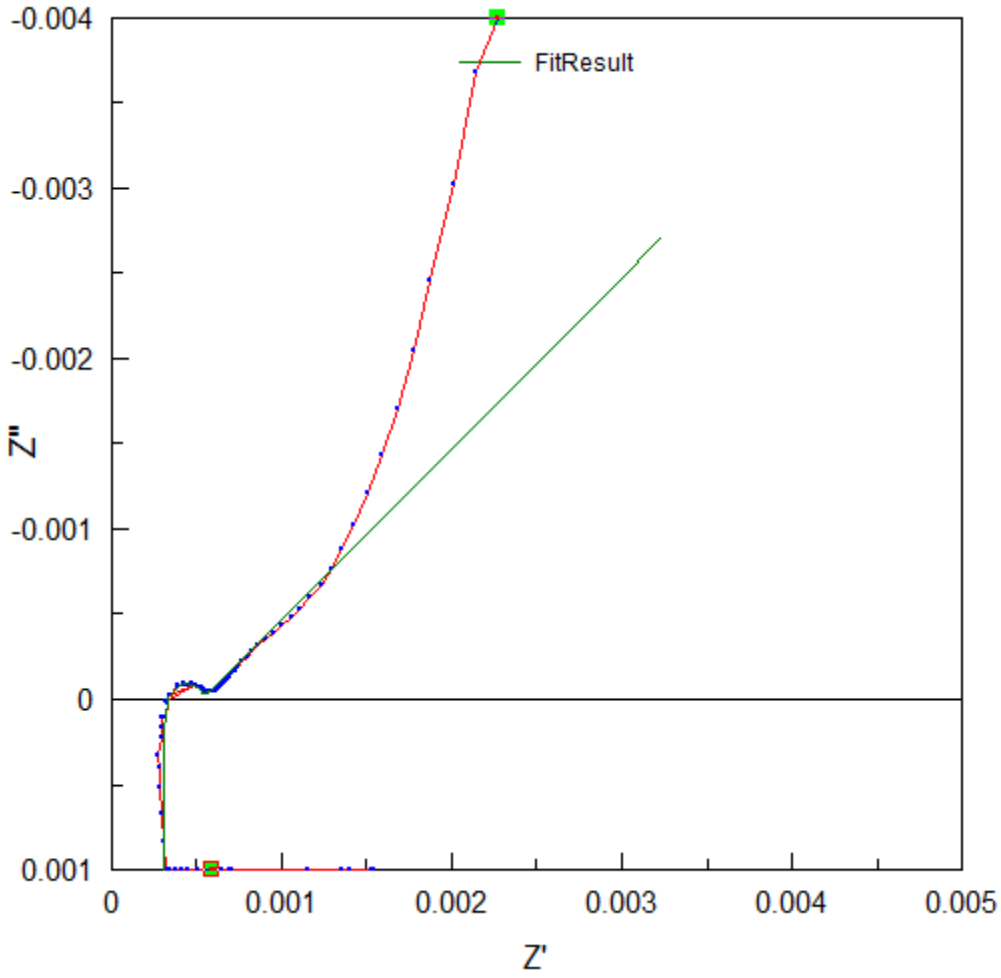

Figure 48: Nyquist plot of cell A at 3.84V

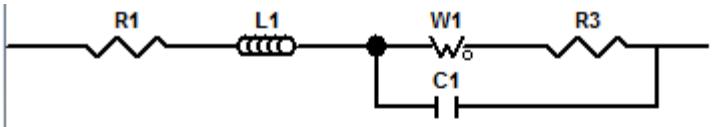

Element	Freedom	Value	Error	Error%
R1	± Free(±)	0.0003074	9.4078E-6	3.0604
L1	± Free(±)	7.8609E-8	1.3607E-9	1.731
W1-R	± Free(±)	0.020013	N/A	N/A
W1-T	± Free(±)	27114	1312.3	4.8399
W1-P	X Fixed	0.5	N/A	N/A
R3	± Free(±)	0.00022485	1.147E-5	5.1012
C1	± Free(±)	11.61	1.5396	13.261

Figure 49: Model and fitting parameters of cell A at 3.84V

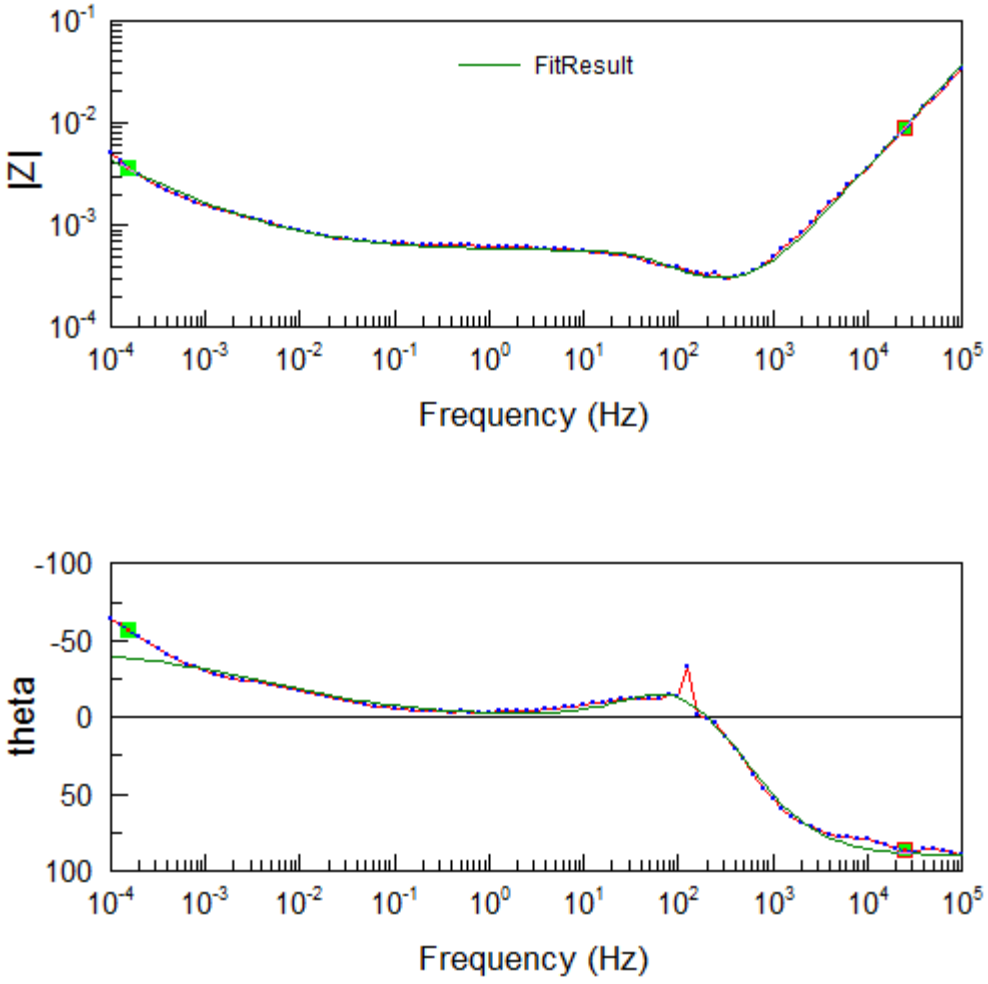

Figure 50: Bode plot of cell A at 3.69V

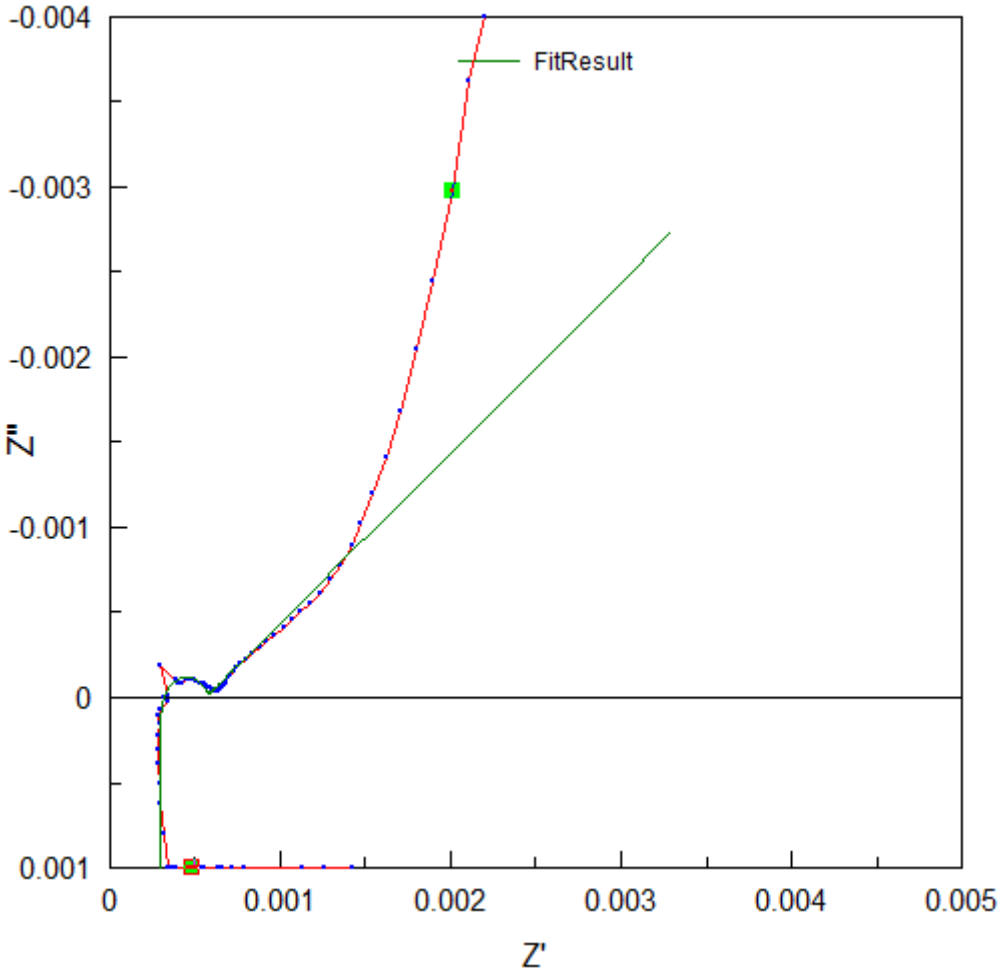

Figure 51: Nyquist plot of cell A at 3.69V

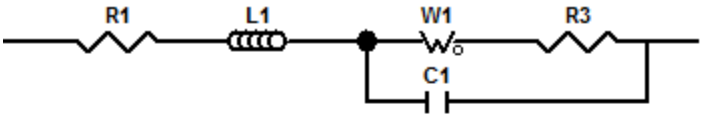

Element	Freedom	Value	Error	Error%
R1	± Free(±)	0.00029446	8.2231E-6	2.7926
L1	± Free(±)	5.8478E-8	1.0145E-9	1.7348
W1-R	X Fixed	0.081722	N/A	N/A
W1-T	± Free(±)	711280	34270	4.8181
W1-P	X Fixed	0.5	N/A	N/A
R3	± Free(±)	0.00027027	1.0801E-5	3.9964
C1	± Free(±)	10.09	1.0436	10.343

Figure 52: Model and fitting parameters of cell A at 3.69V

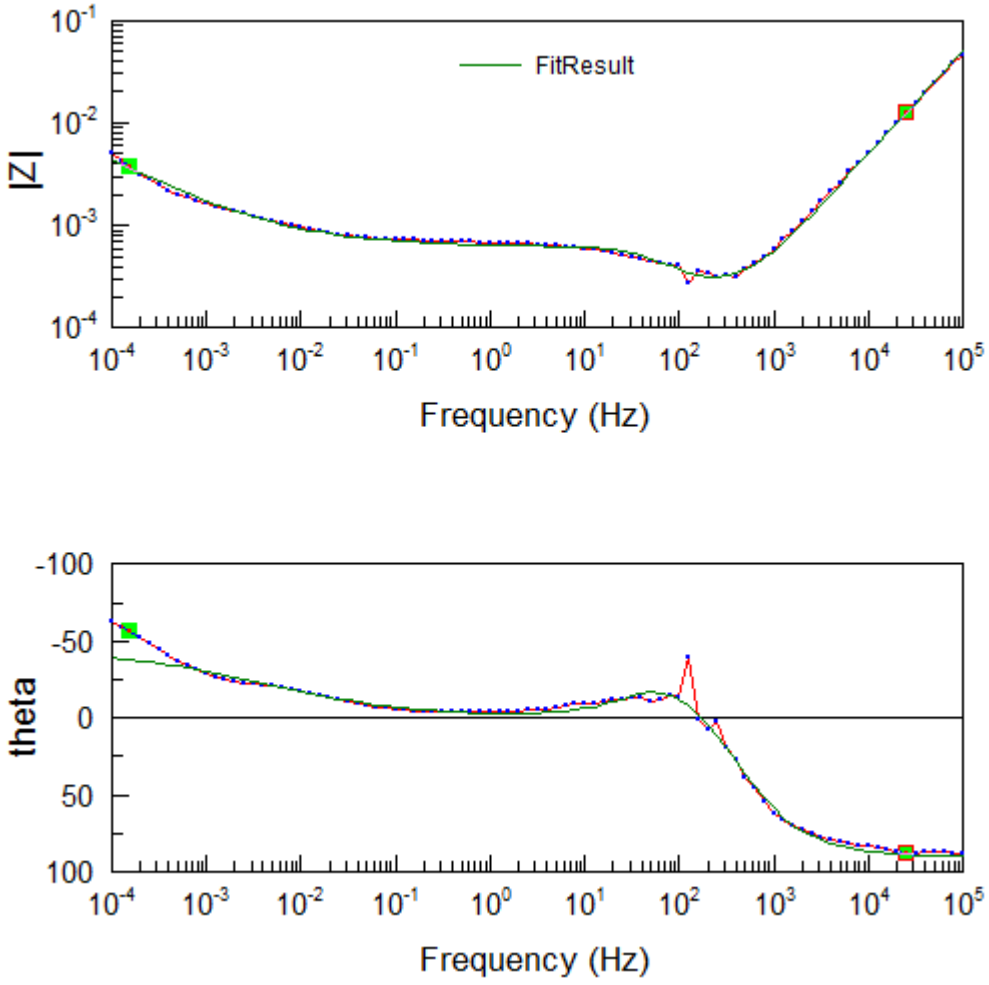

Figure 53: Bode plot of cell A at 3.62V

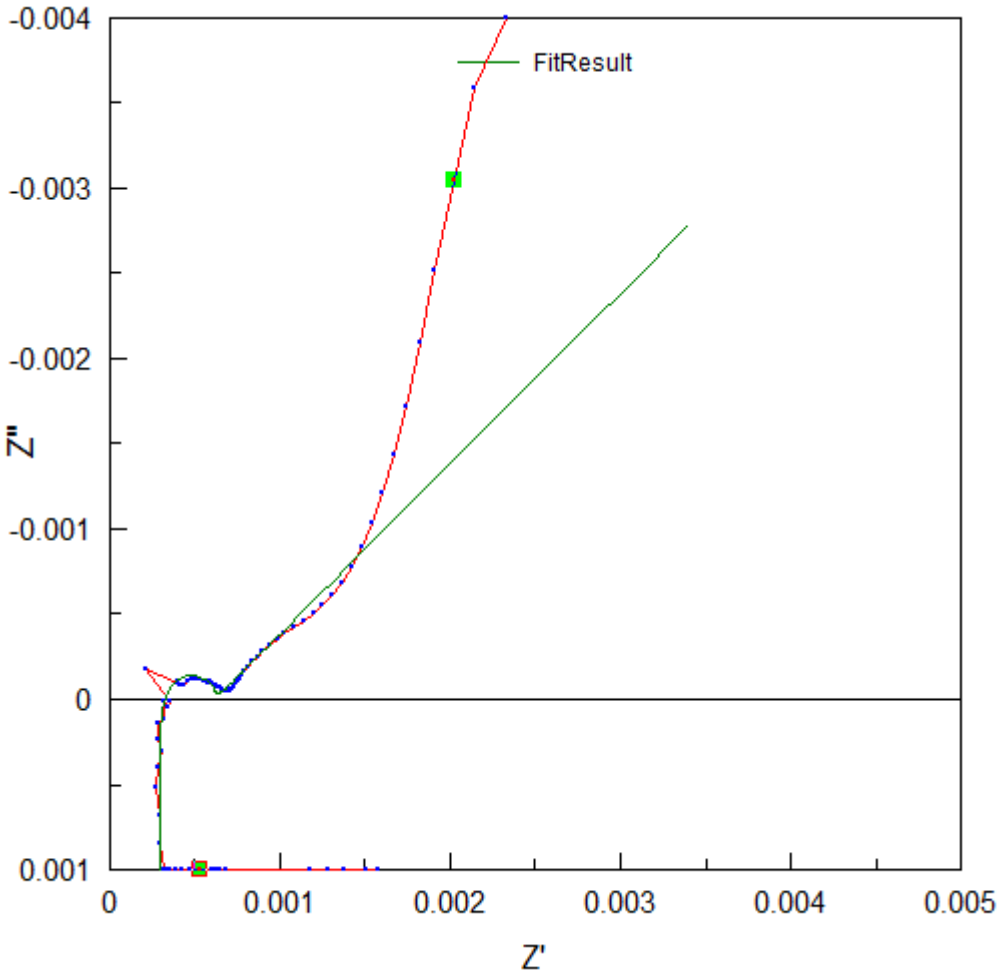

Figure 54: Nyquist plot of cell A at 3.62V

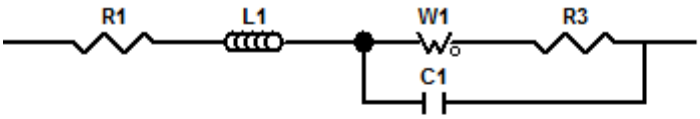

Element	Freedom	Value	Error	Error%
R1	± Free(±)	0.00029716	9.0821E-6	3.0563
L1	± Free(±)	7.9807E-8	1.3914E-9	1.7435
W1-R	± Free(±)	0.081674	35068	4.2937E7
W1-T	± Free(±)	687200	5.9012E11	8.5873E7
W1-P	X Fixed	0.5	N/A	N/A
R3	± Free(±)	0.00031929	1.2082E-5	3.784
C1	± Free(±)	9.857	0.96168	9.7563

Figure 55: Model and fitting parameters of cell A at 3.62V

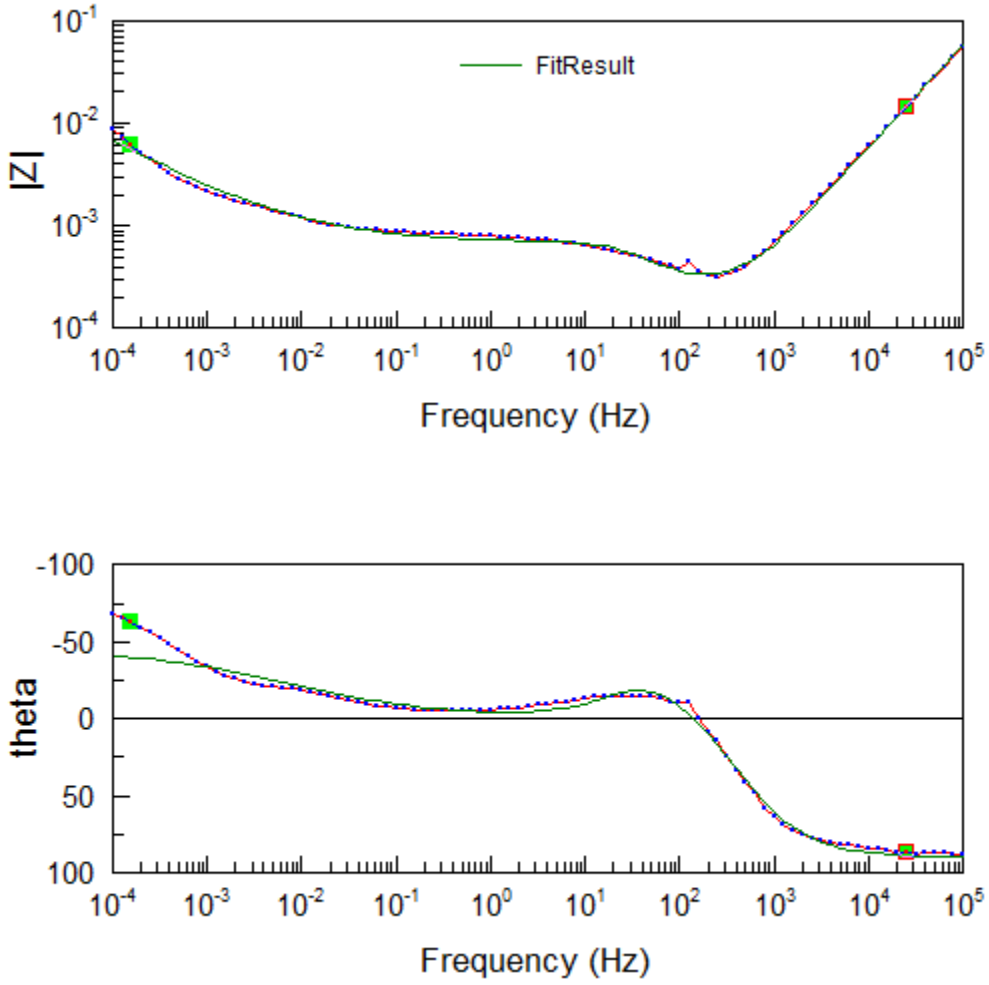

Figure 56: Bode plot of cell A at 3.52V

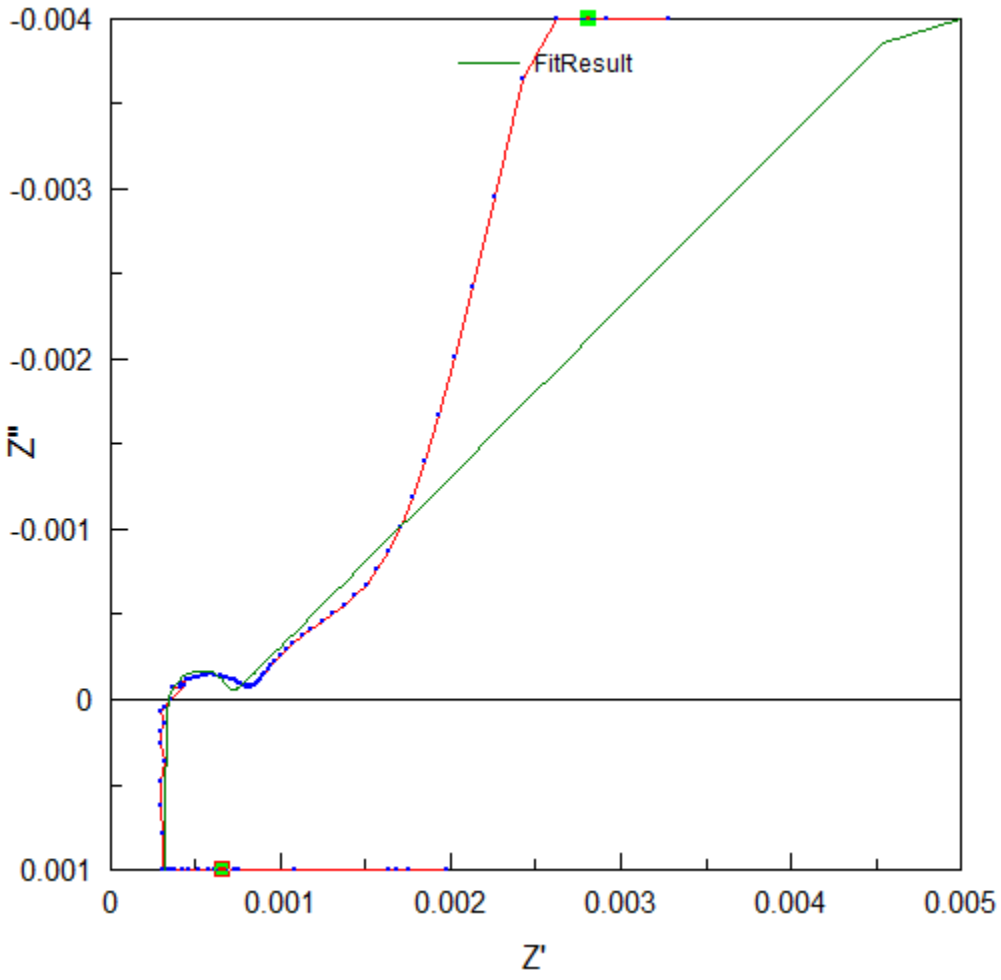

Figure 57: Nyquist plot of cell A at 3.52V

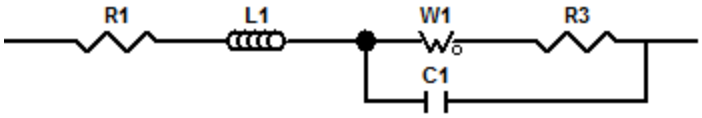

Element	Freedom	Value	Error	Error%
R1	± Free(±)	0.00032469	1.1138E-5	3.4303
L1	± Free(±)	9.2372E-8	1.9319E-9	2.0914
W1-R	± Free(±)	0.082392	22288	2.7051E7
W1-T	± Free(±)	279420	1.5118E11	5.4105E7
W1-P	× Fixed	0.5	N/A	N/A
R3	± Free(±)	0.00036458	1.6287E-5	4.4673
C1	± Free(±)	13.52	1.5313	11.326

Figure 58: Model and fitting parameters of cell A at 3.52V

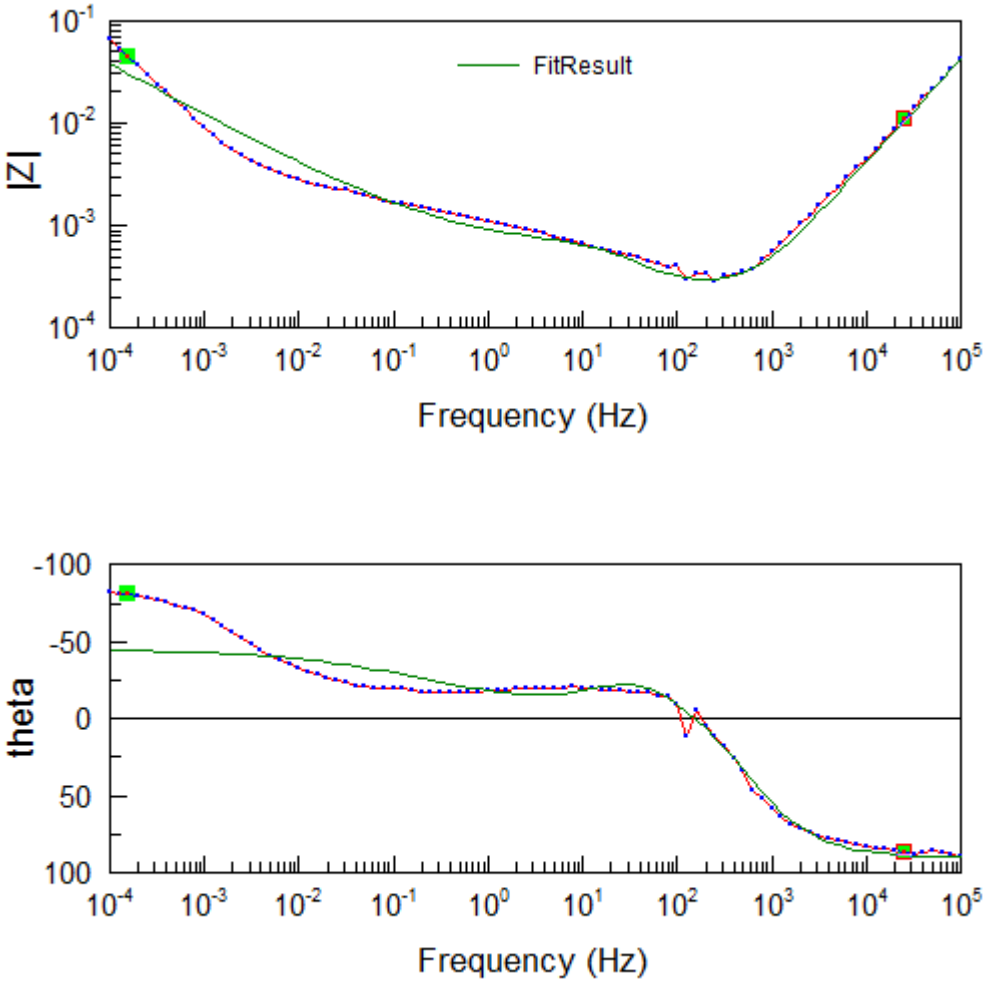

Figure 59: Bode plot of cell A at 3.05V

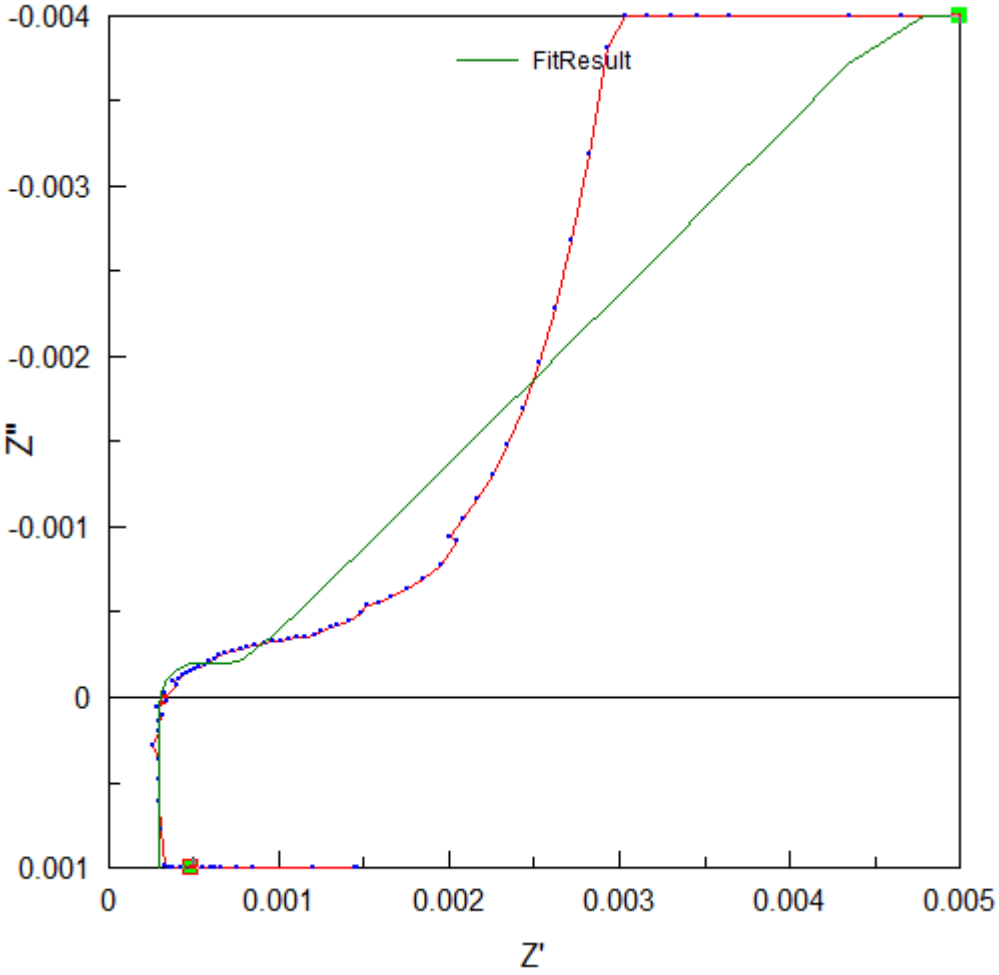

Figure 60: Nyquist plot of cell A at 3.05V

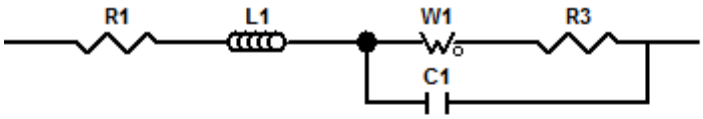

Element	Freedom	Value	Error	Error%
R1	± Free(±)	0.00029429	2.0328E-5	6.9075
L1	± Free(±)	6.6473E-8	3.0455E-9	4.5816
W1-R	± Free(±)	0.4927	2.3435E5	4.7564E7
W1-T	± Free(±)	280710	2.6703E11	9.5127E7
W1-P	× Fixed	0.5	N/A	N/A
R3	± Free(±)	0.00035417	4.4381E-5	12.531
C1	± Free(±)	15.77	3.4198	21.685

Figure 61: Model and fitting parameters of cell A at 3.05V

B.2 Complex frequency domain model fitting results

B.1 includes the fitting result for the model introduced in section 4.2.

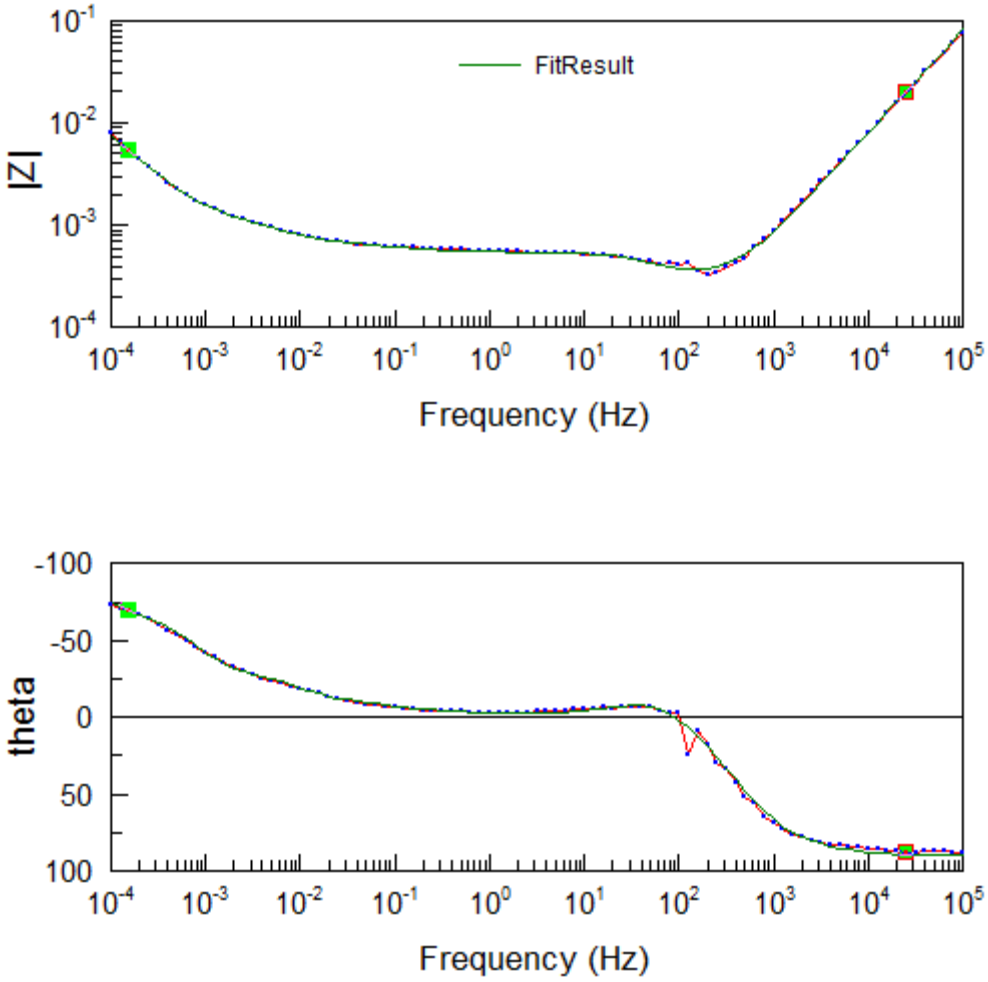

Figure 62: Bode plot of cell A at 4.08V using multiple time constants model

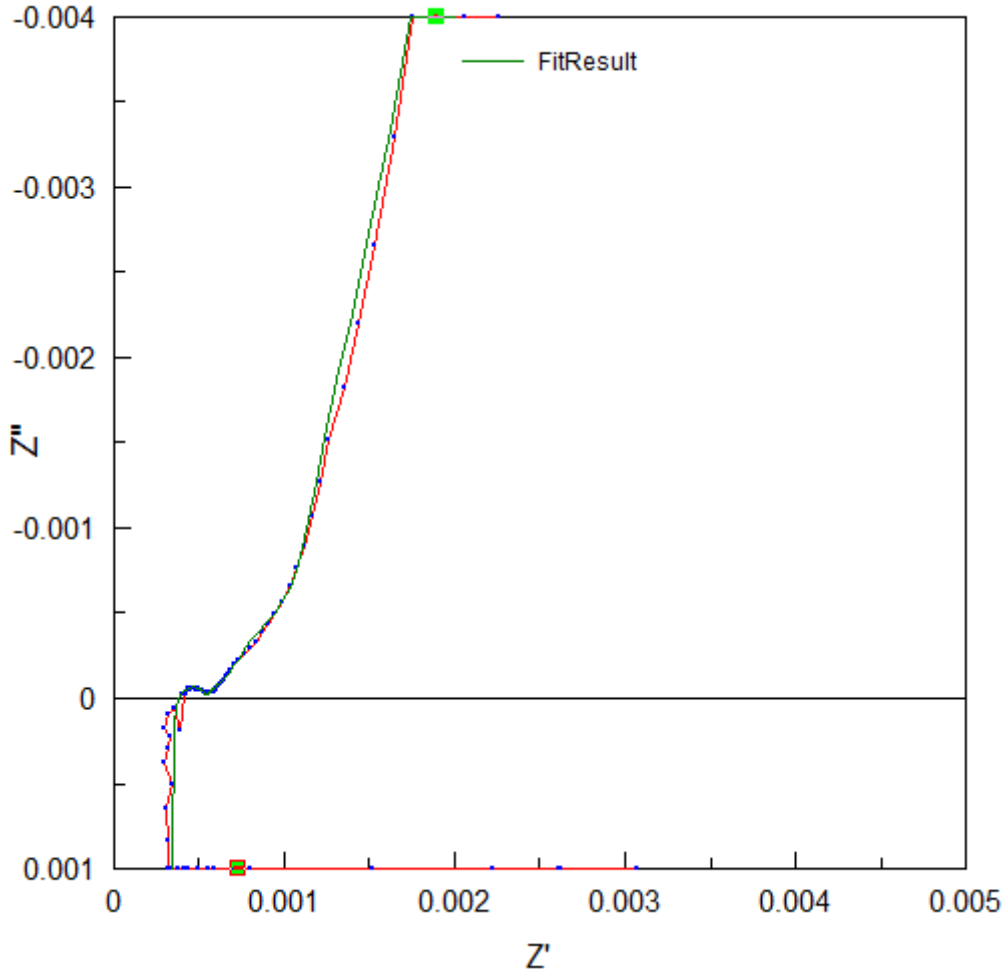

Figure 63: Nyquist plot of cell A at 4.08V using multiple time constants model

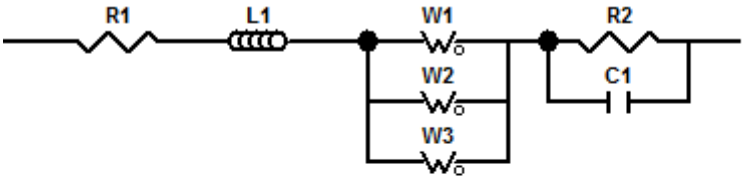

Element	Freedom	Value	Error	Error%
R1	± Free(±)	0.00034768	5.5034E-6	1.5829
L1	± Free(±)	1.2782E-7	1.1055E-9	0.86489
W1-R	± Free(±)	0.024386	0.0070503	28.911
W1-T	± Free(±)	2309	562.6	24.366
W1-P	X Fixed	0.5	N/A	N/A
W2-R	± Free(±)	0.0026848	0.00027646	10.297
W2-T	± Free(±)	318	41.246	12.97
W2-P	X Fixed	0.5	N/A	N/A
W3-R	± Free(±)	0.001839	0.00050558	27.492
W3-T	± Free(±)	28.03	11.767	41.98
W3-P	X Fixed	0.5	N/A	N/A
R2	± Free(±)	0.00018132	6.718E-6	3.7051
C1	± Free(±)	20.42	1.9062	9.335

Figure 64: Fitting parameters of cell A at 4.08V using multiple time constants model

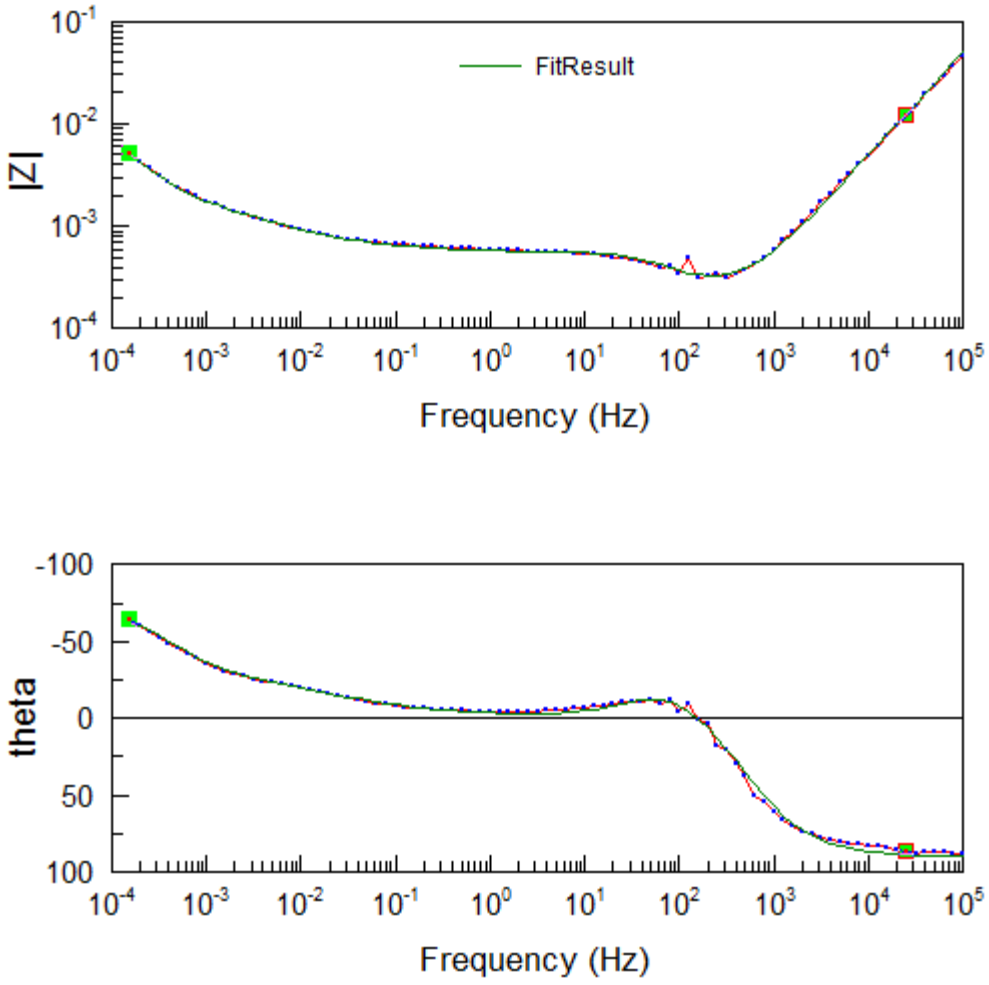

Figure 65: Bode plot of cell A at 3.84V using multiple time constants model

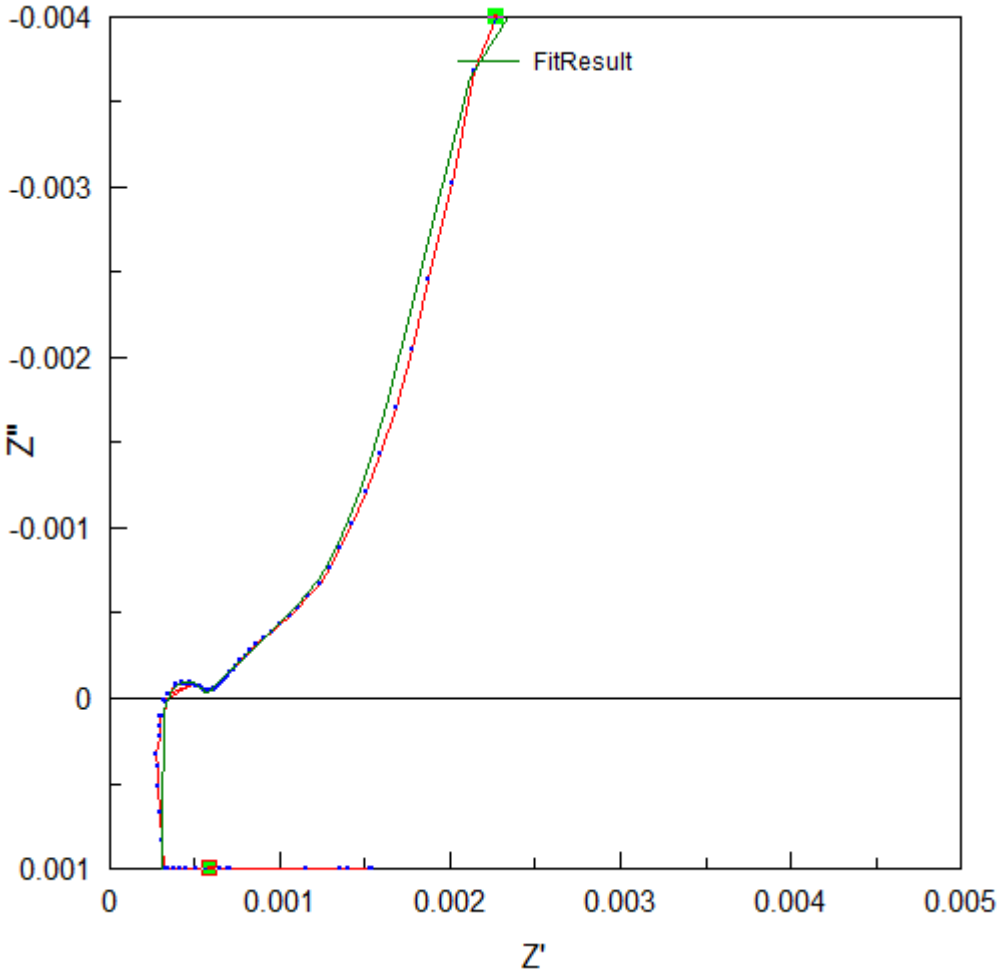

Figure 66: Nyquist plot of cell A at 3.84V using multiple time constants model

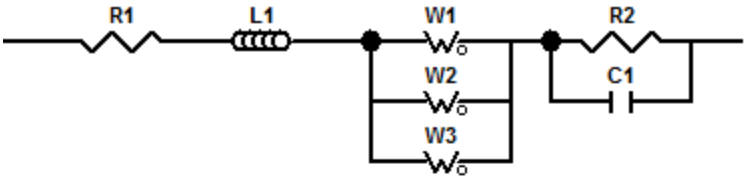

Element	Freedom	Value	Error	Error%
R1	± Free(±)	0.00031237	5.67E-6	1.8152
L1	± Free(±)	7.9208E-8	8.3381E-10	1.0527
W1-R	± Free(±)	0.05931	0.29054	489.87
W1-T	± Free(±)	16810	1.8019E5	1071.9
W1-P	X Fixed	0.5	N/A	N/A
W2-R	+ Free(+)	0.0055756	0.0051385	92.16
W2-T	± Free(±)	282.2	200.31	70.982
W2-P	X Fixed	0.5	N/A	N/A
W3-R	+ Free(+)	0.0078872	0.0095367	120.91
W3-T	± Free(±)	814.1	692.71	85.089
W3-P	X Fixed	0.5	N/A	N/A
R2	± Free(±)	0.0002345	7.209E-6	3.0742
C1	± Free(±)	12.78	1.0179	7.9648

Figure 67: Fitting parameters of cell A at 3.84V using multiple time constants model

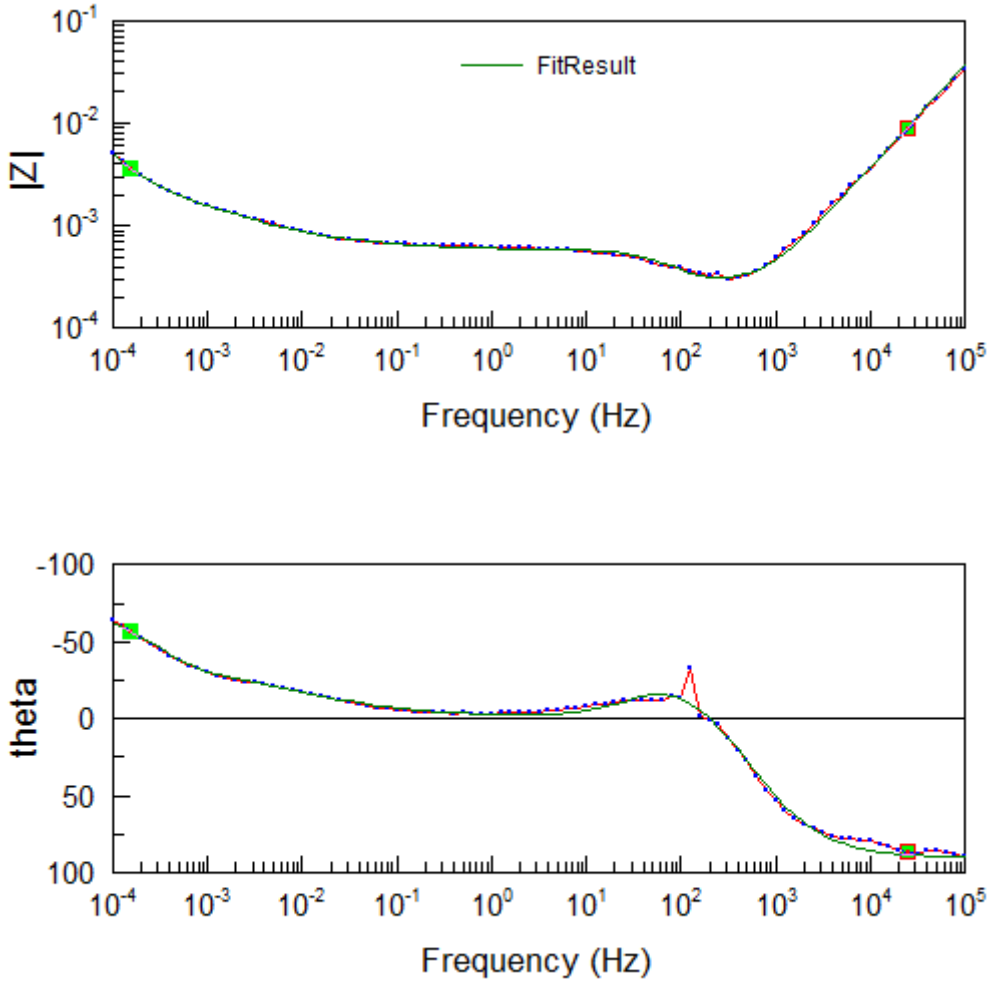

Figure 68: Bode plot of cell A at 3.69V using multiple time constants model

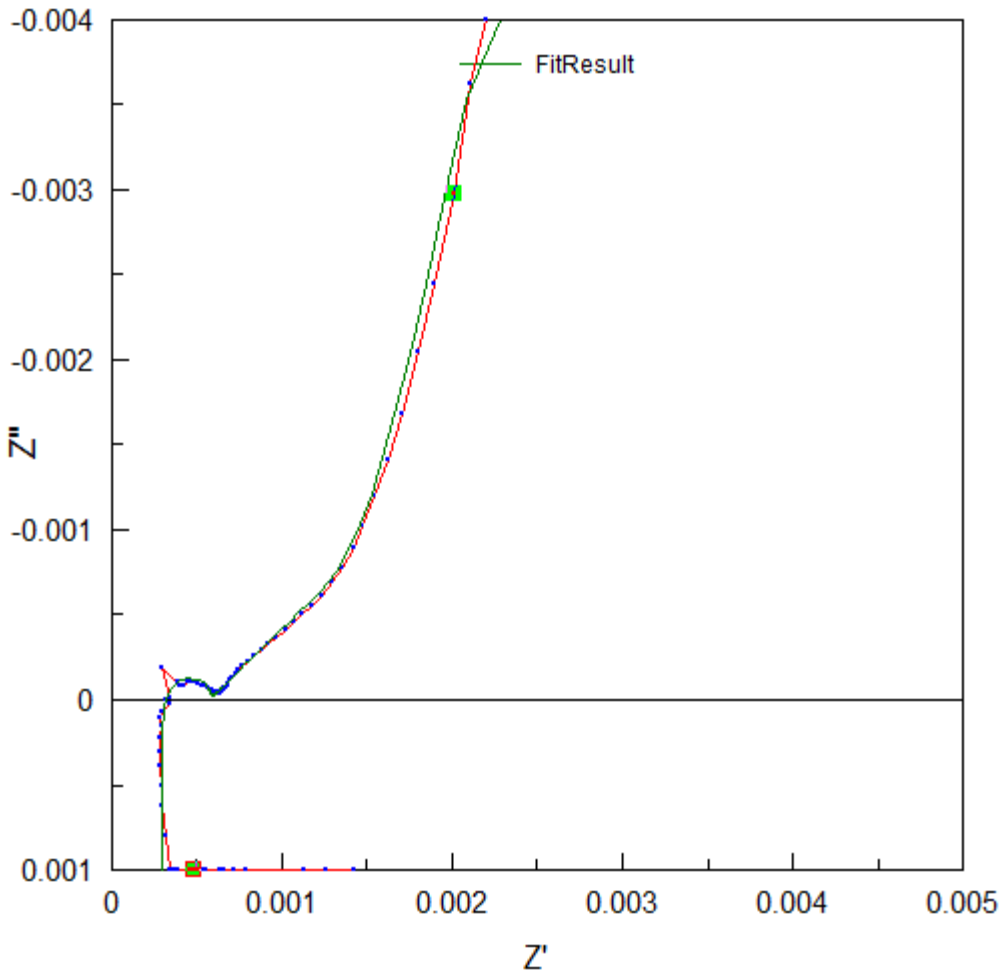

Figure 69: Nyquist plot of cell A at 3.69V using multiple time constants model

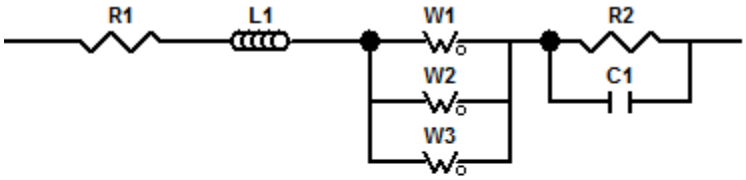

Element	Freedom	Value	Error	Error%
R1	± Free(±)	0.00029726	5.2463E-6	1.7649
L1	± Free(±)	5.8916E-8	6.5114E-10	1.1052
W1-R	± Free(±)	0.080109	0.79611	993.78
W1-T	± Free(±)	30483	6.5958E5	2163.8
W1-P	X Fixed	0.5	N/A	N/A
W2-R	± Free(±)	0.011656	0.02388	204.87
W2-T	± Free(±)	1690	2533.3	149.9
W2-P	X Fixed	0.5	N/A	N/A
W3-R	± Free(±)	0.0048723	0.0047118	96.706
W3-T	± Free(±)	621.7	394.78	63.5
W3-P	X Fixed	0.5	N/A	N/A
R2	± Free(±)	0.00027967	7.1049E-6	2.5405
C1	± Free(±)	10.51	0.68527	6.5202

Figure 70: Fitting parameters of cell A at 3.69V using multiple time constants model

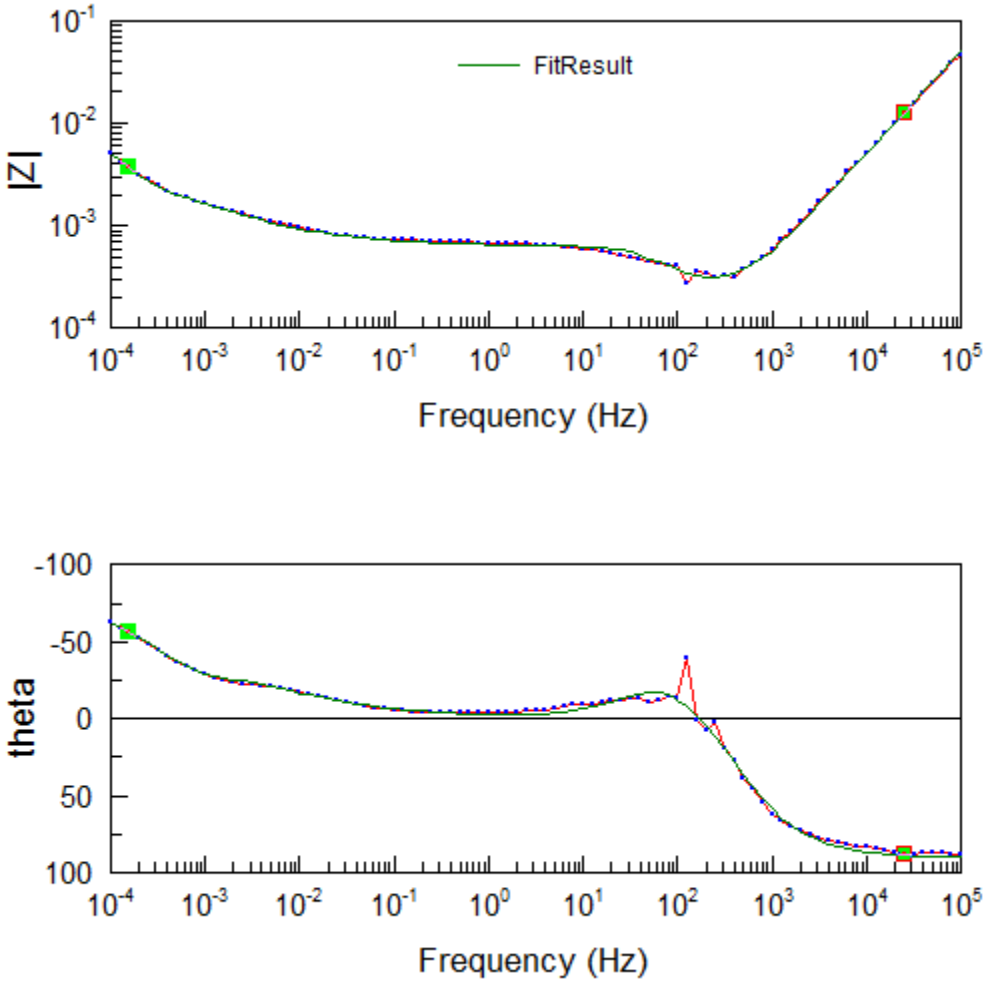

Figure 71: Bode plot of cell A at 3.62V using multiple time constants model

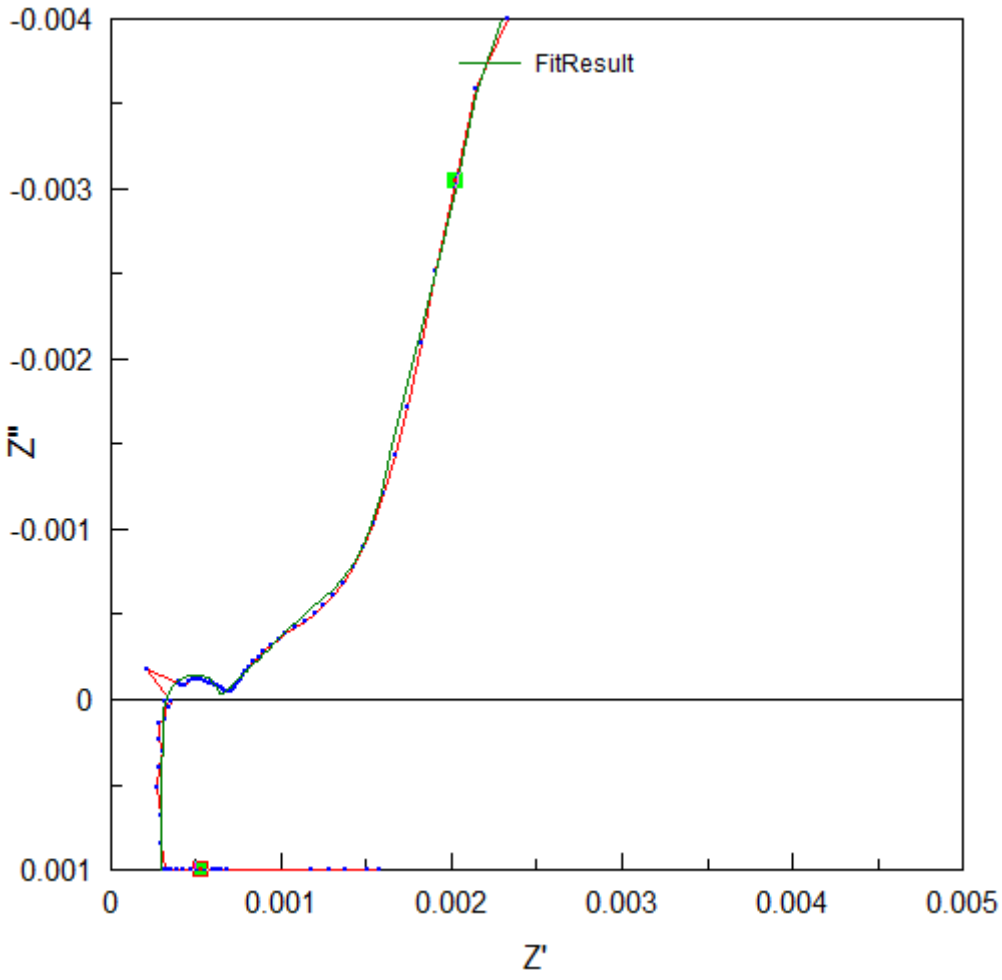

Figure 72: Nyquist plot of cell A at 3.62V using multiple time constants model

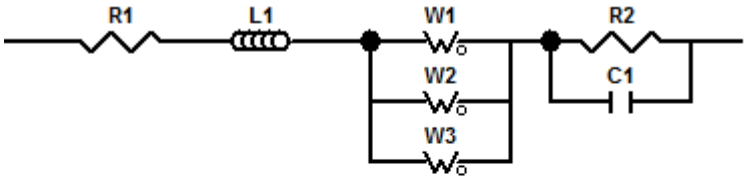

Element	Freedom	Value	Error	Error%
R1	± Free(±)	0.00030009	6.2354E-6	2.0778
L1	± Free(±)	8.0373E-8	9.593E-10	1.1936
W1-R	± Free(±)	0.040933	2.03	4959.3
W1-T	± Free(±)	5818	97117	1669.3
W1-P	X Fixed	0.5	N/A	N/A
W2-R	± Free(±)	0.035861	1.2522	3491.8
W2-T	± Free(±)	2881	66846	2320.2
W2-P	X Fixed	0.5	N/A	N/A
W3-R	± Free(±)	0.0038968	0.0033284	85.414
W3-T	± Free(±)	787.3	471.5	59.888
W3-P	X Fixed	0.5	N/A	N/A
R2	± Free(±)	0.00032904	8.5424E-6	2.5962
C1	± Free(±)	10.26	0.68142	6.6415

Figure 73: Fitting parameters of cell A at 3.62V using multiple time constants model

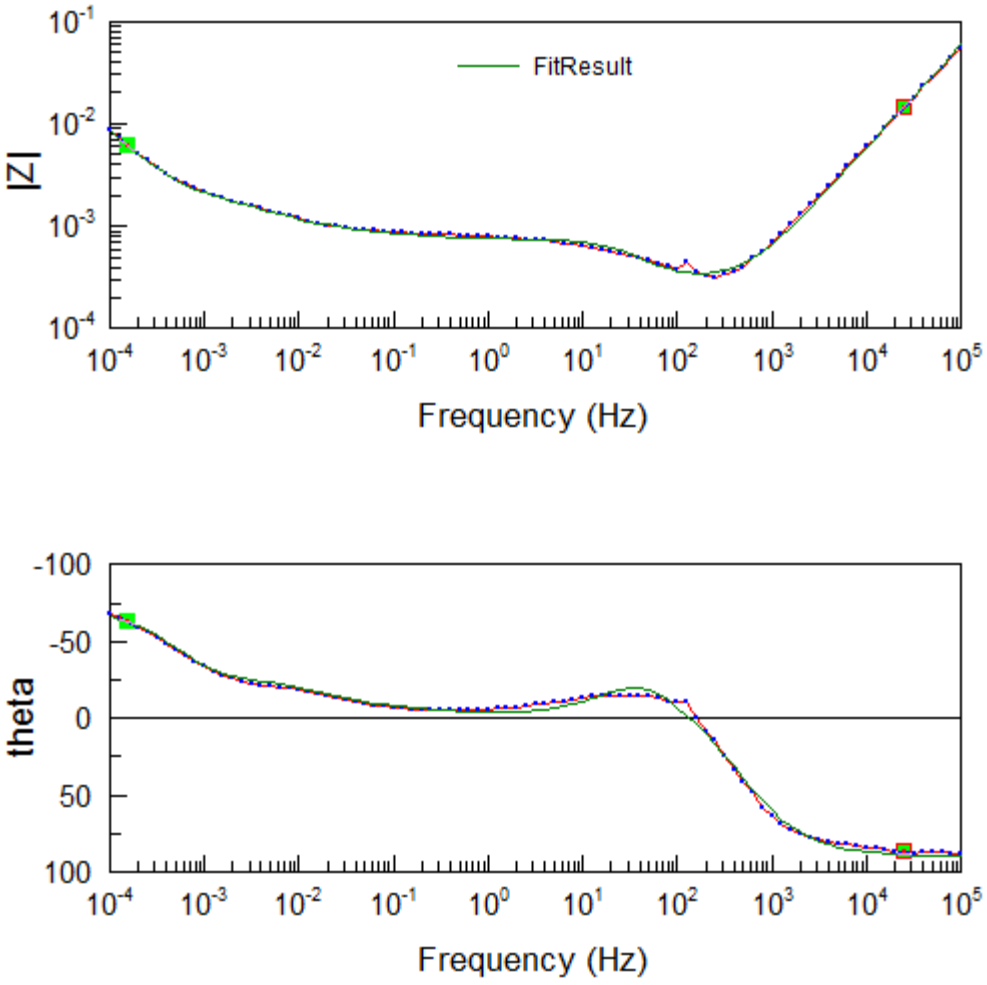

Figure 74: Bode plot of cell A at 3.52V using multiple time constants model

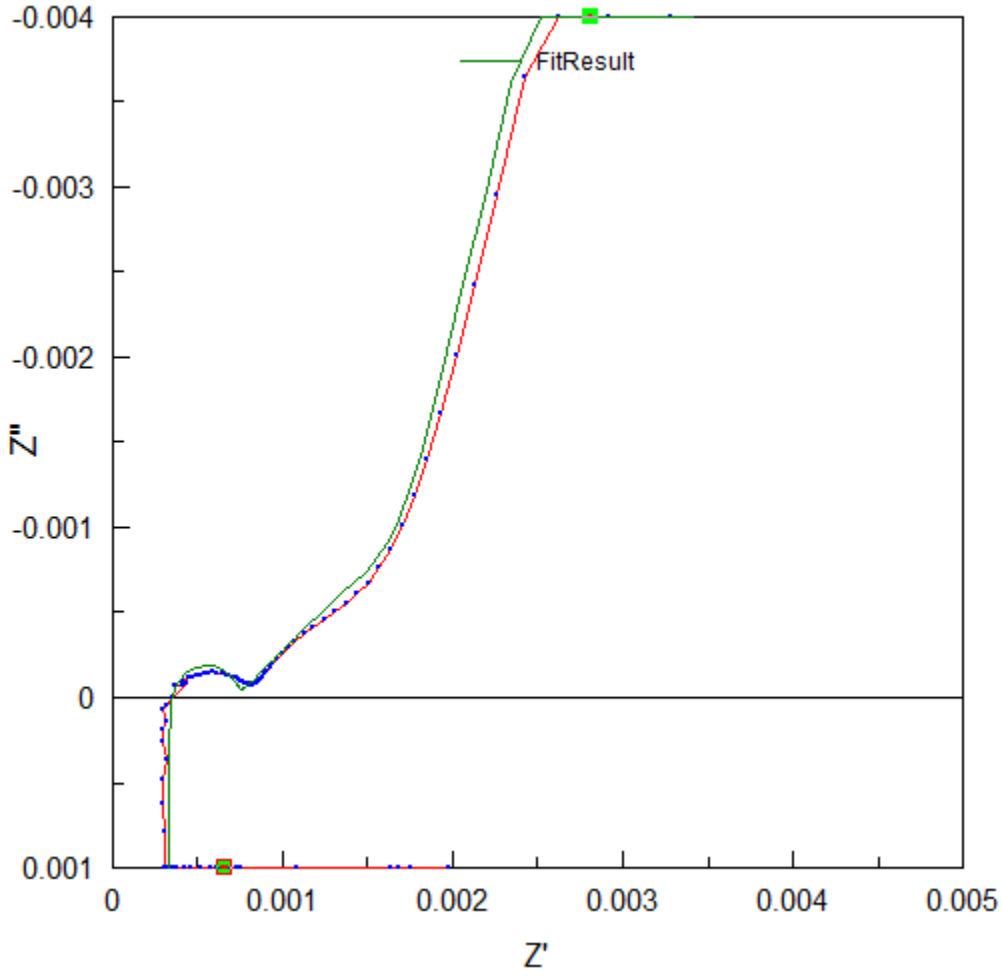

Figure 75: Nyquist plot of cell A at 3.52V using multiple time constants model

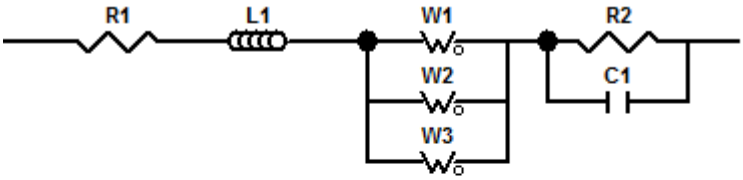

Element	Freedom	Value	Error	Error%
R1	± Free(±)	0.00033334	5.4947E-6	1.6484
L1	± Free(±)	9.3692E-8	9.6661E-10	1.0317
W1-R	± Free(±)	0.031436	0.05675	180.53
W1-T	± Free(±)	1500	2200.3	146.69
W1-P	X Fixed	0.5	N/A	N/A
W2-R	± Free(±)	0.12866	0.95467	742.01
W2-T	± Free(±)	31342	4.8823E5	1557.7
W2-P	X Fixed	0.5	N/A	N/A
W3-R	± Free(±)	0.004517	0.001254	27.762
W3-T	± Free(±)	448.6	125.48	27.971
W3-P	X Fixed	0.5	N/A	N/A
R2	± Free(±)	0.00039006	8.5404E-6	2.1895
C1	± Free(±)	15.06	0.82481	5.4768

Figure 76: Fitting parameters of cell A at 3.52V using multiple time constants model

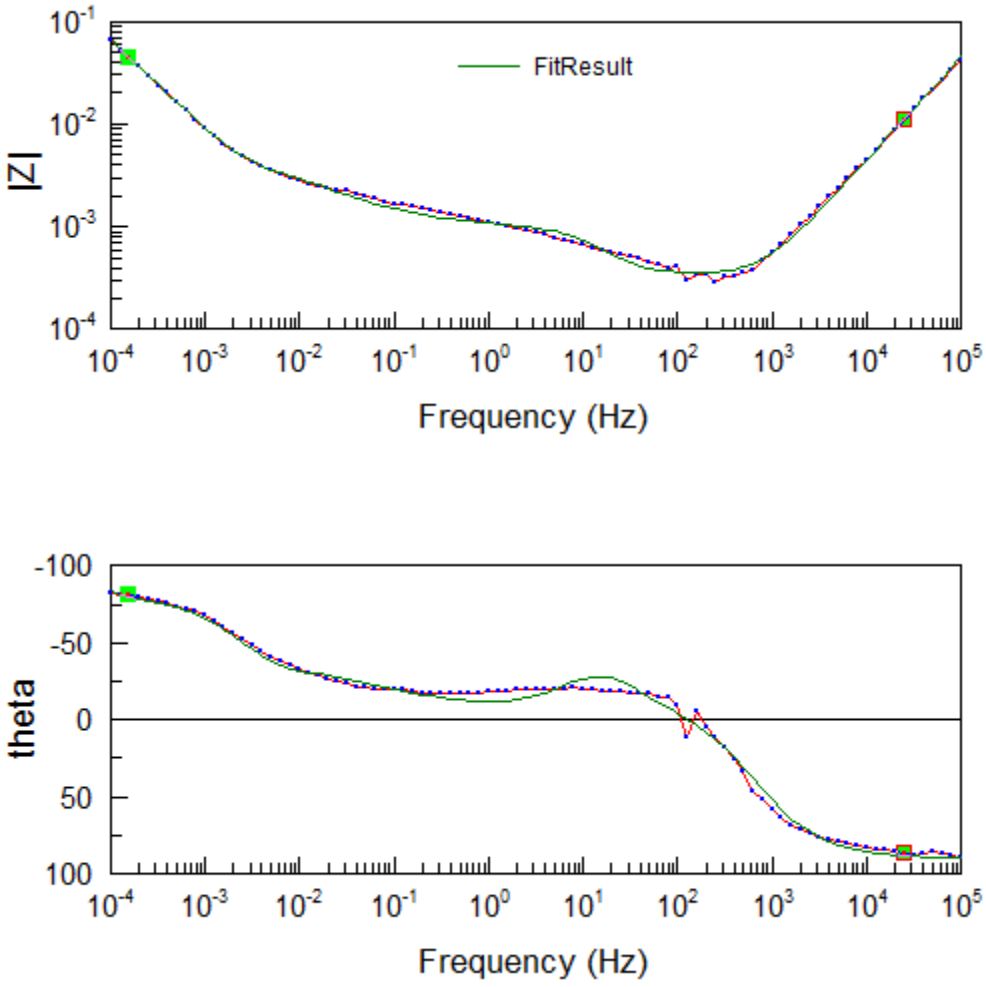

Figure 77: Bode plot of cell A at 3.05V using multiple time constants model

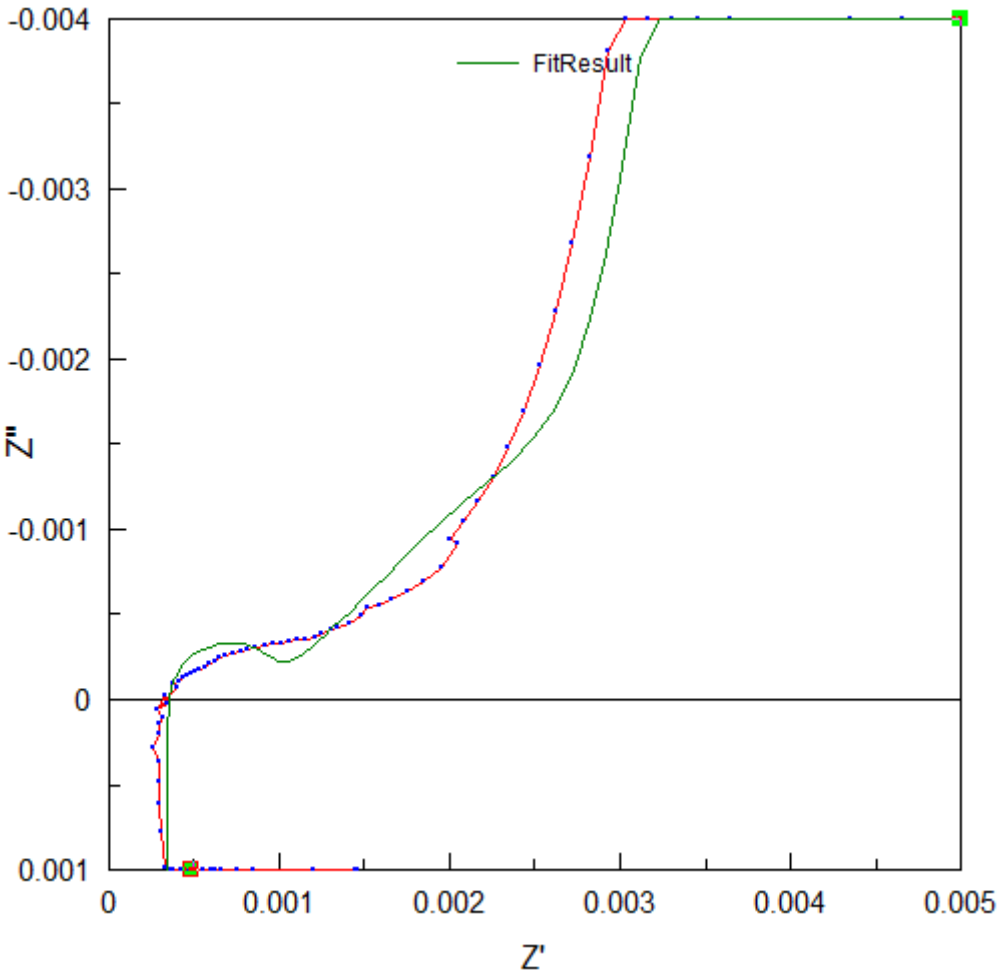

Figure 78: Nyquist plot of cell A at 3.05V using multiple time constants model

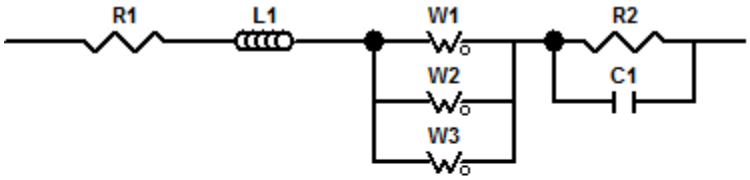

Element	Freedom	Value	Error	Error%
R1	± Free(±)	0.00033845	7.3951E-6	2.185
L1	± Free(±)	7.1671E-8	1.1714E-9	1.6344
W1-R	± Free(±)	0.0075511	0.0026298	34.827
W1-T	± Free(±)	99.77	33.797	33.875
W1-P	X Fixed	0.5	N/A	N/A
W2-R	± Free(±)	0.25147	0.35546	141.35
W2-T	± Free(±)	1677	1432	85.391
W2-P	X Fixed	0.5	N/A	N/A
W3-R	± Free(±)	0.073534	0.25036	340.47
W3-T	± Free(±)	314	716.17	228.08
W3-P	X Fixed	0.5	N/A	N/A
R2	± Free(±)	0.0005643	2.1111E-5	3.7411
C1	± Free(±)	30.12	2.0406	6.7749

Figure 79: Fitting parameters of cell A at 3.05V using multiple time constants model

	C_1(error%) (F)	C_2(error%) (F)	C_3(error%) (F)
4.08V	95000(37.87)	120000(16.56)	15000(50.18)
3.84V	280000(1178.53)	51000(116.33)	100000(147.85)
3.69V	380000(253.85)	140000(253.85)	130000(115.69)
3.62V	140000(5232.71)	80000(4192.37)	200000(104.32)
3.52V	48000(232.61)	240000(1725.40)	99000(39.44)
3.05V	13000(48.58)	6700(165.14)	4300(409.81)

Table 5: Estimated capacitance from the parallel Warburg elements used in multiple time constants model

The C values are found using C=T/R from the Warburg elements. Their uncertainties are found by taking the square root of the sum of the squares of the percentage uncertainties in T and R, respectively.

Voltage	Total capacitance(F)	Capacitance uncertainty magnitude(F)
4.08V	230000	42000
3.84V	440000	3300000
3.69V	650000	9100000
3.62V	420000	8200000
3.52V	390000	4200000
3.05V	24000	22000

Table 6: Total capacitance extracted from the parallel Warburg elements in the multiple time constants model

The total capacitance is found by summing up C_1, C_2 and C_3. The uncertainty of the total capacitance is calculated by taking the square root of the sum of square of the magnitude of errors for C_1, C_2 and C_3. The huge uncertainty in capacitance is expected when the total capacitance is high and the time constant is long.

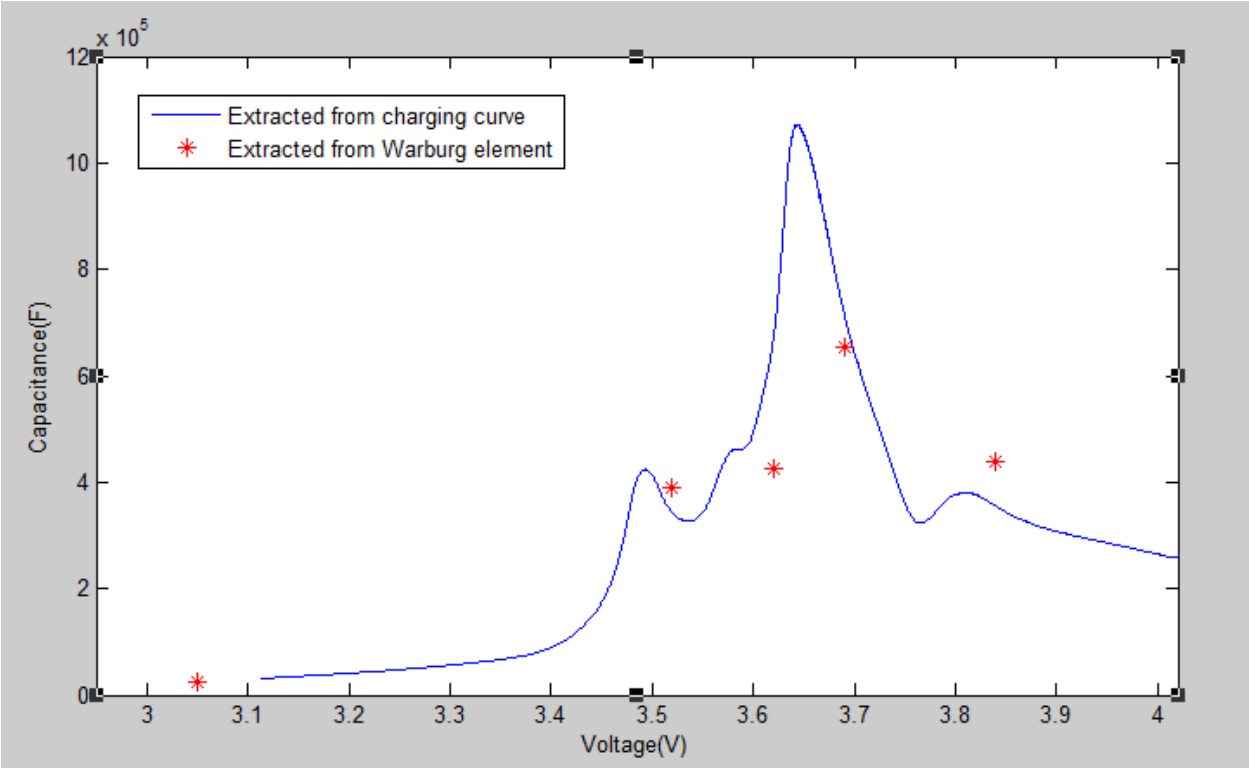

Figure 80: Comparison between capacitance extracted from charging curve and Warburg elements

Appendix C : Simulink model

This section covers the Simulink blocks used in the model introduced in section 4.3. In between data points in the look-up tables, linear interpolation is chosen as the default method to use by Matlab's 1-D lookup table function block. The gap between two known data points is represented by a straight line. The values for the lookup tables are included in Appendix D.

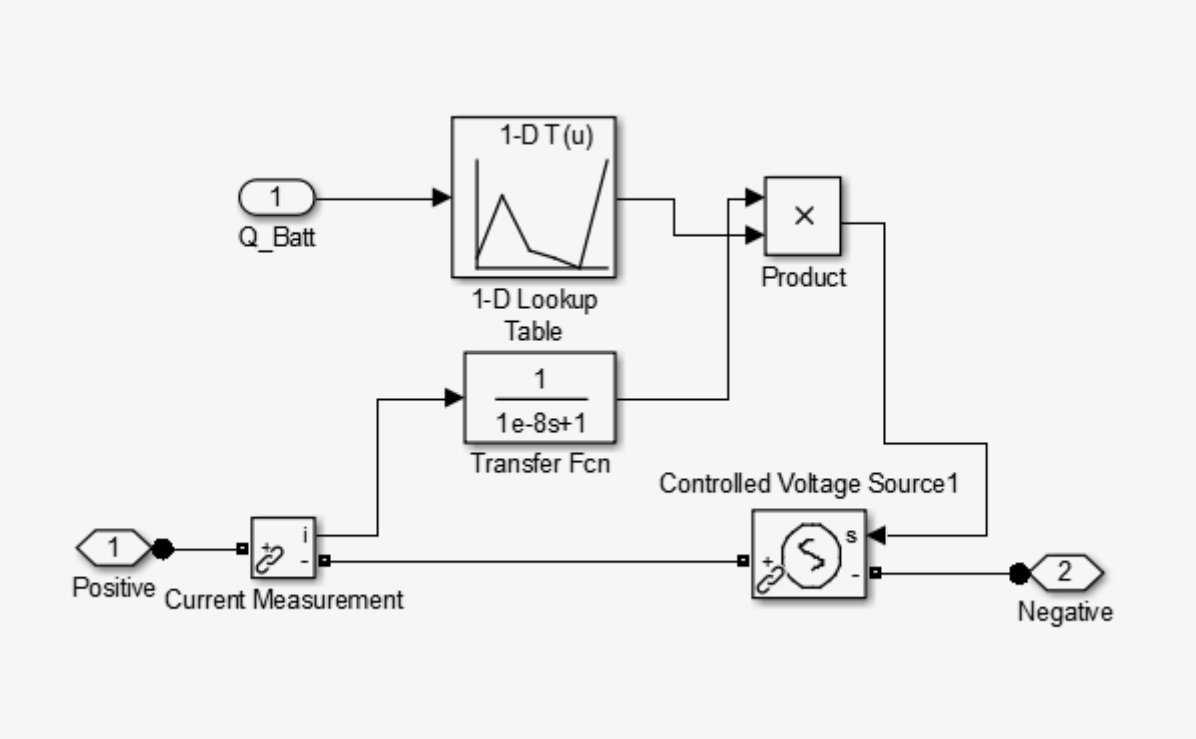

Figure 81: ESR

Figure 81 is the ESR block. 'Q_Batt' is the input terminal for reading in number of charges. This value is fed into the 1-D lookup table, which outputs a numerical value to the 'Product' function. 'Positive' is an input terminal which carries the current. The current is measured by the 'Current Measurement' block and the reading is fed to the 'Transfer Fcn' block, which is a transfer function used to create a short delay. The '-' output of the 'Current Measurement' block is the

current, where the ‘i’ terminal outputs a numerical value of the current measurement. The short delay introduced by the transfer function is to prevent numerical loop from happening while solving the system in Simulink. The lookup table provides a resistance value based on the charge input. This resistance is then multiplied with the current measurement, which gives the numerical value of the voltage drop, caused by the ESR resistor. This value is passed on to ‘Controller voltage source’ block to set the voltage output.

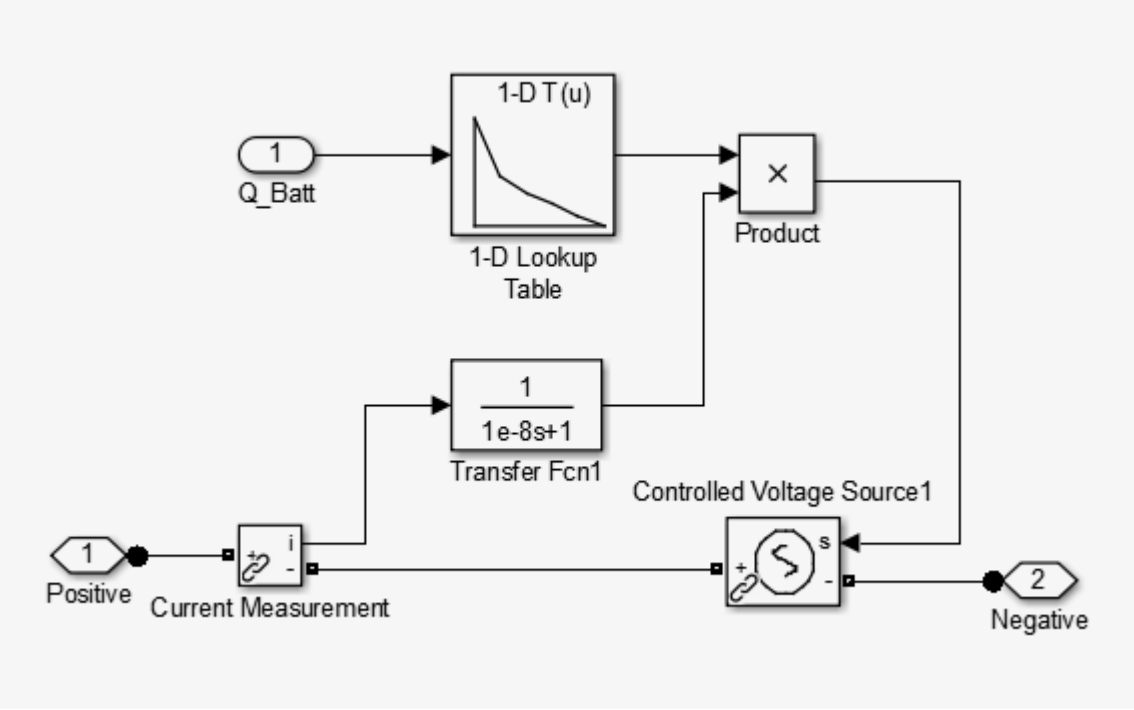

Figure 82: R_{ct}

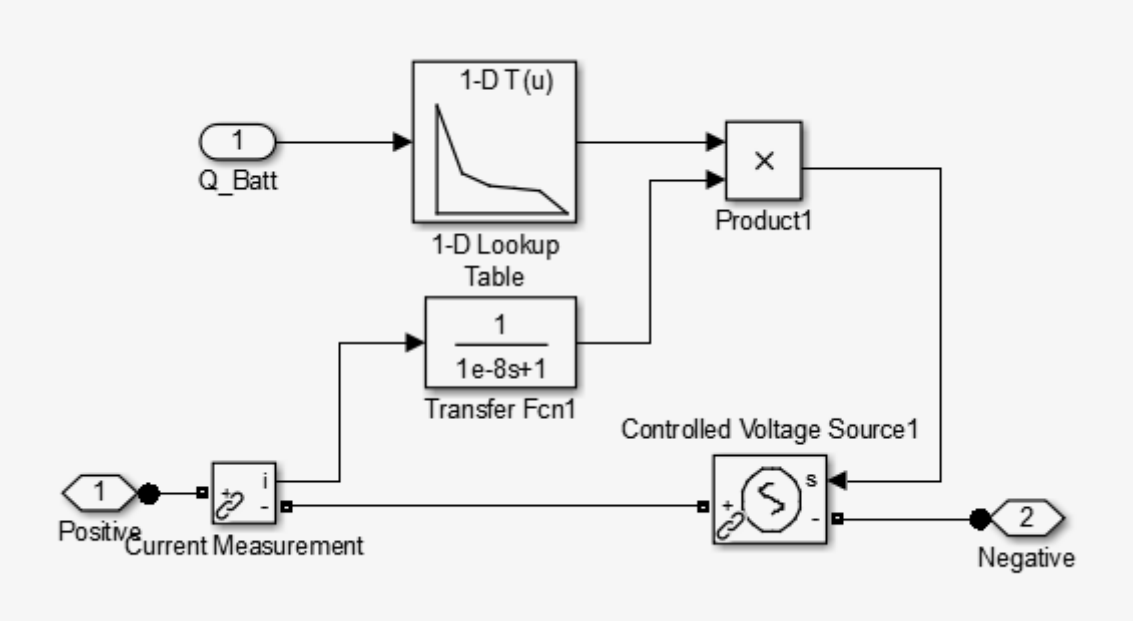

Figure 83: R_t

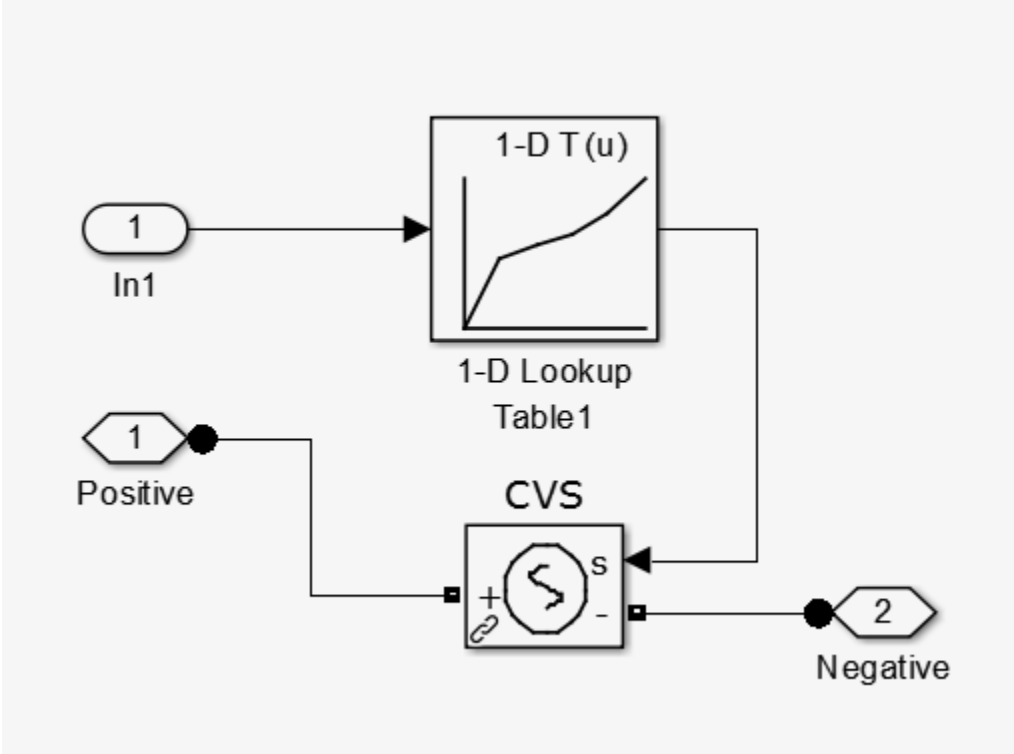

Figure 84: C_t

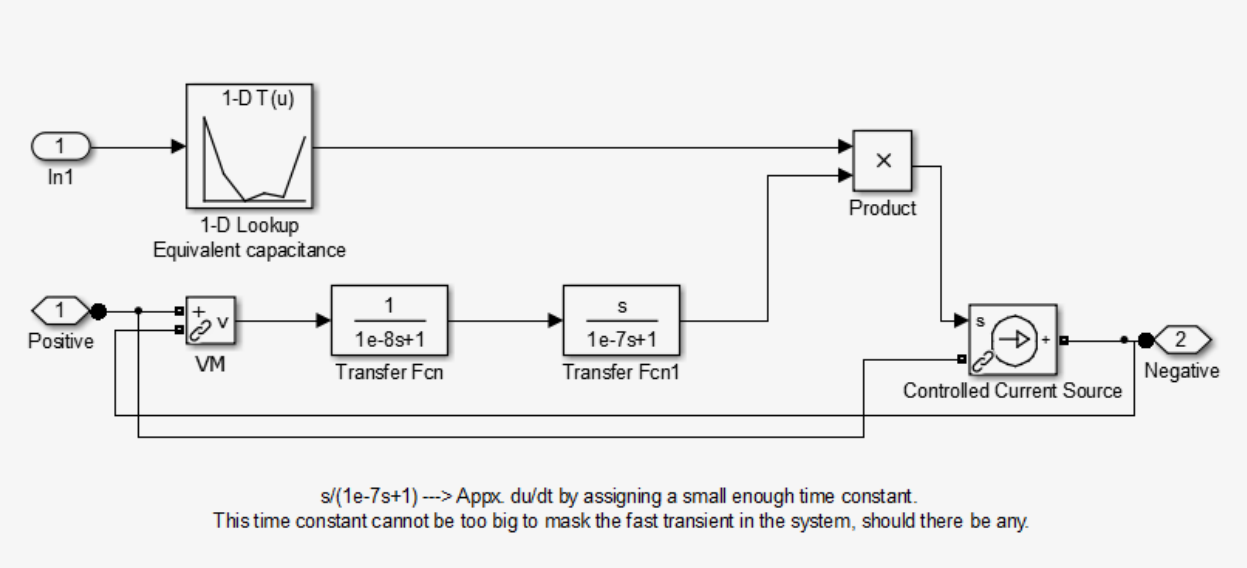

Figure 85: C_{dl}

Appendix D : Simulink model look-up table data

This section covers the lookup table values used in Simulink blocks in the model introduced in section 4.3 and 4.4.

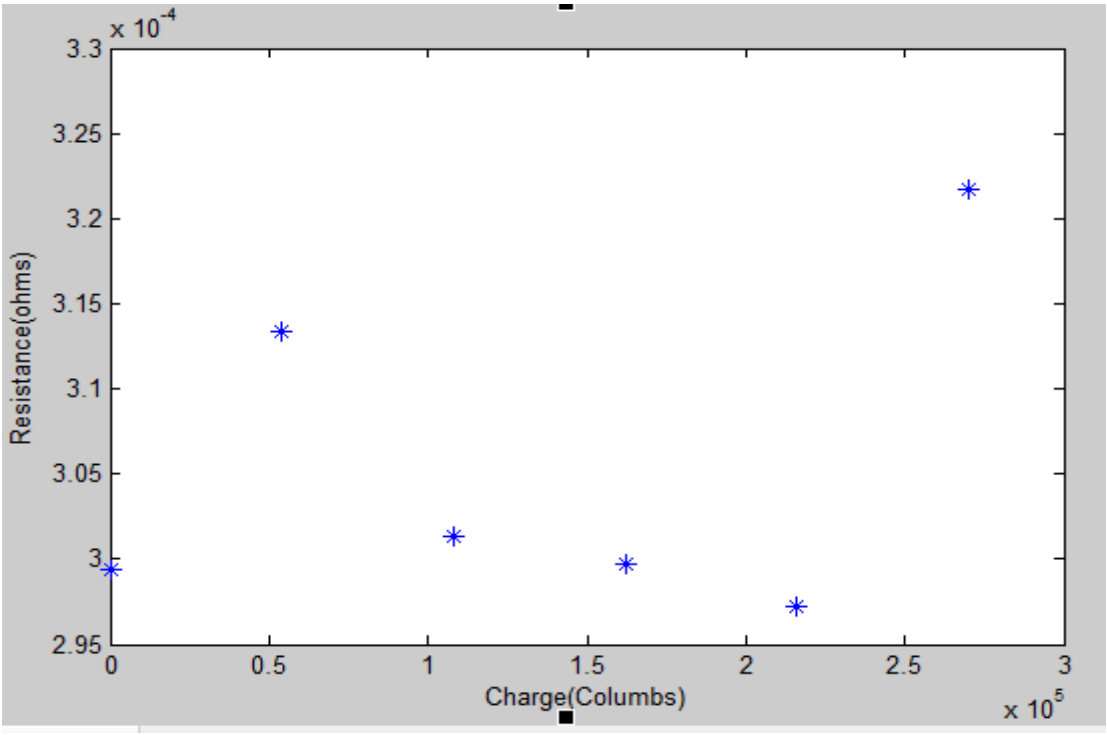

Figure 86: ESR lookup table values

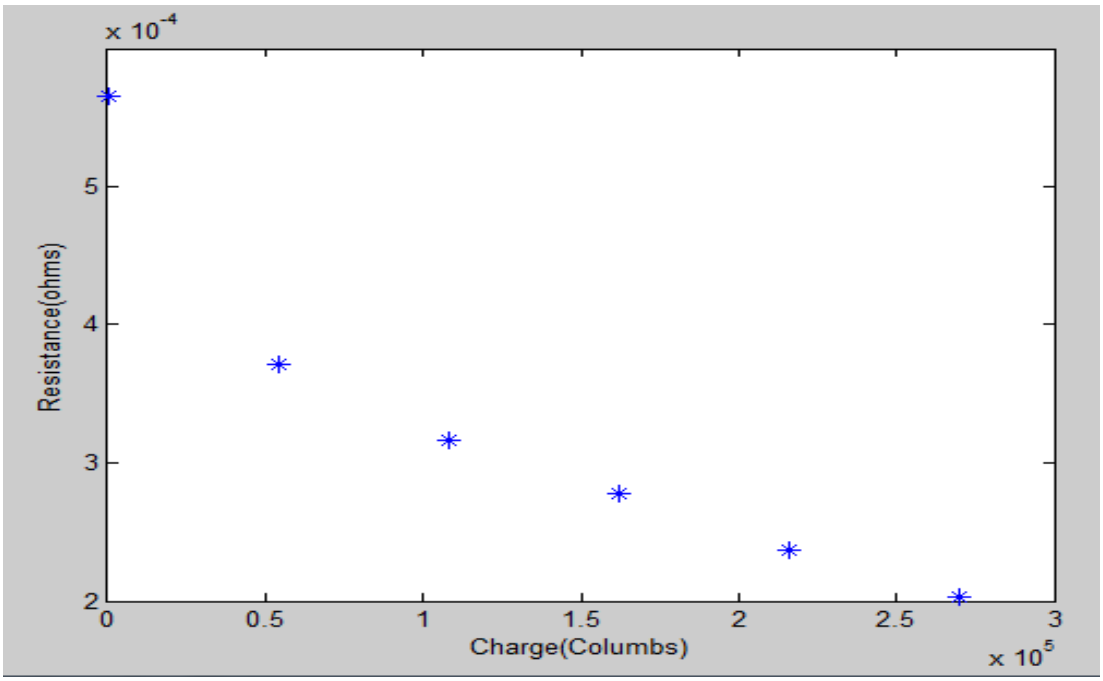

Figure 87: R_{ct} lookup table values

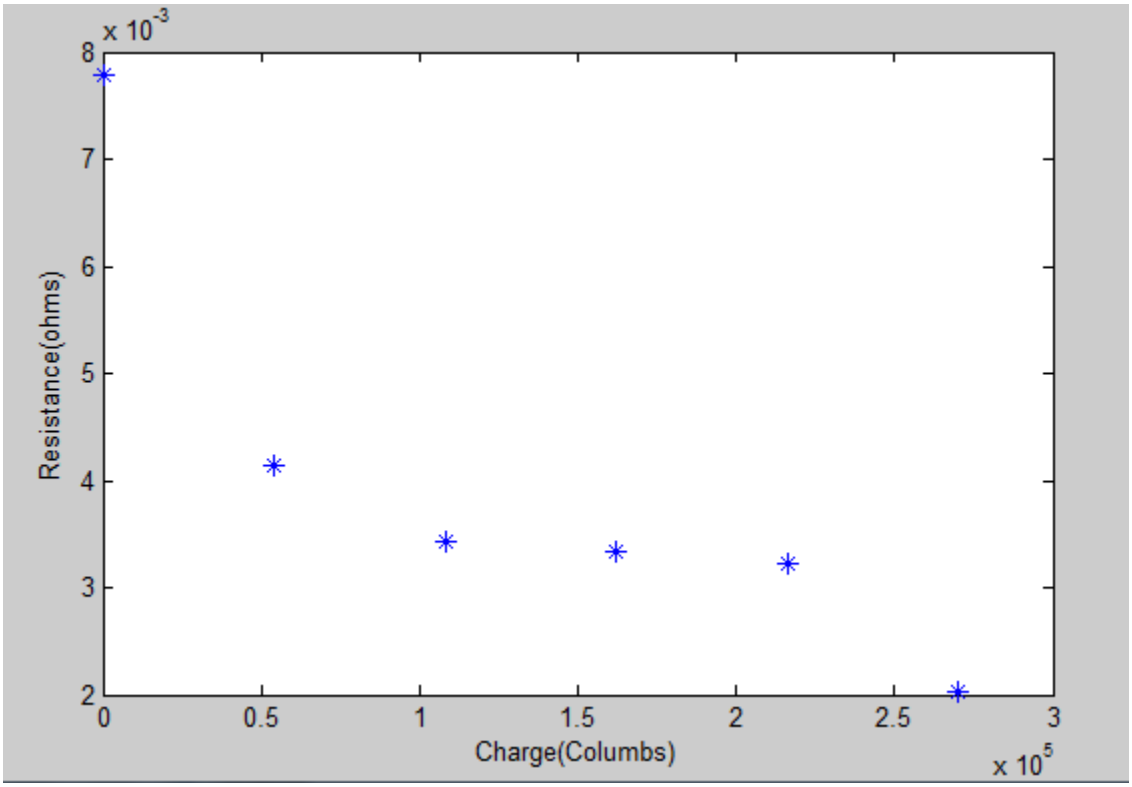

Figure 88: R_t lookup table values

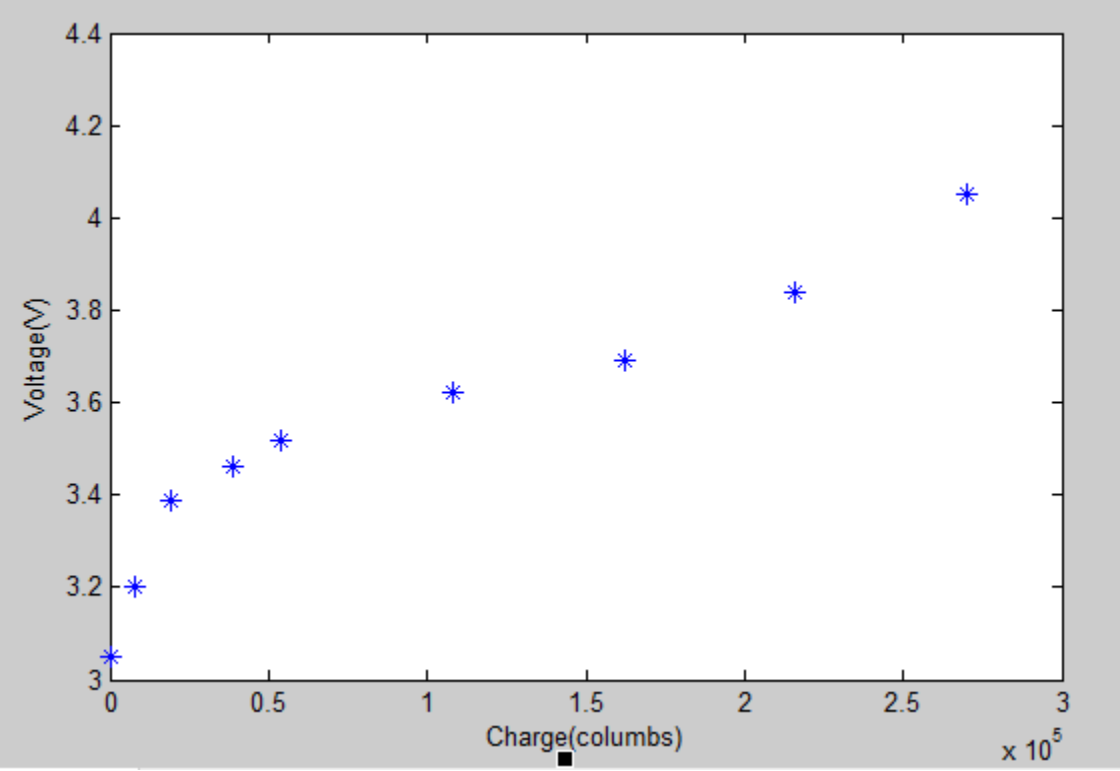

Figure 89: C_t lookup table values

Figure 89 is a plot of Voltage v.s. Charge. C_t is found by using C=q/V.